Synthesis, Characterization and Reactivity Studies of Fe(II) Complexes With Relevance to the Radical SAM Enzymes

Xixi Hong
Marquette University

SYNTHESIS, CHARACTERIZATION, AND REACTIVITY STUDIES OF FE(II) COMPLEXES WITH RELEVANCE TO THE RADICAL SAM ENZYMES

By

Xixi Hong, B.S.

A Thesis submitted to the Faculty of the Graduate School,
Marquette University,
in Partial Fulfillment of the Requirements for
the Degree of Master of Science

Milwaukee, Wisconsin

August, 2014

Abstract

Synthesis, Characterization, and Reactivity Studies of Fe(II) Complexes with Relevance to the Radical SAM Enzymes

Xixi Hong, B.S.

Marquette University, 2014

It is well-established that *S*-adenosylmethionine (SAM) serves as the methyl group donor in methylations of DNA, hormones, neurotransmitters and signal transduction systems. However, a new class of enzymatic reactions involving SAM has recently attracted considerable attention. In these systems, SAM initiates radical-based reactions at the active sites of enzymes via formation of an adenosyl radical, which further abstracts a H-atom from the substrate to initiate a radical-based mechanism. However, modeling studies of radical SAM enzymes have been hindered, by difficulties in preparing adequate synthetic [Fe_4S_4] clusters.

We prepared a novel series of Fe(II) complexes with tripodal tris(2-hydroxybenzyl)amine ligands, which replicate the geometry of the unique Fe centers found in radical SAM enzymes. The resulting complexes were characterized by X-ray crystallography, paramagnetic ^{1}H NMR spectroscopy, electronic absorption spectroscopy, and electrochemical methods. The complexes were evaluated by three criteria established to model the unique Fe site in radical SAM proteins: i) a high spin state, ii) a low redox potential near the value measured for the enzymes (ca. -0.70 V vs SCE), and iii) coordinative unsaturation, such that Fe center can bind exogenous ligands with sulfonium cations.

To determine whether the resulting synthetic models are capable of reductively cleaving S-C bonds to generate radical species, we also prepared sulfonium salts that contain metal-binding moieties, such as a pyridyl group, which position the reactive sulfonium group close to the Fe(II) center. GC-MS and ^{1}H NMR spectroscopy were used to characterize and quantify the resulting products. By monitoring changes in UV-visible absorption features as a function of time, we have measured reaction rates for the following sulfonium cations: *S*-(phenyl) tetramethylenesulfonium and *S*-(2-pyridylmethyl) tetramethylenesulfonium. These experiments allowed us to evaluate the effect of Fe···S distance on the rate of electron transfer. Finally, density functional theory

(DFT) calculations have been performed to further elucidate significant interactions within this synthetic modeling system.

ACKNOWLEDGEMENTS

Xixi Hong, B.S.

It is a pleasure to thank those who made this thesis possible. First and foremost, I would like to express my deep and heartfelt gratitude to my supervisor Professor Adam T. Fiedler for his continuous support and feedback during each step of the research work. His patience, motivation, enthusiasm and guidance are greatly appreciated. I would also like to thank him for his extraordinary amount of experimental and intellectual freedoms during my years here.

I am also grateful to Professor Jier Huang and Professor Chae S. Yi for the time they took to serve in my thesis committee, and I appreciate all the valuable suggestions and advice they gave.

I am extremely appreciative of the financial assistance given by Marquette University Graduate School. I would also like to thank past and present group members for their support and friendship. I am also grateful to all brothers and sisters at Chinese Christian Church of Milwaukee for their prayers and encouragements, and thank Mr.Vaugh Ausman and Dr. Charles Felix Manful for their kindly suggestions and assistances during my graduate study, as well.

Most of all, my heartfelt gratitude and love are due to my grandfather in heaven, grandmother, parents, uncles and other families members for their dedication and the many years of support, no matter where I am and what decision I make. May God bless them in abundance.

TABLE OF CONTENTS

LIST OF TABLES

LIST OF FIGURES

LIST OF SCHEMES

Chapter I

Introduction of Radical SAM Superfamily – Categories, Functions, and Mechanisms

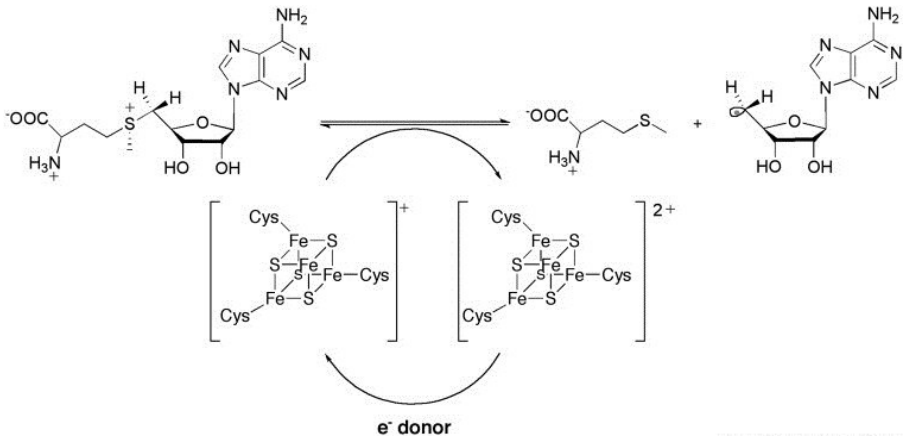

Figure 1.1 Formation of a 5′-deoxyadenosyl radical via a reductive cleavage of *S*-adenosylmethionine.[1]

ABSTRACT: It is well-established that *S*-adenosylmethionine (SAM) serves as the methyl group donor in methylations of DNA, hormones, neurotransmitters and signal transduction systems.[2] However, a new class of enzymatic reactions involving SAM has recently attracted considerable attention. In these systems, SAM initiates radical-based reactions at the active sites of enzymes via formation of an adenosyl radical, in a manner similar to the function of adenosylcobalamin-dependent enzymes.[3] The radical SAM enzymes that have been studied to date have in common the homolytic cleavage of the $[Fe_4S_4]^{1+}$-SAM complexes to yield $[Fe_4S_4]^{2+}$-Met and the 5'-deoxyadenosyl radical (Ado· radical), which further abstracts a H-atom from the substrate to initiate a radical-based mechanism.[4]

1.1 Introduction of the Radical S-Adenosylmethionine Enzyme Superfamily

S-adenosylmethionine (Figure 1.2), also known as SAM or AdoMet, is an important biological sulfonium compound that is biosynthesized via the reaction of methionine with ATP. This reaction is catalyzed by the enzymes SAM synthetase or methionine adenosyltransferase.[5]

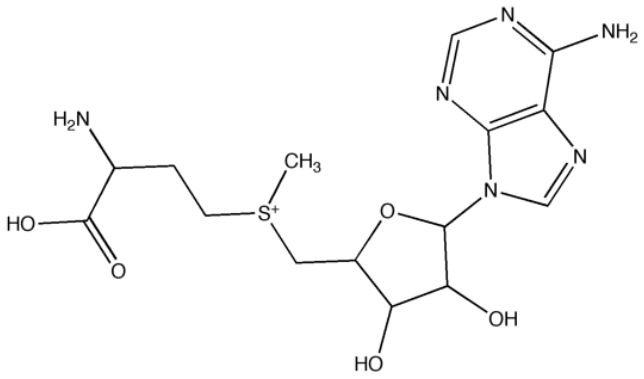

Figure 1.2 The Structure of S-adenosylmethionine (SAM)

For decades, SAM has been recognized as the second most-widely used cofactor after ATP, participating in many significant regulatory processes in living systems. Particularly, it can be utilized as a donor of diverse chemical groups, such as methylene groups (synthesis of cyclopropane fatty acid (CFA)),[6] amino groups (synthesis of 7,8-diaminopelargonic acid (DAPA)),[7] ribosyl groups (synthesis of epoxyqueuosine),[8] aminoalkyl group (synthesis of cyclopropane 1-carboxylic acid (ACC))[9] and methyl groups (Scheme 1.1).[10] Among these reactions, methylation is the most common, playing a critical role in gene expression, hormone regulation, and other processes. Even though the mechanism of these reactions has not been extensively characterized, it is likely that

the electrophilic methyl group adjacent to the positively charged S-atom reacts with nucleophilic substrates via typical SN_2 displacement.[10]

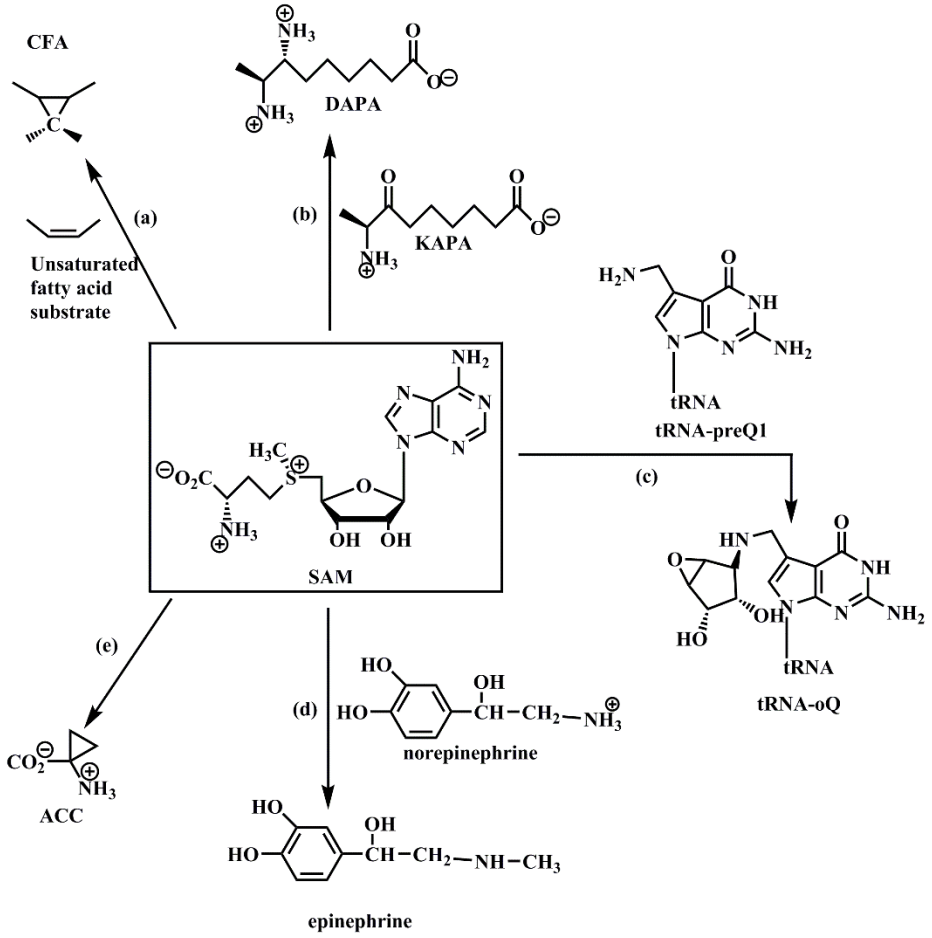

Scheme 1.1 The reactions using S-adenosylmethionine (SAM) as source of chemical groups.[2]

Recently, however, independent studies of three different SAM-participating enzyme systems (lysine 2,3-aminomutase (LAM),[11] pyruvate-formate lyase (PFL)[12] and anaerobic ribonucleotide reductase[13]) have revealed a new and unanticipated function of SAM as a radical initiator. The homolytic cleavage of the S-C(Ado) bond in SAM gives rise to an adenosyl radical (Ado•) that reacts with substrates. The function of SAM is

equivalent to that of the adenosylcobalamin cofactor in coenzyme B12-dependent enzymes that catalyzes radical rearrangements.[3] The radical SAM superfamily, however, is much more extensive,[11] with over 2800 members (and counting). Enzymes in this superfamily carry out a wide variety of chemical transformations, including substrate oxidation, sulfur-insertion,[14] and other functions yet to be discovered (Table 1.1). The first member of this family to be discovered was lysine 2,3-aminomutase, which was first characterized by H. A. Barker in the late 1960s and early 1970s.[11]

Table 1.1 Radical SAM enzymes and associated biological functions.[4]

Protein	Function	Reference
LAM	Lysine 2,3aminomutase	Ruzicka *et al.*, 2000
Eam	Glutamate 2,3-aminomutase	Ruzicka & Frey, 2007
SplB	Spore photoproduct lyase	Rebeil *et al.*, 1998
DesII	Desosamine biosynthesis	Trefzer *et al.*,1999
Littorine mutase	Alkaloid biosynthesis	Ollagnier *et al.*, 1998
PFL activase	Glycyl radicalization	Wong *et al.*, 1993
BioB	Biotin synthase	Duin *et al.*, 1997
HemN	Coproporphyrinogen III oxidase	Akhtar, 1994
MoaA	Molybdopterin biosynthesis	Rieder *et al.*, 1998
MiaB	Methylthiolation of tRNA	Esberg *et al.*, 1999
TYW1	Wybusine biosynthesis in $tRNA^{Phe}$	Nona *et al.*, 2006

All members of the SAM superfamily feature a canonical $CX_3CX_2CX_3$ $[Fe_4S_4]$ binding motif and a SAM binding motif.[4] Most enzymes share a relatively common triosephosphateisomerase (TIM) barrel tertiary structure, in which eight β-strands are arranged in a barrel with eight intervening α-helices (Figure 1.3). In some cases (such as

LAM), the enzyme uses a modified "¾ TIM barrel" with only six pairs of α-helices and β-strands.[15] Each barrel contains a [Fe_4S_4] cluster bound to three conserved cysteine (Cys) residues. One Fe center in the cluster lacks Cys coordination; this "unique Fe" is therefore capable of binding the SAM cofactor via its carboxylate and amino groups, resulting in a five-coordinate Fe site. [16]

The cleavage of SAM generates the 5'-deoxyadenosine radical (Ado• radical), which initiates biochemical reactions via the abstraction of hydrogen atom from substrates.[4] Even though this step is very common to all radical SAM enzymes, there are still mechanistic variations. In some cases, such as LAM, the SAM cofactor serves as a coenzyme that is regenerated in the end of the catalytic cycle. [13] Alternatively, in biotin synthase, SAM is a co-substrate that is consumed during the reaction turnout.[14] Finally, the recently-discovered RlmN and Cfr enzymes[13,17] utilizes two equivalents of SAM for catalysis: one for radical generation and another for methyl-group donation. These three classes of radical SAM enzyme will be discussed in turn briefly.

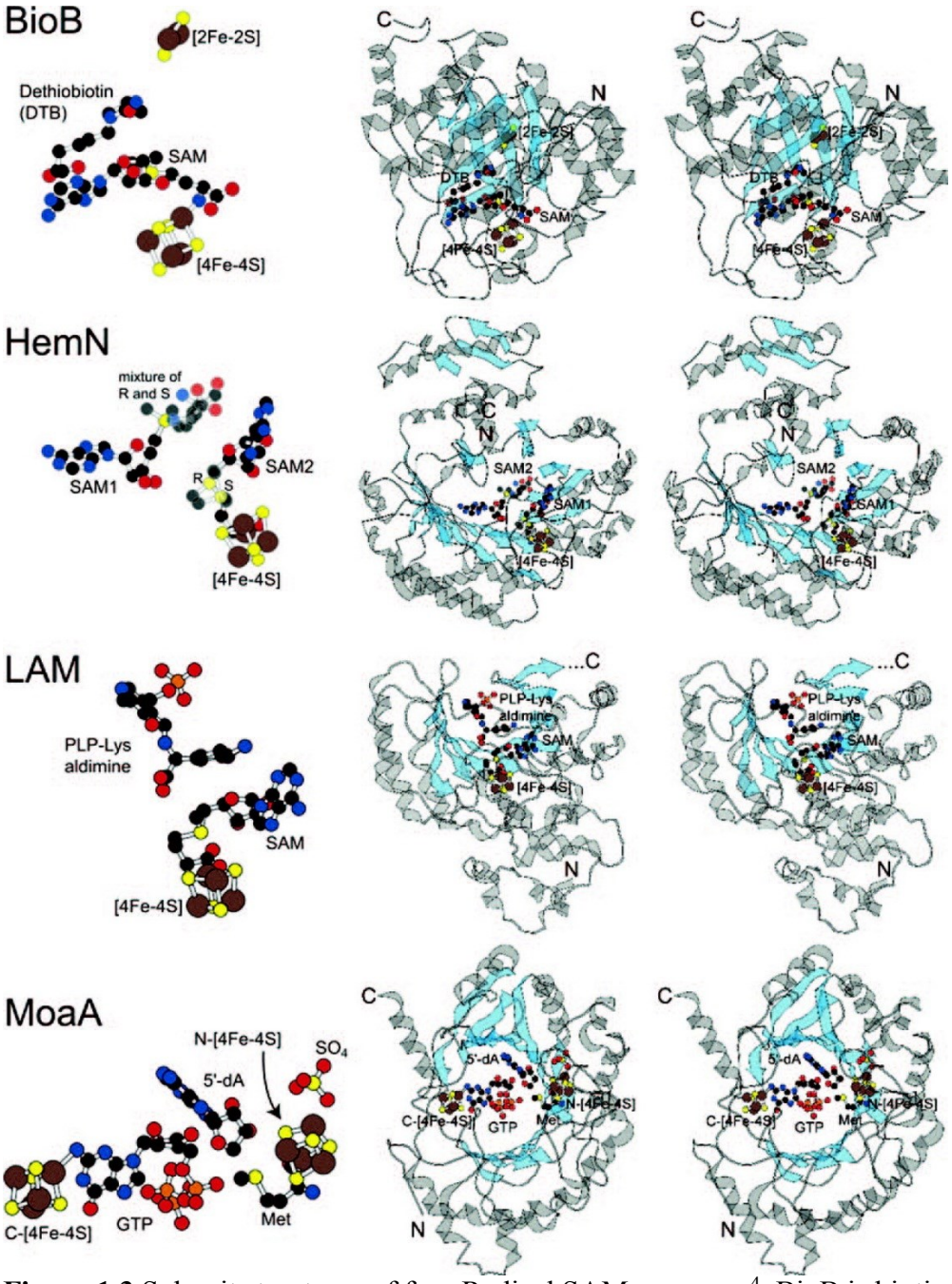

Figure 1.3 Subunit structures of four Radical SAM enzymes.[4] BioB is biotin synthase, and the subunit is folded in $(\alpha\beta)_8$ (TIM barrel) shown in a side view. HemN is coproporphyrnogen oxidase III, and the subunit fold is in $(\alpha\beta)_6$ (3/4-barrel), shown down the barrel axis. LAM is lysine 2,3-aminomutases, and the subunit fold is in $(\alpha\beta)_6$ (3/4-barrel), shown down the barrel axis. MoaA is required in molybdoprotein biosynthesis, and the subunit fold is in $(\alpha\beta)_6$(3/4-barrel) , shown down the barrel axis.

1.1.A Lysine 2,3-aminomutase: SAM as co-catalyst

Aminomutases have been studied extensively since the discovery of lysine 2,3-aminomutase by H. A. Barker in the late 1960s.[11] These enzymes catalyze the reversible intramolecular migration of an amino group between adjacent carbon atoms in the substrate (Scheme 1.2). Such rearrangements are required for the metabolism of lysine in anaerobic organisms, which degrade lysine into acetyl CoA.

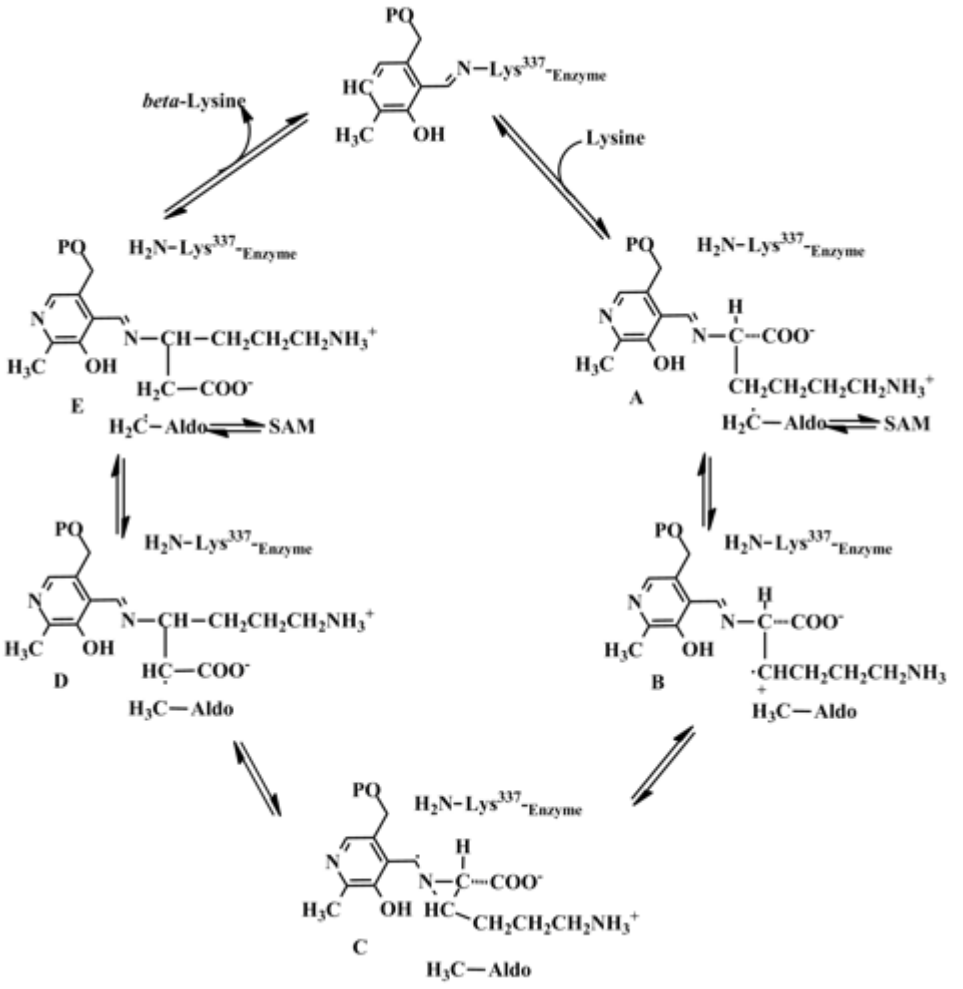

Scheme 1.2 Radical mechanism of the reaction of LAM.[18]

As shown in Scheme 1.2, the radical-mediated transamination reaction proceeds via several steps.[18] In the first step, the amino group lysine substrate condenses with pyridoxal 5'-phosphate (PLP) to form an aldimine linkage ($RHC=NH_2^+$) in the active site (the so-called internal PLP-aldimine).[19] The $[Fe_4S_4]$/SAM unit then generates an Ado· radical that abstracts a H-atom from 3-pro-R position of the lysine side chain, resulting in the radical **B**. Two-step radical rearrangement gives rise to the intermediate **D**, which in turn abstracts a H-atom from H_3C-Ado to give the desired product (release of the product requires hydrolysis of the PLP-aldimine unit). The adensoyl radical can react with methionine to regenerate the SAM cofactor. During the whole process, LAM serves as a coenzyme, catalyzing the isomerization reversibly without consumption. Most of other aminomutases also share similar mechanism.

1.1.B Biotin Synthase: SAM as co-substrate

The cofactor biotin (Vitamin H) – generated only by plants and certain microorganisms – is necessary for cell growth and the metabolism of fats and amino acids.[4] The final step of biotin production, catalyzed by biotin synthase (BioB), involves insertion of a S-atom into dethiobiotin to generate the five-membered tetrahydrothiophene ring. This remarkable reaction requires the activation of methyl and methylene C-H bonds, which are generally inert.[20]

Biotin synthase overcomes these difficulties by using the radical-generating apparatus that is typical of the radical SAM superfamily. BioB contains multiple Fe/S clusters with different functions. One $[Fe_4S_4]$ cluster binds SAM to initiate the radical-base chemistry,[14] while a $[Fe_2S_2]$ cluster serves as the source of the S-atom.[21]

Looking at the active site structure (Figure 1.4),[1] dethiobiotin (DTB) is packed deeply between the $[Fe_4S_4]^{2+}$ and $[Fe_2S_2]^{2+}$ clusters in each dimer subunit. The distance between C9 of dethiobiotin and the proximal iron center of the $[Fe_2S_2]^{2+}$ cluster is 4.6 Å. In addition, the positively charged S-atom in SAM is 2.7 Å away from the unique iron in $[Fe_4S_4]^{2+}$, facilitating reductive cleavage of S-C bond in SAM. As shown in Scheme 1.3, the resulting Ado• radical abstracts a H-atom from C9 and the dethiobiotin radical then captures a sulfide ion from the $[Fe_2S_2]^{2+}$ cluster.[20,21] Consumption of a second SAM cofactor results in formation of a carbon-centered radical at C6, which reacts with the alkylthiolate group to complete formation of the 5-membered ring.

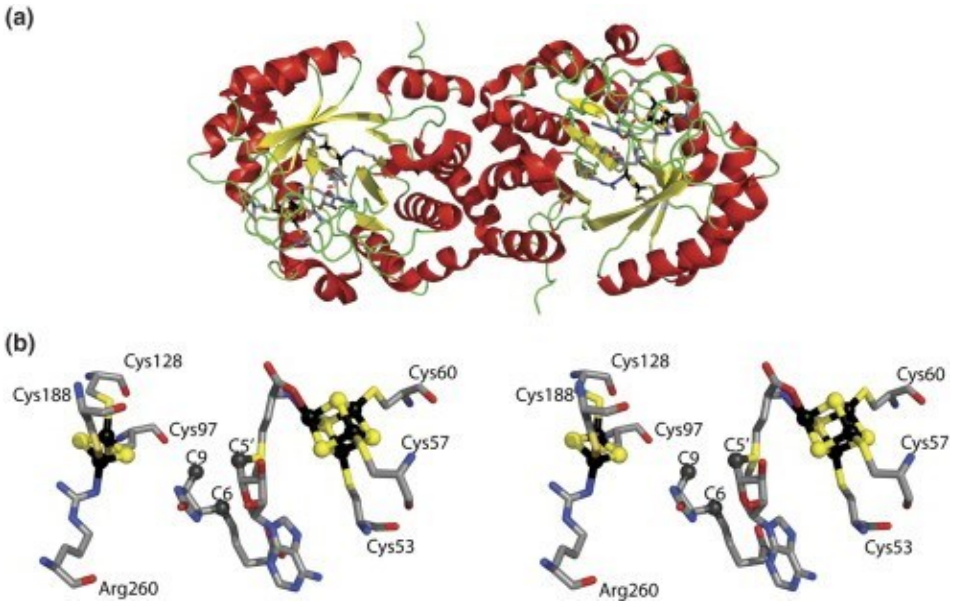

Figure 1.4 X-ray structure of biotin synthase **(a)** Structure of homodimer showing the $(\alpha/\beta)_8$ barrel fold. **(b)** Selected view of the active site.[1]

In this mechanism, the $[Fe_4S_4]$ cluster is responsible for the electron transfer and the homolytic cleavage of SAM, while $[Fe_2S_2]^{2+}$ is degraded to provide the sulfur atom of biotin. The fate of the degraded iron cluster is uncertain, although some studies have

proposed the reconstruction of this cluster by cysteine desulfurases (IcsS or SufS) and FeS cluster assembly proteins (IScU/A or SufA).[22]

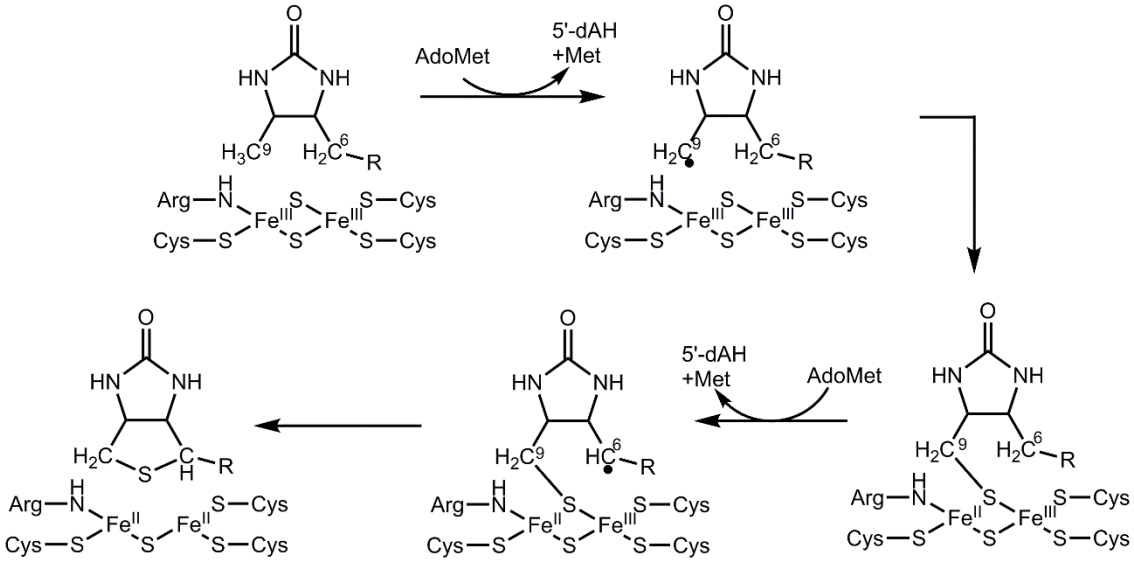

Scheme 1.3 The mechanism of sulfur insertion in the reaction of BioB.[21]

1.1.C Radical-mediated enzymatic methylations: RlmN and Cfr

As mentioned above, SAM is a common methyl-transfer agent in biological systems.[2] The posttranscriptional and posttranslational methylation of RNA, DNA and proteins are traditionally achieved via S_N2 nucleophilic displacement.[23, 24] The methylation of specific amino acid side-chains or nucleotide bases improve the stability of the biomolecules, and often enhances resistance to antibiotics.[25]

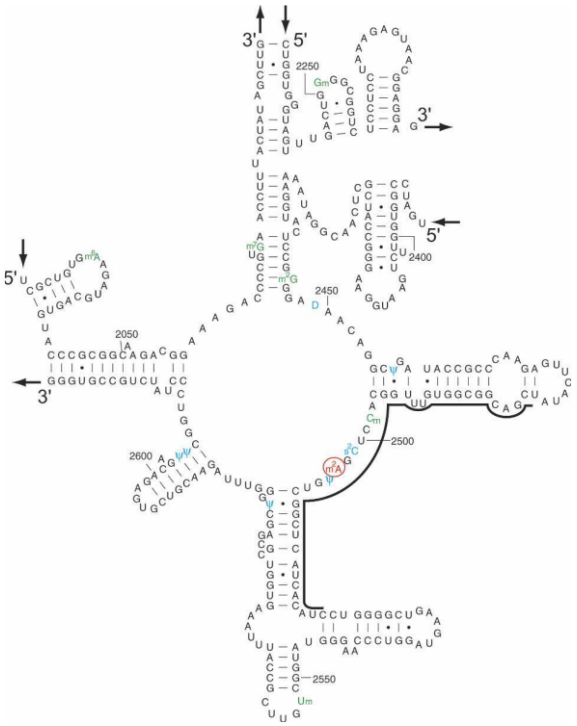

Figure 1.5 Secondary structure of domain V of *Escherichia coli* 23S rRNA[25]. M^2A2503 is circled.

However, recently, Professor Squire Booker's group at Penn State University has uncovered a novel mechanism for the methylation of adenosine 2503 (A2503) in the 23S rRNA nucleotide.[17] In bacteria, rRNA modification involves mainly methylation of rRNA residues and pseudouridylation.[26] In the case of *Escherichia Coli* 23S rRNA, there are fourteen modifications associated with domain V – the main component of the peptidyl transferase center (Figure 1.5)[25] – seven of which correspond to methylations. One methylated nucleotide residue is A2503, which is close to the interaction sites of peptidyl transferase center-targeting antibiotics.[27] The involvement of methylations at C2 of A2503 by RlmN methyltransferase can result in resistance against a number of antibiotics.[28,29] RlmN belongs to the SAM superfamily and accomplishes this complex

reaction by using two equivalents of SAM that play distinct roles as methyl donor and radical initiator. [13]

X-ray crystallographic studies have shown that the RlmN active site contains an [Fe_4S_4] cluster with the canonical SAM motif, adenosine 2503, and two mechanistically important cysteine residues: Cys355 and Cys118 in a $(\alpha/\beta)_6$ TIM barrel (Figure1.6 (A)).[17] The distance between Cys355 and the methyl group of SAM is 3.6 Å (Figure1.6 (B)); such proximity results in the highly-favorable methylation of Cys355 by SAM via S_N2 displacement.[13] Thus, methylation of the adenine ring does not occur by direct reaction with SAM, which is not surprising given that the site of adenine methylation is an electrophilic sp^2-hydrized carbon, not a nucleophilic one.[17]

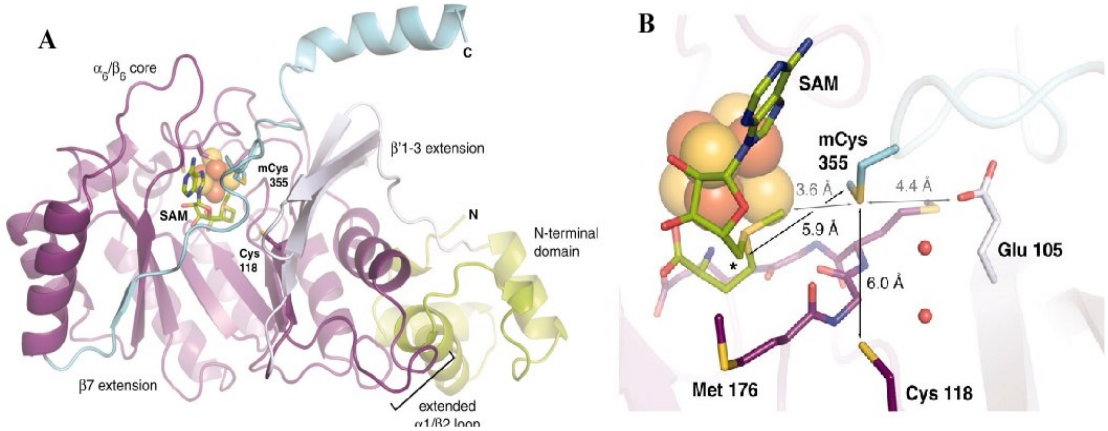

Figure 1.6 The Structure of *E. Coli* RlmN with SAM.[17] **(A)** Structure showing the $(\alpha/\beta)_6$ barrel fold. **(B)** Selected view of the active site.

The next step involves generation of the Ado• radical from reductive cleavage of the second equivalent of SAM. The Ado• radical then abstracts a hydrogen atom from the methylated-Cys355 residue, thereby initiating the multi-step mechanism (Scheme 1.4).[13] The catalytic cycle ends with formation of a disulfide bond between Cys355 and

Cys118 (step 5) and the imine/enamine tautomerization (step 6) to yield methylated A2503. The mechanism of the Rlm methyltransferase therefore combines the two biological functions of SAM: traditional S_N2-type methylation and radical-initiated reactions.

Booker's group also found that Cfr, which methylates C8 in A2503, shares an identical mechanism.[13]

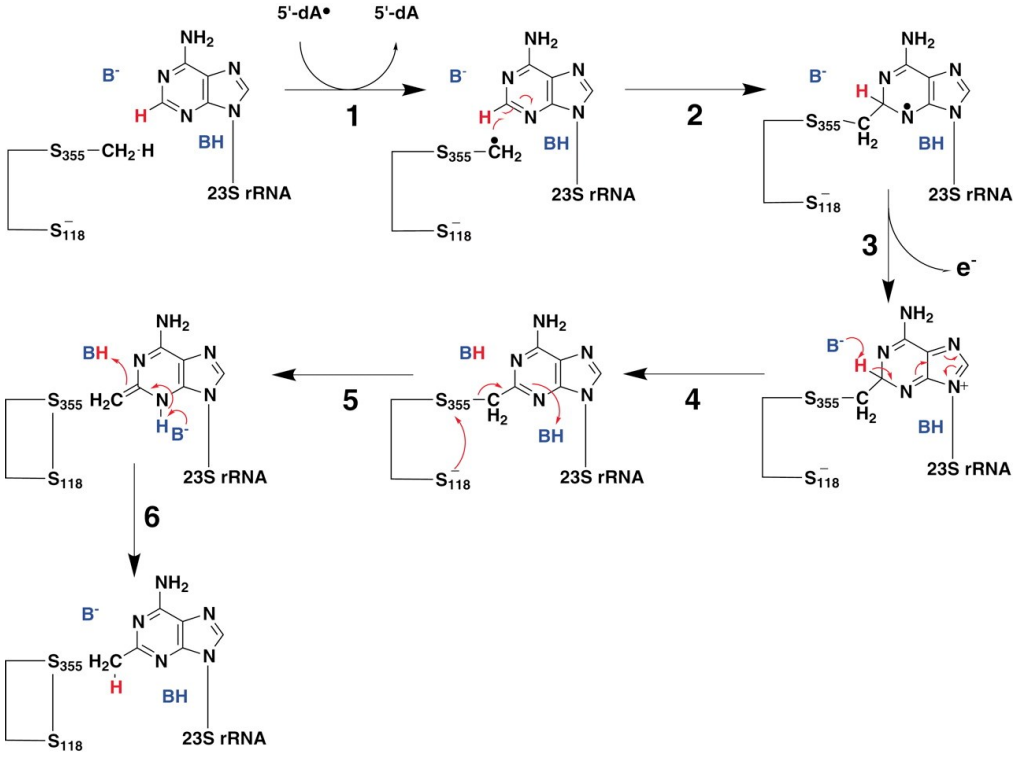

Scheme 1.4 Postulated mechanism of RlmN. BH, unidentified general acid; B-, unidentified general base.[13]

1.2 Mechanistic Questions Regarding The Radical-SAM Enzymes

As highlighted in the previous examples, the SAM superfamily of enzymes is of great significance to biochemical processes *in vivo*. Though radical SAM enzymes

catalyze an impressive variety of chemical reactions (Table 1.1),[4] central to each enzymatic mechanism are two common steps: i) coordination of SAM to the unique Fe site via the carboxylate and amino groups of the methionine moiety (with the approximate bond lengths of 2.51 and 2.35 Å)[4], and ii) the reduction of $[4Fe\text{-}4S]^{2+}$ by flavodoxin and the subsequent generation of the Ado$^{\bullet}$ radical, which serves as the initiator of radical chemistry.

Multiple questions have been raised regarding this central step in the catalytic cycle. The first concerns the thermodynamics of the electron-transfer that results in cleavage of the S-C(Ado) bond. The reduction potential of the free SAM cofactor is −1.8 V (vs. NHE), while the redox potentials for $[Fe_4S_4]^{1+/2+}$ clusters in radical SAM enzymes range from –430 mV to –500 mV. Thus, it appears that $[Fe_4S_4]^{1+}$ clusters are not competent to reduce SAM, because the electron transfer would have to surmount an energetic barrier of 32 kcal/mol ($\Delta G^{o} = -nF\Delta E^{o}$).[30]

The second open question concerns the pathway for the inner-sphere electron transfer (E.T.). Two possibilities have been proposed, as shown in Figure 1.7. The first involves an interaction of the sulfonium group with the unique Fe center of the cluster prior to ET, followed by the formation of a Fe-S(Met) bond following ET. The second scenario envisions an interaction between the sulfonium group and a sulfide in the Fe/S cluster; in this case, the resulting methionine would not coordinate to the cluster following ET.

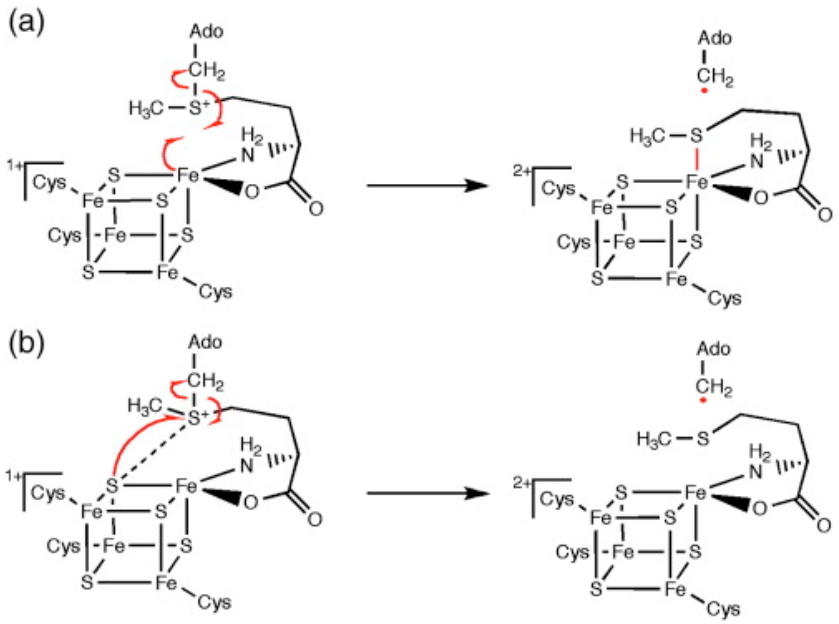

Figure 1.7 Two mechanisms for the reductive cleavage of SAM. (a) The reversible cleavage and interaction of sulfur in methionine to the unique iron. (b) Irreversible cleavage and interaction of sulfur in methionine with a sulfide in $[Fe_4S_4]^{2+}$.[31]

1.2.A Thermodynamics of SAM Reduction

The redox properties of LAM have been studied extensively by Prof. Perry Frey at UW-Madison. As noted above, the midpoint reduction potential for $[Fe_4S_4]^{2+/1+}$ is near -450 mV,[32] while the reduction potential of free SAM in aqueous solution is -1.8 V (Figure 1.8). Thus, electron transfer from the $[Fe_4S_4]^{+}$ cluster to SAM is extremely unfavorable with an energy barrier of almost 32 kcal mol^{-1}. Frey et al. found that the coordination of SAM to the enzyme active site elevates the $[Fe_4S_4]$ reduction potential by 50 mV,[32] while the presence of the substrate lysine (forming the external PLP aldimine) lowers the potential of the $[Fe_4S_4]$/SAM complex to –600 mV (blue line in Figure 1.8). The most dramatic change, however, occurs for the potential of the SAM cofactor, which increases by 810 mV (to -990 mV) upon binding to the Fe/S cluster.

The dramatic elevated potential of SAM in the active site of LAM can be attributed to its ligation to the [Fe_4S_4] cluster. Following electron transfer, the unique Fe site in the [Fe_4S_4] cluster is proposed to change from pentacoordinate to hexacoordinate – a more favored coordination geometry for iron.[33] The binding of the S-atom of methionine to the oxidized [Fe_4S_4]$^{2+}$ cluster stabilizes the product of S-C(Ado) cleavage, which accounts for the increased potential of SAM in the LAM active site.

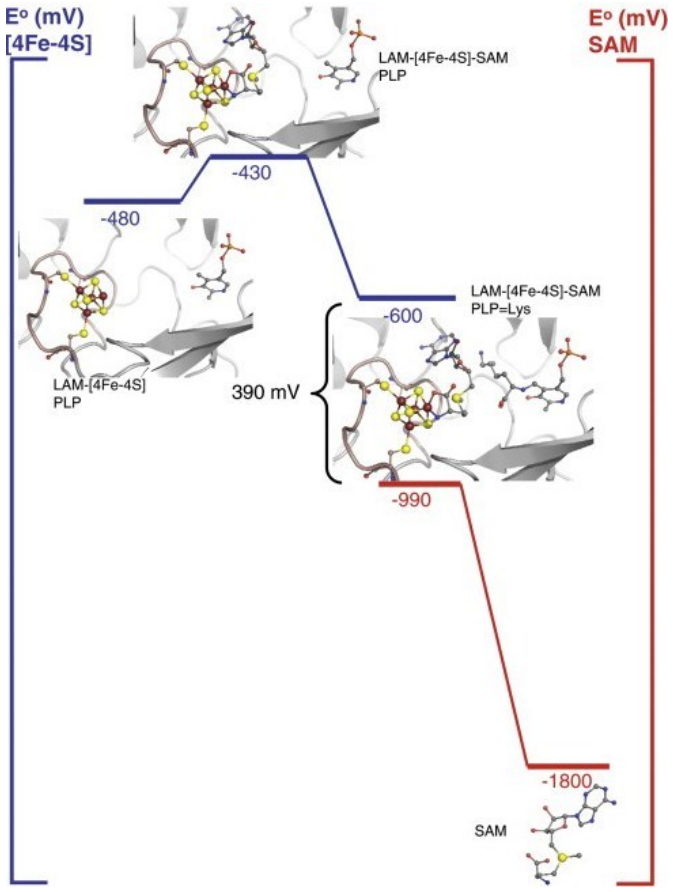

Figure 1.8 Binding energetics and redox potentials in the radical SAM enzyme LAM.[33]

1.2.B Nature of Interaction between SAM and [Fe_4S_4] Cluster

X-ray crystallographic and absorption data suggest that the Fe/sulfonium interaction is the most likely mechanism by which SAM is cleaved reversibly to Ado• radical (Pathway (a) in Figure 1.7). Cosper et al. used selenium-substituted SAM in their studies of LAM as a suitable analogue of SAM.[16] Selenium X-ray absorption spectra indicate a sizable interaction between the Fe and Se centers after the radical fragmentation. Therefore, they concluded that the S (or Se) atom in the methionine (or selenomethionine) product likely coordinates to the unique Fe site (Figure 1.9 (A)). Furthermore, X-ray crystal structures of LAM with the [Fe_4S_4] cluster, PLP, SeSAM and lysine (Figure 1.9 (B)) provided further evidence with the spatial distance of 3.2 Å between Se and the unique Fe site.[15]

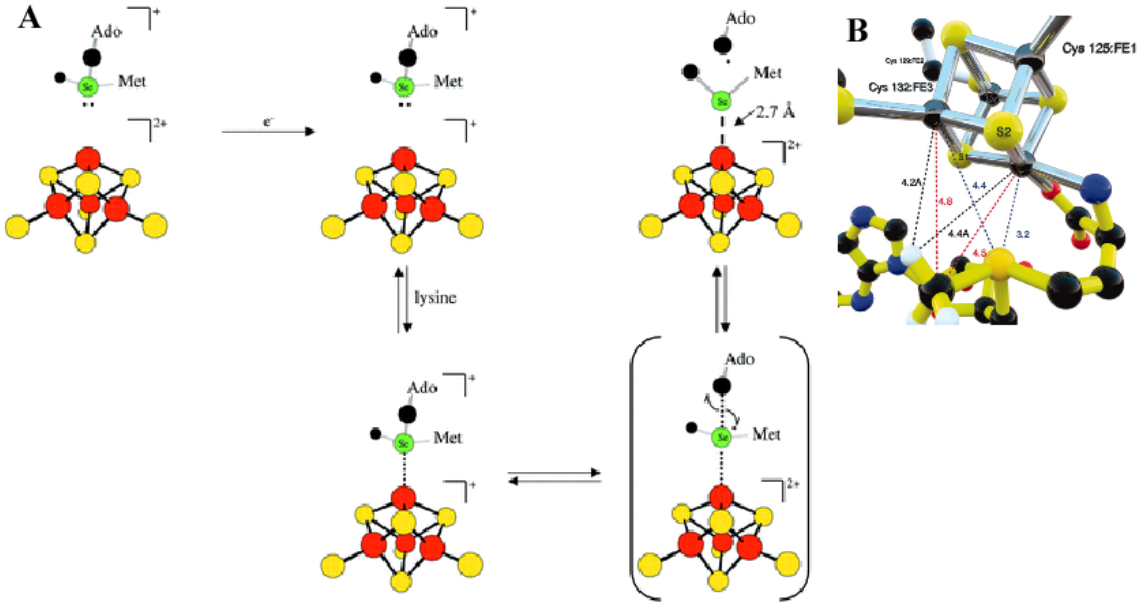

Figure 1.9 (A) Proposed Mechanism for Generation of Ado• radical in LAM bound to SeSAM;[16] (B) Structure of the $[Fe_4S_4]^{1+}$ cluster in the active site of LAM bound to SeSAM.[15]

In Figure 1.7 (b), the sulfonium moiety interacts primarily with a sulfide anion of the $[Fe_4S_4]$ cluster. ENDOR and Mössbauer studies of BioB and pyruvate lyase suggested that the sulfonium group of SAM lies closer to a sulfide atom than the unique Fe center[34], which supports this scenario. In addition, a computational (QM/MM) study found that the Fe-$S_{(SAM)}$ and C_{SAM}-S_{SAM} bond distances are almost unchanged before and after the reduction of the $[Fe_4S_4]$ cluster (Figure 1.10).[31] Furthermore, calculated charge and spin densities of the Fe and S centers support the postulation that the unique Fe is not directly responsible for C-S bond cleavage.[31] In Figure 1.10, the $S_4\cdots S_{SAM}$, and $S_1\cdots S_{SAM}$ distances are 3.30 and 3.69 Å, respectively; such relatively close distances increase the possibility of inner-sphere electron transfer between a sulfide atom in the Fe/S cluster and the sulfonium group in SAM.

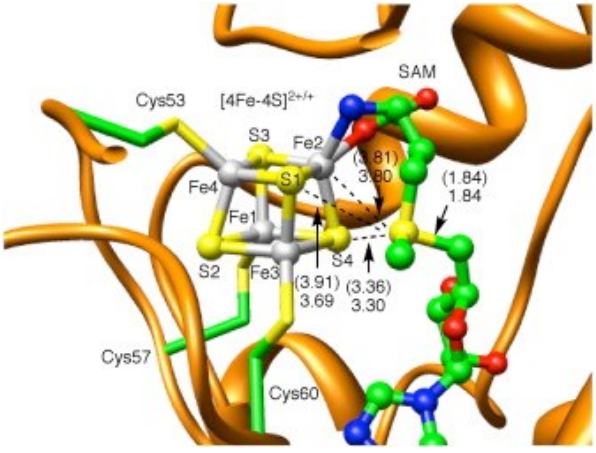

Figure 1.10 Optimized structure of the ($[Fe_4S_4]^{2+}$) $[Fe_4S_4]^{1+}$ cluster in the active site of biotin synthase. Units are in Å.[31]

Another issue that deserves attention is the enzymatic control of the inherently reactive Ado• radical to avoid harmful side reactions. There are several explanations for the controlled radical fragmentation in SAM enzymes: i) due to the large gap between the redox potentials of [Fe_4S_4] and free SAM, electron transfer and bond cleavage are only favorable in the presence of substrate,[30] ii) the location of the active site deep within the TIM barrel seals off the cluster from solvent, preventing reactions with stray molecules,[35] and iii) second-sphere residues position the SAM cofactor and substrate in close proximity to each other, which facilitates reaction of the Ado radical with the intended H-atom.[30] These second-sphere interactions involve hydrogen bonds, van der Waals interactions, and hydrophobic contacts.[30] For example, there are conserved residues and eight water molecules in the LAM active site that hold the PLP-lysine substrate in the correct position through hydrogen bonds.

1.3 Reaction of Synthetic $[Fe_4S_4]^{2+/1+}$ Clusters with Sulfonium Cations

As discussed in the previous section, [Fe_4S_4] clusters play a central role in the radical SAM superfamily of enzymes.[4] These clusters contain three Fe centers capped by conserved Cys residues and one differentiated "open" Fe site, which can bind SAM through its carboxylate and amine groups. In the presence of SAM and substrate, the reduction of the $[Fe_4S_4]^{2+}$ cluster by biological reductants such as flavodoxin, prompts electron transfer and homolytic cleavage of the S−C bond. The products of the reaction are $[Fe_4S_4]^{2+}$ cluster, methionine, and the 5'-Ado• radical that can participate with high reactivity in important biochemical processes.

Given the prevalence of the SAM superfamily, there is an interest in elucidating the mechanism of the reductive cleavage of sulfonium ions by $[Fe_4S_4]^{1+}$ cluster. However, modeling studies have been prohibited by difficulties in preparing adequate synthetic $[Fe_4S_4]^{1+}$ clusters. In 2001, Holm's group, studied the reactivity of synthetic $[Fe_4S_4(SPh)_4]^{2-/3-}$ cluster (**1, 2**) with various sulfonium salts $[PhMeSCH_2R]^+$ (R = COPh **3**, *p*-C_6H_4CN **4**) (Table 1.2).[36] They observed a mixture of products arising from two pathways: i) electrophilic attack of the sulfonium group on the thiolate ligands, ii) two-electron reduction of the sulfonium compounds by two equivalents of $[Fe_4S_4]^{1+}$ cluster. Thus, the reactivity of this synthetic system deviates from the reactivity of the biological radical SAM enzymes.[30]

Table 1.2 Designations of compounds.

Species	Number
$[Fe_4S_4(SPh)_4]^{2-}$	**1**
$[Fe_4S_4(SPh)_4]^{3-}$	**2**
$[PhMeSCH_2R]^+$	R = COPh **3**; *p*-C_6H_4CN **4**
PhMeS=CHR	**5**
$PhOCH_3$	**6**
$PhSCH_2COPh$	**7**
$PhSCH_2$-*p*-C_6H_4CN	**8**

In Holm's synthetic system, the selected sulfonium salts are made as dialkylarysulfonium ions with a methyl group, which replicates methyl group in SAM. The sulfonium salts have irreversible reduction potentials E_{pc} = -0.91 V (**3**) and -0.92 V (**4**) vs. SCE, while the redox potential $E_{1/2}$ for the couple of $[Fe_4S_4(SPh)_4]^{2-/3-}$ in

acetonitrile is -1.00 V. This result indicates that the analogue clusters are thermodynamically competent to reduce sulfonium cations.[36]

The reaction of the reduced cluster $[Fe_4S_4(SPh)_4]^{3-}$ with **3** or **4** involves initial S−C cleavage by electron transfer and the generation of PhSMe and radical RCH_2• (**R-1**). There are three possibilities for the fate of RCH_2•. The first one involves the reduction by second equivalent $[Fe_4S_4(SPh)_4]^{3-}$ (**R-2**) to generate a transient carbanion $RCH_2:^-$. The second one is hydrogen abstraction from solvent or other hydrogen donors to form RCH_3 (**R-3**). In the third one, the coupling of two RCH_2• to give the combination product RCH_2CH_2R (**R-4**):

$$[Fe_4S_4(SPh)_4]^{3-} + [PhMeSCH_2R] \rightarrow [Fe_4S_4(SPh)_4]^{2-} + PhSMe + RCH2\bullet \quad (\mathbf{R\text{-}1})$$

$$[Fe_4S_4(SPh)_4]^{3-} + RCH_2\bullet \rightarrow [Fe_4S_4(SPh)_4]^{2-} + RCH_2:^- \quad (\mathbf{R\text{-}2})$$

$$RCH_2\bullet + PhSH \rightarrow RCH_3 + PhS\bullet \quad (\mathbf{R\text{-}3})$$

$$2RCH_2\bullet \rightarrow RCH_2CH_2R \quad (\mathbf{R\text{-}4})$$

Upon careful examinations of the NMR spectra (Figure 1.11),[36] Holm's group didn't detect the coupling products: RCH_2CH_2R (**R-4**) or the disulfide of PhSSPh derived from radical PhS• (**R-3**). They, therefore, postulated that **R-2** is the dominant reductive cleavage pathway, which means that the cleavage of the sulfonium substrate is a two-electron process in this model system.

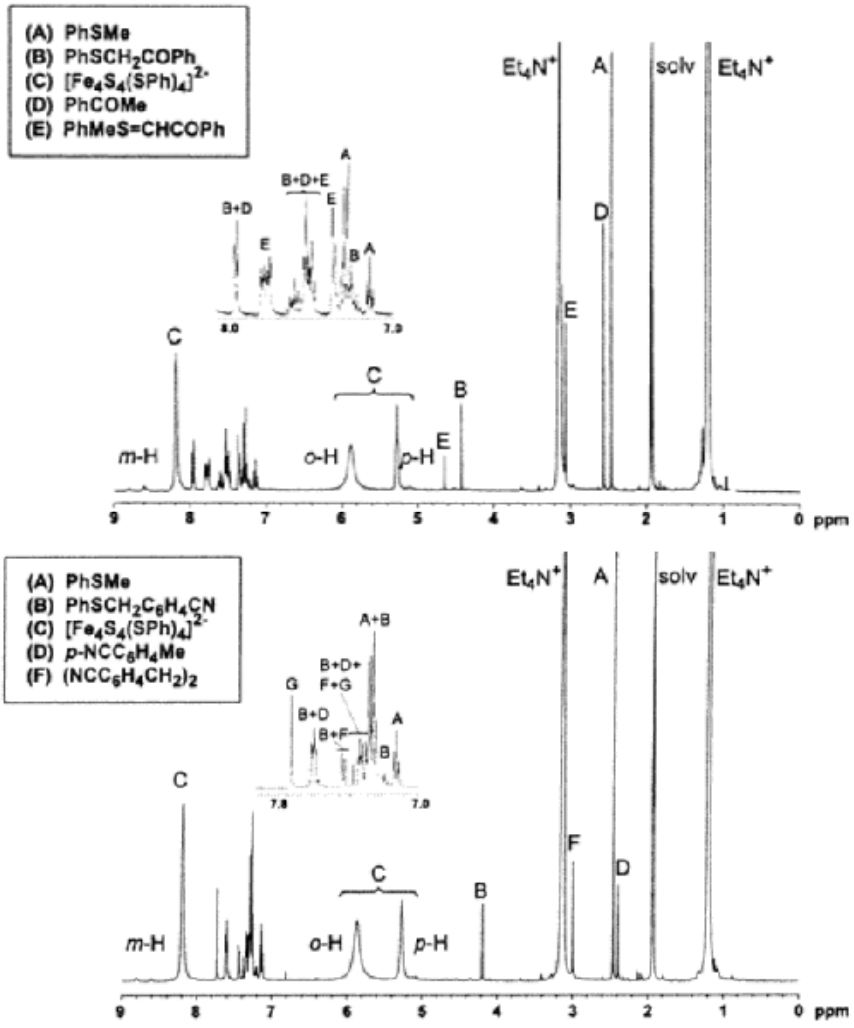

Figure 1.11 ^{1}H NMR spectra of the reaction systems $[Fe_4S_4(SPh)_4]^{3-}$/$[PhMeSCH_2R]^{+}$ (R = COPh **3** (Upper), p-C_6H_4CN **4** (Down) in acetonitrile solutions. Reactants were present in equimolar concentration. Signal assignments are indicated; insets show expanded aromatic proton regions.[36]

As for the fate of carbanion $RCH_2:^{-}$, there are two possibilities, both involve nucleophilic attack of $RCH_2:^{-}$ on second equivalent of sulfonium cation (Scheme 1.5 (e)). The first attack happens on the carbon of methylene group adjacent to sulfur (**R-5**), which cleaves S-C bond and generates products of RCH_2CH_2R and PhSMe (same as products of first-electron reduction)**.** The second possibility is nucleophilic attack on relatively acidic α-hydrogen coming from electron-withdrawing phenacyl group.[37] The withdrawal of α-

hydrogen can push electron to flow to S−C bond and form RCH_3 and ylid **5** (PhMeS=CHR) (corresponding to signal E in Figure 1.11 (Upper) (**R-6**):

$$RCH_2{:}^- + [PhMeSCH_2R]^+ \rightarrow PhSMe + RCH_2CH_2R \quad (\textbf{R-5})$$

$$RCH_2{:}^- + [PhMeSCH_2R]^+ \rightarrow RCH_3 + PhMeS{=}CHR \quad (\textbf{R-6})$$

Summarizing the stepwise reactions, Holm's group provided the following full reactions (**R-7**&**8**):[36]

$$2[Fe_4S_4(SPh)_4]^{3-} + 2[PhMeSCH_2R]^+ \rightarrow 2[Fe_4S_4(SPh)_4]^{2-} + 2PhSMe + RCH_2CH_2R \quad (\textbf{R-7})$$

$$2[Fe_4S_4(SPh)_4]^{3-} + 2[PhMeSCH_2R]^+ \rightarrow 2[Fe_4S_4(SPh)_4]^{2-} + PhSMe + RCH_3 + PhMe{=}CHR \quad (\textbf{R-8})$$

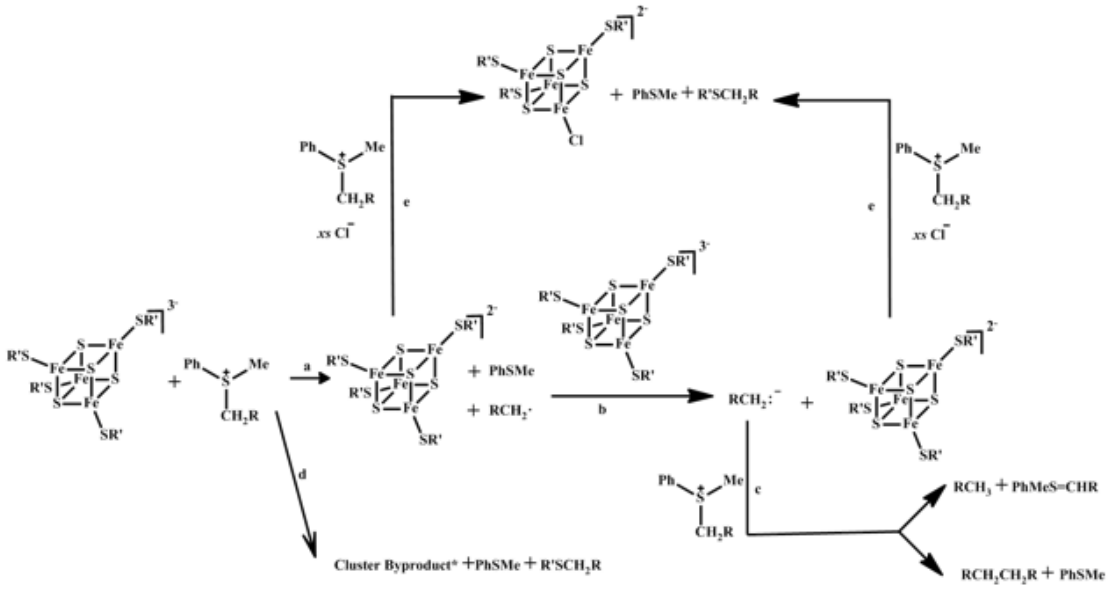

Scheme 1.5 Reaction pathway in $[Fe_4S_4(SPh)_4]^{3-}$/ $[PhMeSCH_2R]^+$ system. (a) Electron transfer reaction. (b) Second (fast) electron transfer reaction. (c) Quenching of sulfonium cation. (d) Terminal thiolate attack from reduced cluster. (e) Terminal thiolate attack from oxidized cluster (cluster decomposition observed in absence of added chloride to the reaction mixture).

Considering the product distribution, **R-8** is dominant for **2**/**3** system. While the acidity of sulfonium **4** is smaller in relative with **3**, so **R-7** accounts more for **2**/**4** system, the NMR data also reflects this tendency due to the absence of product **5** PhMeS=CHR

in Figure 1.11(Down).

In 2003, Holm conducted a similar study using a 3:1 site-differentiated $[Fe_4S_4]^{1+}$ cluster with a semirigid trithiolate ligand ($L(SH)_3$) coordinated in a trigonally symmetric arrangment (Figure 1.12).[38] In this model system, they observed similar two-electron chemistry with sulfonium cations. The isolation of the products as NBu^+ salts, characterization with electrochemistry, and spectroscopic analysis (EPR, ^1H NMR and Mössbauer) confirmed their results.

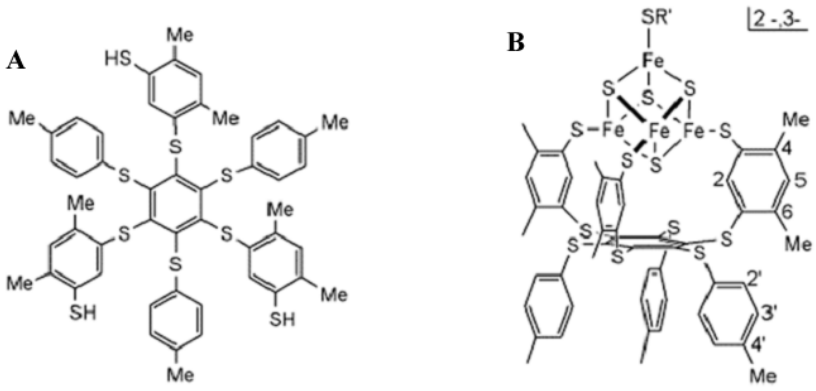

Figure 1.12 Trithiol $L(SH)_3$ (**A**) and 3:1 substite-differentiated clusters $[Fe_4S_4(LS_3)(SR')]^{2-/3-}$(**B**).[38]

In summary, Holm and coworkers demonstrated the ability of synthetic $[Fe_4S_4]^{1+}$ clusters to cleave sulfonium cations in overall two-electron reactions, on the basis of product analysis.[36, 38] And unlike one-electron reduction cleavage and the formation of a stable 5'-Ado· radical in SAM enzymes, the two-electron processes observed in these models are due to the inability to stabilize the radical product prior to the fast second reduction to form the carbanion $RCH_2:^-$.

1.4 Specific Aims of our Research

Biomimetic studies of the radical SAM enzymes have been hindered due to the difficulty in preparing suitable synthetic [Fe_4S_4] clusters. To date, biomimetic studies of radical SAM enzymes have been limited to two reports by Daley and Holm discussed above.[39] These researchers found that synthetic [$Fe_4S_4(SR')_4$] (R'=Ph, Et) clusters react with sulfonium cations to yield a mixture of products arising from (i) electrophilic attack of the sulfonium group on the thiolate ligands, and (ii) two-electron reduction of the sulfonium cation by two equivalents of [Fe_4S_4] cluster. Neither pathway mimics the mechanism of the radical SAM enzymes, which involves one-electron reduction of the sulfonium group by the [Fe_4S_4] cluster to give a carbon-based radical. Structurally, the synthetic clusters generated by Holm and others lack the all-important unique Fe centers capable of coordinating biologically-relevant ligands like the SAM cofactor. Thus, the electron transfers occur via an outer-sphere mechanism, in contrast to the inner-sphere transfer that occurs in the enzymatic systems. In addition, the redox potentials of these synthetic clusters tend to be dramatically more negative than their biological counterparts.

Due to the limitation in using synthetic [Fe_4S_4] clusters to mimic radical SAM enzymes, we have pursued a different and simplified approach to modeling these active sites. Our strategy is based on the assumption that *it is only necessary to model the unique Fe center of the biological cluster in order to obtain valuable insights into the catalytic mechanism of radical SAM enzymes*. These synthetic models must incorporate three critical features of the biological unique Fe center: (i) coordinative unsaturation, such that the Fe center can bind exogenous ligands with sulfonium groups, (ii) a high-

spin state, and (iii) a low redox potential near the value measured for the enzymes (ca. -0.70 mV vs SCE). The following chapters of this report will discuss the design, synthesis, and characterization of such complexes, as well as their reactivity with sulfonium salts.

Chapter 2*: Synthesis of Low-potential Mono-iron(II) complexes*. High-spin Fe(II) complexes with neutral or monoanionic coordination environments generally have $Fe^{2+/3+}$ redox potential greater than +0.6 V vs SHE. In order to obtain mononuclear Fe(II) complexes with reduced potentials near those measured for biological $[Fe_4S_4]$ clusters, we have employed the tripodal ligands (**H_3L^n;** n = 1-5) that feature three phenolate rings appended to a tertiary amine (Figure 1.13). These tetradentate ligands coordinate in a trigonal pyramidal fashion, thereby rendering a vacant coordination site *trans* to the nitrogen donor. Therefore, these complexes replicate the geometry of the unique Fe centers found in radical SAM enzymes. Importantly, the size of this cavity can be adjusted by varying the size of the substituent at the 2-position of phenolate rings (**H_3L^1** and **H_3L^2**).

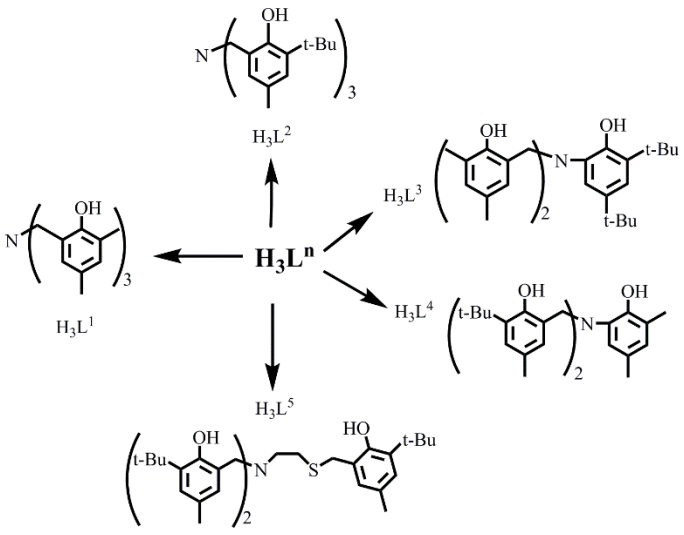

Figure 1.13 Structures of Amine tris(phenolate) ligands **H_3L^n** (**n**=1-5).

On the basis of ligand designs, a novel series of Fe(II) complexes that fulfill the three criteria established above have been prepared, as one example shown in Figure 1.14. The resulting complexes were characterized by X-ray crystallography, paramagnetic nuclear magnetic resonance (NMR) spectroscopy, electronic absorption spectroscopy, and electrochemical studies.

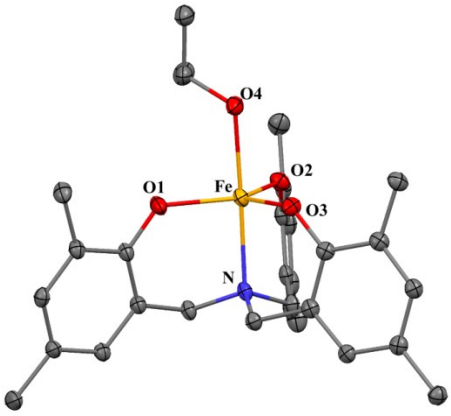

Figure 1.14 Thermal ellipsoid plots (50% probability) derived from the X-ray crystal structures of complexes [**1**]NEt_4 ($FeCl_2$ reacted with H_3L^1 listed in chapter 2 in detail). Non-coordinating solvent molecules, counterions, and most hydrogen atoms have been omitted for clarity.

Chapter 3*: Reactivity of [1]NEt_4 complexes with sulfonium salts.* To determine whether our synthetic models are capable of reductively cleaving S-C bonds to generate radical species, we have prepared the sulfonium cations shown in Figure 1.15. Like SAM itself, these cations contain metal-binding moieties, such as pyridyl rings, that positions the reactive sulfonium group close to the Fe(II) center. The cations differ with respect to the identity of the metal-binding group, the strength of the S-C bonds, and the distance of the S-atom from the Fe(II) ion in the putative Fe/sulfonium adduct.

We measured reaction rates for various sulfonium cations by monitoring changes in UV-visible absorption features as a function of time. These kinetics allowed us to

quantitively evaluate the effect of Fe···S distances on the rate of electron transfer. The products resulting from the reaction of these sulfonium cations with [**1**]NEt_4 were characterized with gas chromatography-mass spectrometry (GC-MS) and ^1H NMR. Furthermore, we performed reactions in the presence of organic compounds that serve as "radical traps" to detect whether cleavage of the S-C bond occurs via one–electron transfer to yield a carbon-based radical (as occurs in biological enzymes), or via a two-electron processes (as in Holm's system). All of these results will have major implications for our understanding of electron transfer in radical SAM enzymes.

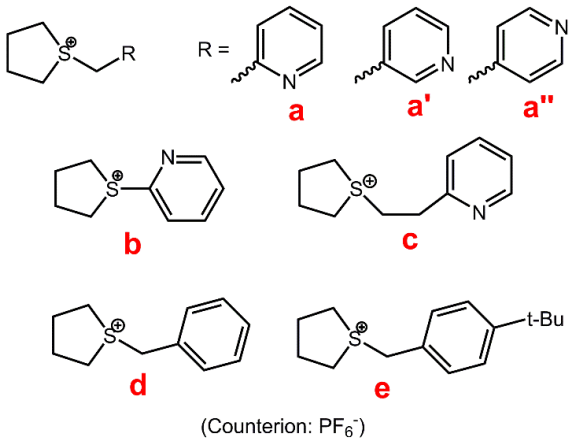

Figure 1.15 Structures of sulfonium cations (**a-e**).

Chapter II

Synthesis and Characterization of Low-Potential Fe(II) Complexes with Tris(2-hydroxybenzyl)amine Ligands

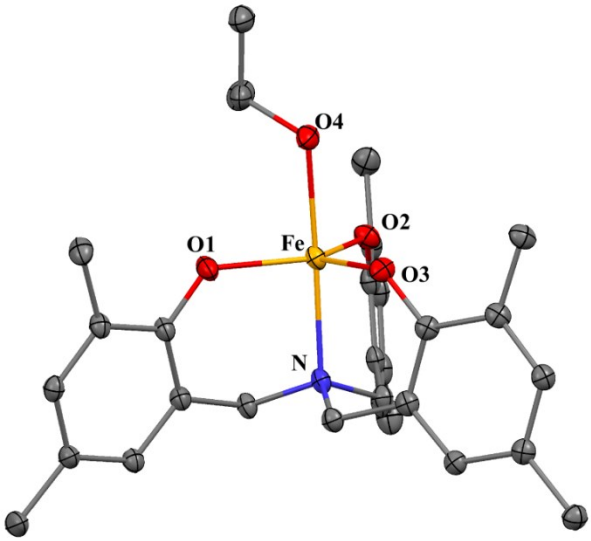

Abstract: A novel series of Fe(II) complexes with tripodal tris(2-hydroxybenzyl)amine ligands, which replicate the geometry of the unique Fe centers found in radical SAM enzymes, have been prepared. The resulting complexes were characterized by X-ray crystallography, paramagnetic ^{1}HNMR spectroscopy, electronic absorption spectroscopy, and electrochemical methods. The complexes were evaluated by three criteria established to model the unique Fe sites in radical SAM proteins: i) a high spin state, ii) a low redox potential near the value measured for the enzymes (ca. -0.70 V vs SCE), and iii) coordinative unsaturation, such that Fe center can bind exogenous ligands with sulfonium cations.

2.1 Introduction

Due to the participation of radical SAM enzymes in tremendously significant biological processes, considerable attention has been devoted to the mechanism of reductive SAM cleavage by $[Fe_4S_4]^{1+}$ clusters. Studies involving synthetic models have been hindered, however, by the difficulty in generating Fe/S clusters that contain a "unique" Fe center capable of interacting with sulfonium cations.[36] My research has employed a novel and simplified strategy for modeling the unique Fe active site. These complexes must meet three criteria to be considered appropriate models: i) the Fe center(s) should have high-spin, ferrous states, ii) the redox potential should lie near the value measured for the enzymes (ca. -0.70 mV vs SCE), and iii) the complexes should exhibit coordinative unsaturation, such that the Fe center can bind exogenous ligands containing sulfonium units.

Generally, high-spin Fe(II) complexes with neutral or monoanionic coordination environments have $Fe^{2+/3+}$ redox potentials greater than +0.6 V vs SHE. To lower the potential of our mono- and dinuclear Fe(II) complexes, we have utilized various trianionic ligands based on the tris(2-hydroxybenzyl)amine motif. Ferric complexes with such ligands have been previously reported in the literature. An early synthetic and electrochemical study involved the Fe(III) complex **1A-Meim** shown in Figure 2.1.[40] In general, the chemistry of symmetric trisphenolate NO_3-type ligands has received considerable attention due to its rich coordination chemistry with various transition metals.[41] For instance, titanium complexes with NO_3 ligands serve as catalysts for aza-Diels-Alder[42] and sulfoxidation[43] reactions. Tris(phenolate)amines have also been used to mimic the coordination spheres of metalloprotein active sites such as haloperoxidases

(a vanadium-dependent enzyme)[44] and Fe-containing intradiol catechol dioxygenases.[45,46] Phenolate substituents with different steric bulk have been shown to modify the steric and electronic properties of the metal complexes, thus influencing binding modes, conformation changes, and overall stability.[44] Because of the difficulty in isolating four-coordinate iron complexes with trisphenolate NO_3 ligands, few such Fe complexes were characterized until Prof. Stephen Koch's group reported complex **1A-Meim** in 1998 (Figure 2.1).[40] In the X-ray structure of **1A-Meim**, the five-coordinate Fe(III) center exhibits a trigonal bipyramidal geometry with N1(amine) and N2 (1-methylimidazole) in the axial positions (the N1-Fe1-N2 bond angle is 173.4(1)º. Three oxygen atoms from the phenolate donors reside in the equatorial plane with O-Fe1-O bond angles between 117.4(1)º and 126.3(1)º. Cyclic voltammetry experiments of **1A-Meim** showed a quasi-reversible $Fe^{3+/2+}$ redox couple at $E_{1/2}$= -0.78 V (vs Ag/AgCl) in DMF solution.[40]

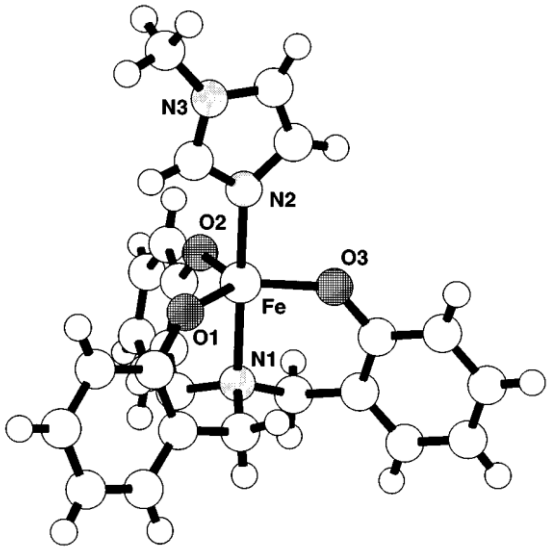

Figure 2.1 Structural diagram for [Fe{N(CH_2-o-$C_6H_4O)_3$}(1-Meim)] (**1A-Meim**).[40]

To the best of our knowledge, examples of ferrous complexes with tripodal tris(2-hydroxybenzyl)amine ligands have not been reported. In this chapter, we present the synthesis and characterization of ligands H_3L^n (n = 1-5; see Figure 2.2) and the corresponding Fe complexes.

2.2 Results and Discussion

2.2.A Syntheses of Ligands and $Fe^{3+/2+}$ Complexes

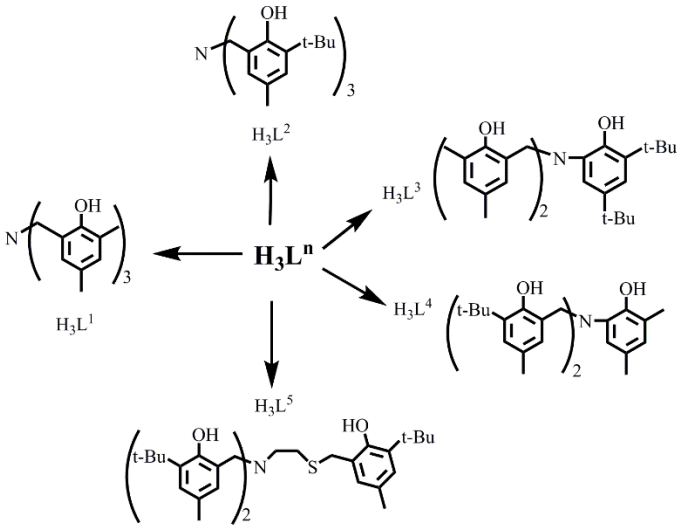

Figure 2.2 Ligand design of **H_3L^n (n**=1-5).

In this chapter, we have modeled the unique Fe center of SAM-dependent enzymes with four classes of phenolate-based ligands: symmetric NO_3 ($H_3L^{\mathbf{1}}$, $H_3L^{\mathbf{2}}$), asymmetric NO_3 ($H_3L^{\mathbf{3}}$, $H_3L^{\mathbf{4}}$), and pentadentate NO_3S ($H_3L^{\mathbf{5}}$) ligands. For the first type, we generated the symmetric ligands with different steric bulk via a modified Mannich reaction between hexamethylene tetraamine, 36 % aqueous formaldehyde, and the

corresponding substituted phenol with either methyl or tert-butyl substituents in *ortho* positions to the phenolate O-atom.[47] In order to alter the topology of the phenolate donors, two asymmetric ligands ($H_3L^{\mathbf{3}}$, $H_3L^{\mathbf{4}}$) were designed, which required the synthesis of substituted *o*-aminophenol and 2-(chloromethyl)phenol precursors. In the case of H_3L^5, 2-mercaptoethylamine was reacted with three equivalents of 2-(chloromethyl)-4,6-dimethylphenol to generate new type of pentacoordinate ligand. The inclusion of a sulfur donor in H_3L^5 is intended to better mimic the active site structure of radical SAM enzymes.

The preparations of $Fe^{3+/2+}$ complexes with $(\mathbf{L^n})^{3-}$ ligands follow the same general procedure: $\mathbf{H_3L^n}$ (1.0 mmol) was dissolved in 20.0 ml anhydrous methanol and deprotonated with sodium methoxide (3.0 mmol) in glovebox of nitrogen pressure. To the resulting solution were added $FeCl_3/FeCl_2$ (1.0 mmol) (For the Fe(II) complexes, one equivalent NEt_4Cl or PPh_4Br was added to provide a suitable countercation for crystallographic studies. After stirring the mixture at room temperature overnight and removal of the solvent under vacuum, the yellow-colored solid was redissolved in acetone, filtered through celite and dried under vacuum. X-ray quality crystals were obtained using different solvents.

2.2.B X-ray Structural Characterization

2.2.B.1 Mononuclear Fe(II) and Fe(III) Complexes

For the sake of clarity, we will first discuss the monoiron(II) complexes $[Fe(L^{\mathbf{1}})]NEt_4$ ($[\mathbf{1}]NEt_4$) (product of $FeCl_2$ reacting with H_3L^1) and $[Fe(L^{\mathbf{2}})]PPh_4$

([**2**]PPh$_4$). The molecular structures of these complexes are shown in Figure 2.3, while selected bond distances (Å) and angles (º) for these complexes are provided in Table 2.1. Details concerning the X-ray data collection and analysis are summarized in Table 2.6 of the Experimental Section.

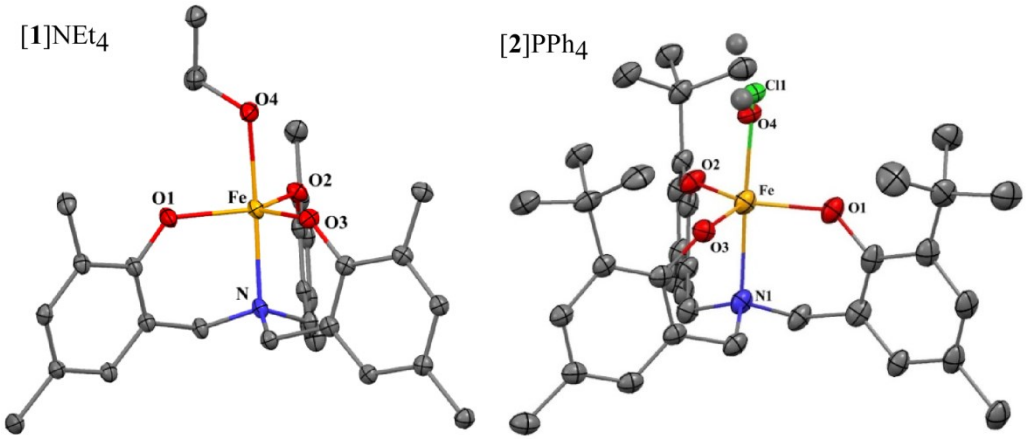

Figure 2.3 Thermal ellipsoid plots (50% probability) derived from the X-ray crystal structures of complexes [**1**]NEt$_4$ and [**2**]PPh$_4$. Non-coordinating solvent molecules, counterions, and most hydrogen atoms have been omitted for clarity. For complex [**2**]PPh$_4$, the Fe site contains 70% Fe(III) and 30% Fe(II).

The X-ray structure of [**1**]NEt$_4$ features two symmetry-independent [**1**]$^-$ complexes in the asymmetric unit with nearly identical geometries. As shown in Figure 2.3 (left), complex [**1**]$^-$ has an idealized trigonal bipyramidal geometry with a solvent-derived isopropanol ligand in the axial position *trans* to the amine N-atom (the N(1)−Fe−O(4) bond angle is 173.53º). The equatorial FeO_3 plane shows small deviations from C_3 symmetry with O−Fe−O angles ranging from 111.12(13)º to 131.49(14)º. The Fe atom is slightly below the plane of three oxygen donor atoms with an Fe(1)-N(1) distance of 2.212(3) Å. The average equatorial Fe−O distance of 1.995 Å is 0.32 Å

shorter than average Fe-S distance in the known four-coordinate complex $[Fe^{II}(N(CH_2\text{-}o\text{-}C_6H_4S)_3)]^-$;[48] this difference is consistent with the different donor abilities of phenolates and phenylthiolates. The Fe−O/N bond distances are typical of high-spin Fe(II) centers with four unpaired electrons ($S = 2$), and the wide distribution of chemical shifts observed in the ^{1}H NMR spectrum also reflects its paramagnetic nature (*vide infra*). The isopropanol ligand coordinated at the axial position is labile and easily displaced by other substrates.

Table 2.1 Selected bond distance (Å) and angles (º) for complexes [**1**]NEt_4 and [**2**]PPh_4.

	[**1**]NEt_4	[**2**]PPh_4[a]	[**3**]PPh_4	**4**
Bond Distance (Å)				
Fe(1)-O(1)	1.963(3)	1.885(4)	1.874(2)	1.866(3)
Fe(1)-O(2)	1.981(3)	1.883(3)	1.873(2)	1.909(3)
Fe(1)-O(3)	2.042(3)	1.886(4)	1.874(2)	1.847(3)
Fe(1)-N(1)	2.212(3)	2.287(5)	2.317(2)	2.172(2)
Fe(1)-O(4)/Cl(1)[a]	2.190(3)	2.485(3)	2.3524(7)	2.070(3)
Bond Angles (º)				
O(1)-Fe(1)-O(2)	131.49(14)	124.33(19)	123.36(8)	119.84(14)
O(1)-Fe(1)-O(3)	117.37(13)	119.33(16)	119.01(7)	117.62(13)
O(2)-Fe(1)-O(3)	111.12(13)	115.22(19)	116.01(8)	122.55(19)
O(1)-Fe(1)-N(1)	90.60(12)	85.63(18)	85.69(7)	90.2(1)
O(2)-Fe(1)-N(1)	89.52(12)	86.31(16)	86.69(7)	90.9(1)
O(3)-Fe(1)-N(1)	91.41(11)	87.62(17)	84.99(7)	88.9(1)
O(1)-Fe(1)-O(4)/Cl(1)[a]	91.85(13)	92.1(2)	94.05(5)	89.9(1)
O(2)-Fe(1)-O(4)/Cl(1)[a]	88.64(12)	94.3(2)	95.27(6)	94.9(2)
O(3)-Fe(1)-O(4)/Cl(1)[a]	81.71(12)	94.2(1)	93.43(5)	85.1(2)
N(1)-Fe(1)-O(4)/Cl(1)[a]	173.53(12)	177.6(2)	177.92(5)	173.3(1)

[a] For [**2**]PPh_4, the axial position is disordered with 70:30 Cl:MeOH ligands. Data is only given for the chloride-containing species.

With the same type of NO_3 donor set as [**1**]NEt_4, complex [**2**]$^-$ also displays a trigonal bipyramidal geometry, although the *ortho* positions on three phenolate rings are now occupied by bulky *tert*-butyl groups. The disorder in the structure arises from partial oxidation of the ferrous center, resulting in a 70:30 superposition of Fe(III) and Fe(II) structures. The axial position is occupied by chloride in the Fe(III) structure, while MeOH occupies this site in the Fe(II) complex; thus, the overall charges of the two species are identical. The Fe center was likely oxidized by dichloromethane (employed as a crystallization solvent), or excess Cl^- from $FeCl_2$ or NEt_4Cl. Indeed, we found that prolonged exposure of [**1**]$^-$ and [**2**]$^-$ to chlorinated solvents results in oxidation due (presumably) to reductive clevage of the C-Cl bond – a result that highlights the reductive nature of Fe(II) complexes with tris(2-hydroxybenzyl)amine ligands. The FeO_3 plane in [**2**]$^{0/-}$ exhibits a C_3 conformation with almost identical Fe-O lengths and O-Fe-O bond angles. The shorter average Fe-O(equatorial) distance of 1.885 Å (compared to 1.995 Å in [**1**]$^-$) reflects the increase in Fe oxidation state. Viewing a space-filling model of the crystal structure, it is evident that the three bulky *tert*-butyl groups exert large steric hindrance on the axial position.

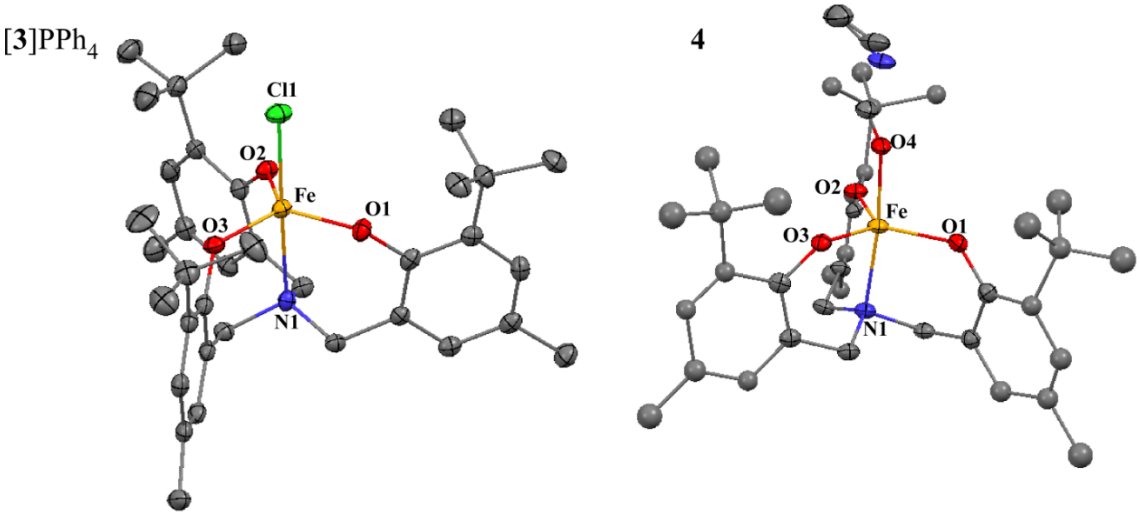

Figure 2.4 Thermal ellipsoid plots (40% probability) derived from the X-ray crystal structures of complexes [**3**]PPh_4 and [**4**]. Non-coordinating solvent molecules, counterions, and most hydrogen atoms have been omitted for clarity.

While attempting to obtain a crystal structure of the ferrous complex $[\mathbf{2}]^-$ without ferric contamination has not been successful, we have grown "pure" crystals of the ferric complex $[FeCl(L^2)]PPh_4$ ([**3**]PPh_4; see Figure 2.4). Not surprisingly, the metric parameters of [**3**]PPh_4 closely match those found for [**2**]PPh_4 (Table 2.1). We have also generated the neutral ferric complex $[Fe(L^2)(DMF)]$ (**4**), in which the axial position is occupied by DMF (Figure 2.4). Despite the change in the identity of the axial ligand (chloride versus DMF), the Fe–O/N distances and bond angles are very similar in [**3**]PPh_4 and **4** (Table 2.1).

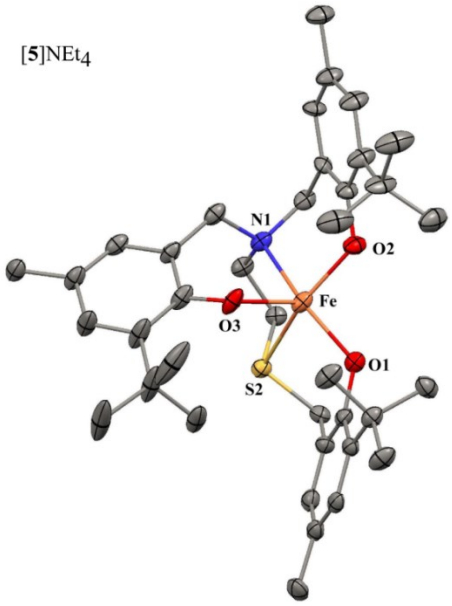

Figure 2.5 Thermal ellipsoid plots (40% probability) derived from the X-ray crystal structures of complex [**5**]NEt_4. Non-coordinating solvent molecules, counterions, and most hydrogen atoms have been omitted for clarity.

With the aim of including sulfur donors in the Fe coordination sphere, we prepared the pentadentate H_3L^5 ligand that contains a thioether moiety. The X-ray structure of the resulting Fe(II) complex, [Fe(L^5)]NEt_4 ([**5**]NEt_4), is shown in Figure 2.5; selected bond distances and angles are provided in Table 2.2. Unfortunately, the *R*-value of the structure (17%) is quite large due to poor crystal quality, resulting in large uncertainties in bond lengths and angles. Complex [**5**]NEt_4 exhibits a distorted square-pyramidal geometry in which one of the amine-appended phenolate donors lies in the axial position. The O_2NS equatorial plane features basal O(2)−Fe(1)−S(2) and O(1)−Fe(1)−N(1) angles of 148.1(2) and 149.1(2)°, respectively. Similar to [**1**]NEt_4, the Fe(II)-phenolate bonds in [**5**]$^-$ display distances near 2.0 Å, while the Fe–N(amine) bond length is elongated to ~2.30 Å. The Fe–S bond is quite lengthy at 2.681(3) Å, reflecting the weak donor strength of thioether groups. This NSO_3 ligand environment around an

Fe(II) center is unprecedented to our knowledge, and there is no reference data for comparison.

Table 2.2 Selected bond distance (Å) and angles (º) for complex [**5**]NEt_4.

	[**5**]NEt_4
Bond Distance (Å)	
Fe(1)-O(1)	1.969(6)
Fe(1)-O(2)	1.946(7)
Fe(1)-O(3)	1.978(7)
Fe(1)-N(1)	2.301(7)
Fe(1)-S(1)	2.681(3)
O(1)-Fe(1)-O(2)	93.4(3)
O(1)-Fe(1)-O(3)	118.9(3)
O(2)-Fe(1)-O(3)	115.1(3)
O(1)-Fe(1)-N(1)	149.1(2)
O(2)-Fe(1)-N(1)	89.3(3)
O(3)-Fe(1)-N(1)	87.2(3)
O(1)-Fe(1)-S(1)	84.8(2)
O(2)-Fe(1)-S(1)	148.1(2)
O(3)-Fe(1)-S(1)	115.1(3)
N(1)-Fe(1)-S(1)	77.0(2)

2.2.B.2 Dinuclear Fe Complexes

Unexpectedly, the reaction of $FeCl_2$ with the asymmetric NO_3 ligands H_3L^3 and H_3L^4 in the presence of base (3 equivalences of NaOMe) generated the yellow diiron(II) complexes [**6**]$(NEt_4)_2$ and [**7**]$(NEt_4)_2$, respectively (NEt_4Cl was added to provide a suitable countercation). Both complexes feature $Fe_2(\mu$-phenolate$)_2$ cores with Fe1···Fe1A separations of ~3.2 Å; an idealized C_2 axis lies perpendicular to the $Fe_2(\mu$-$O)_2$ plane (Figure 2.6). The lack of a methylene spacer between the amine N and phenolate ring

apparently opens up the coordination sphere around the Fe centers, thus permitting dimerization of the $Fe(NO_3)$ units.

For both complexes, the less sterically-hindered 4,6-dimethylphenolates occupy the bridging positions. The Fe(II) centers are five-coordinate with geometries intermediate between square-pyramidal and trigonal-bipyramidal (τ-values of 0.40 for [**6**]$(NEt_4)_2$ and 0.22 for [**7**]$(NEt_4)_2$). The Fe_2O_2 core is essentially planar in $[\mathbf{6}]^{2-}$ with a Fe1-O2-Fe1A-O2A dihedral angle of 15°, while the Fe_2O_2 core in $[\mathbf{7}]^{2-}$ is more puckered with a dihedral angle of 31°. As were the cases for the monoiron(II) complexes, the terminal Fe-O bond lengths lie near 2.0 Å. Distances between the Fe(II) centers and the bridging O-atoms are slightly longer, with an average value of 2.09 Å. Such metric parameters suggest that the Fe(II) centers are high-spin, especially considering the lengthy Fe-N distances of ~2.23 Å.

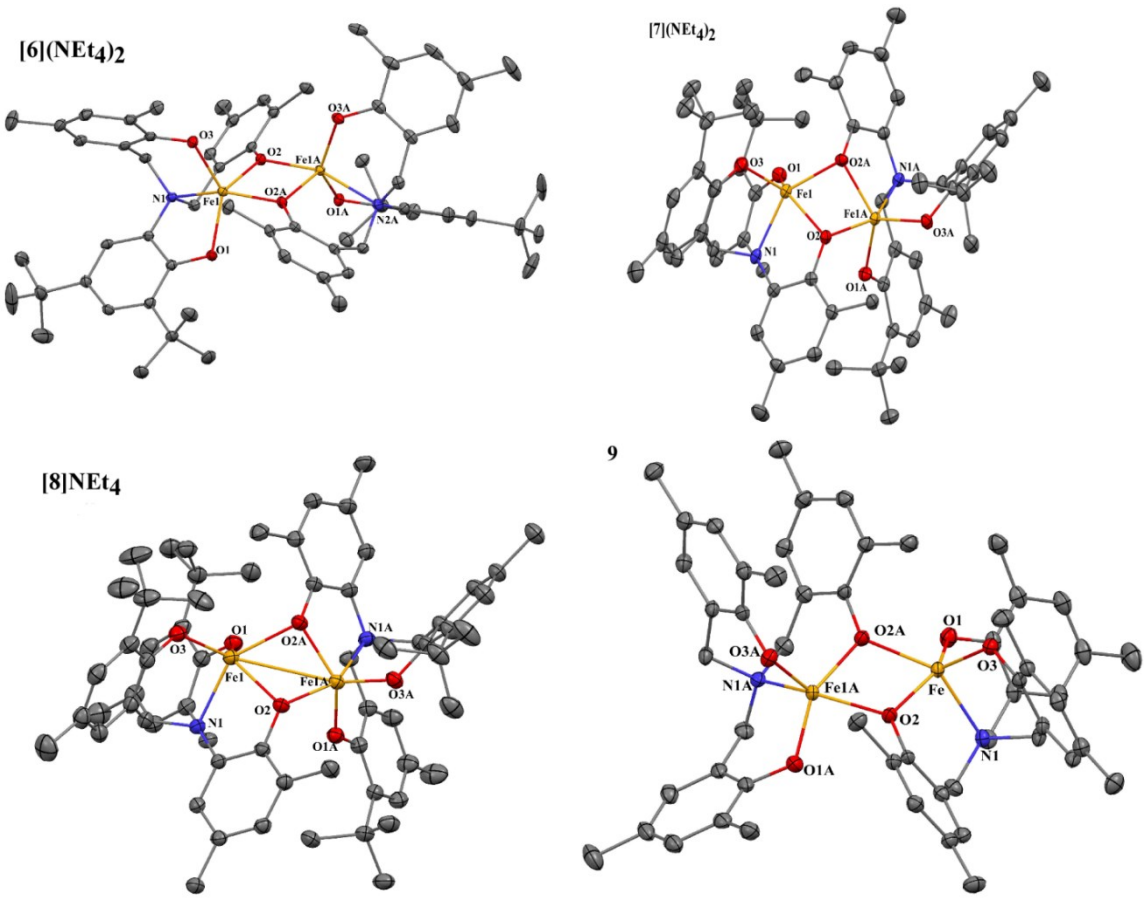

Figure 2.6 Thermal ellipsoid plots (50% probability) derived from the X-ray crystal structures of dinuclear complexes [**6**]$(NEt_4)_2$, [**7**]$(NEt_4)_2$**,** [**8**]NEt_4 and **9**. Non-coordinating solvent molecules, counterions, and most hydrogen atoms have been omitted for clarity.

Interestingly, a MeCN solution of [**7**]$(NEt_4)_2$ that had been sitting in glovebox freezer for several weeks provided dark red crystals that were clearly distinct from those originally obtained for the diiron(II) complex. XRD analysis revealed that the crystals correspond to the one-electron oxidized derivative of $[\mathbf{7}]^{2-}$, e.g. $[Fe_2(\mathbf{L^4})_2]NEt_4$ ([**8**]NEt_4). This result further highlights the oxidative sensitivity of ferrous complexes with trianionic NO_3 ligands, since the O_2 concentration in our glovebox is less than one ppm. The molecule has a local two-fold symmetry with a Fe···Fe separations of 3.05 Å.

However, the coordination environments of Fe1 and Fe1A are distinctly different. As shown in Table 2.2, the Fe1-$O_{phenolate}$ bonds are considerably longer than the Fe2-$O_{phenolate}$ bonds (average lengths of 2.056 Å and 1.930 Å, respectively). This result indicates an absence of electron delocalization in the mixed-valence complex, such that we can assign Fe1 to the ferrous state and Fe1A to the ferric state. Similar to the diiron(II) complexes, the Fe centers in [**8**]NEt_4 have coordination geometries intermediate between trigonal-bipyramidal and square-pyramidal.

As noted above, Fe(III) complexes with tris(2-hydroxybenzyl)amine ligands have been studied extensively.[40,49,50] Generally, these complexes are prepared by reaction $FeCl_3$ with the NO_3 ligand in the presence of base (3 equivalences) and an axial donor, such as 1-methylimidazole (1-Meim). The procedure has afforded mononuclear, five-coordinate complexes like **1A-Meim** (Figure 2.1). We attempted to prepare analogous complexes, but *without* a strongly-donating axial ligand. Interestingly, reaction of H_3L^1 with $FeCl_3$ and base in MeOH provided the diiron(III) complex $[Fe_2(L^{\mathbf{1}})_2]$ (**9**), as shown in Figure 2.6. As with the diiron complexes discussed above, the Fe centers are bridged by two phenolate ligands and the complex has C_2 symmetry. Metric parameters for **9** are provided in Table 2.2. The short average Fe-$O_{phenolate}$ distance of 1.935 Å is typical of such bonds in high-spin ferric complexes. The geometry of the five-coordinate Fe(III) centers is distorted square-pyramidal (τ-value of 0.08).

In summary, we have succeeded in preparing a series of diiron complexes in three distinct oxidation states: diferrous, diferric, and mixed-valences. Such complexes nicely model a fragment of the $[Fe_4S_4]$ cluster found in the active sites of radical SAM enzymes.

Table 2.3 Selected bond distance (Å) and angles (º)[a] for complexes [**6**]$(NEt_4)_2$, [**7**]$(NEt_4)_2$, [**8**]NEt_4, and **9**.

Complexes	[**6**]$(NEt_4)_2$	[**7**]$(NEt_4)_2$	[**8**]NEt_4	**9**
Oxidation States	Fe^{2+}/Fe^{2+}	Fe^{2+}/Fe^{2+}	Fe^{2+}/Fe^{3+}	Fe^{3+}/Fe^{3+}
Bond Distance (Å)				
Fe(1)-O(1)	2.005(1)	2.034(2)	2.008(1)	1.872(2)
Fe(1)-O(2) [bridging]	2.045(1)	2.108(2)	2.136(1)	1.989(2)
Fe(1)-O(3)	1.984(1)	1.983(2)	1.924(1)	1.851(2)
Fe(1)-O(2A) [bridging]	2.104(1)	2.097(2)	2.159(1)	2.029(2)
Fe(1)-N(1)	2.231(2)	2.186(2)	2.185(1)	2.173(2)
Fe(1A)-O(2) [bridging]	2.113(1)	2.096(2)	1.988(1)	1.989(2)
Fe(1A)-O(1A)	2.000(1)	1.948(2)	1.890(1)	1.872(2)
Fe(1A)-O(2A) [bridging]	2.074(1)	2.066(2)	1.972(1)	2.029(2)
Fe(1A)-O(3A)	1.985(1)	2.028(2)	1.874(1)	1.851(2)
Fe(1A)-N(1A)	2.236(2)	2.209(2)	2.192(1)	2.173(2)
Fe(1)···Fe(1A)	3.206	3.163	3.052	3.212
Bond Angles (º)				
O(1)-Fe(1)-O(2)	126.62(5)	129.03(6)		146.01(7)
O(1)-Fe(1)-O(3)	130.01(5)	108.50(7)		108.83(8)
O(1)-Fe(1)-N(1)	77.66(5)	91.38(7)		91.20(8)
O(1)-Fe(1)-O(2A)	84.07(5)	87.03(6)		86.35(7)
O(2)-Fe(1)-O(3)	102.17(5)	121.61(7)		105.00(7)
O(2)-Fe(1)-N(1)	94.04(5)	78.02(6)		89.21(7)
O(2)-Fe(1)-O(1A)	77.94(5)	74.10(6)		72.56(7)
O(3)-Fe(1)-N(1)	89.96(5)	93.08(7)		94.71(7)
O(3)-Fe(1)-O(2A)	119.95(5)	123.01(6)		122.74(7)
N(1)-Fe(1)-O(2A)	149.96(5)	142.37(6)		141.15(7)
τ-value	0.44	0.22		0.08

[a] Angles only provided for the Fe(1) center.

2.2.C Nuclear Magnetic Resonance (NMR) Spectroscopy Data

In order to confirm high spin Fe(II) center, we did paramagnetic ^1H NMR in Methanol-d_4 solutions for ferrous complexes. Except for complex **2**, all the spectra

exhibit largely down-field shifts, which indicates Fe(II) center has high spin S=2. In Figure 2.7, [**1**]NEt_4 displays an example.

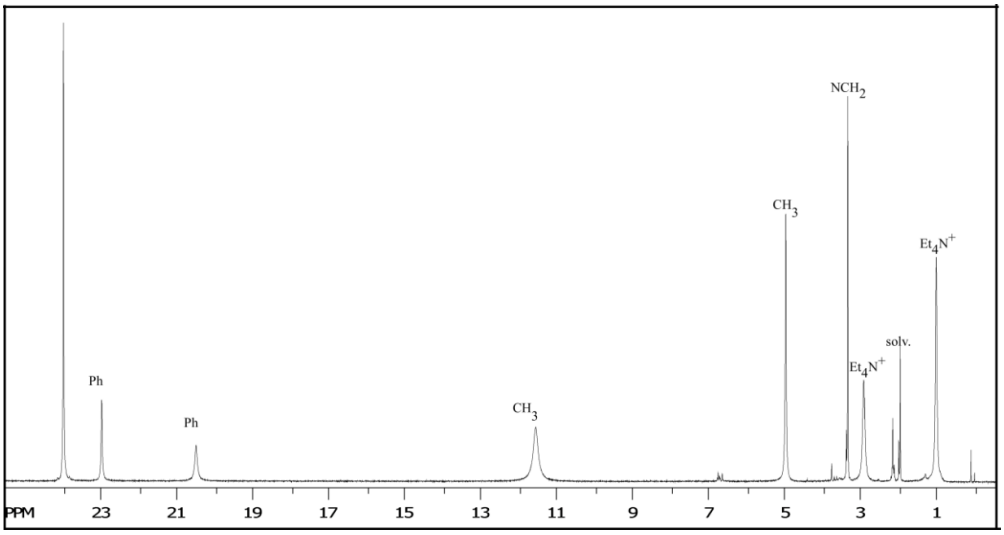

Figure 2.7 ^{1}H NMR spectra of [**1**]NEt_4 in Methanol-d_4.

2.2.D Cyclic Voltammetry Data

As mentioned in previous chapter, an important criterion for modeling the unique Fe site of $[Fe_4S_4]$ clusters is to generate complexes with low redox potential near the value measured for enzymes (ca. -1.1 V vs $Fc^{+/0}$). The cyclic voltammetry data (CVs) of our Fe(II) complexes in DMF with different ligands are depicted in Figure 2.8, and the peak potentials are listed in Table 2.4. Potentials are referenced to the ferrocene/ferrocenium ($Fc^{+/0}$) couple. All complexes exhibit at least one quasi-reversible oxidation (termed "couple 1": 1_{ox} and 1_{red}) in the range of -1.2 to -1.4 V. An exception is complex [**2**]PPh_4, which displays a relatively high $E_{1/2}$ value of -770 mV. An irreversible oxidation near -400 mV is discernible for most complexes. The feature may correspond to either irreversible oxidation of Fe(III)→Fe(IV) or phenolate-based

oxidation. Based on previous studies of redox-active phenolates bound to metal centers, we favor the latter hypothesis.[51,52, 53]

Table 2.4 Peak potentials E (in V vs $Fc^{+/0}$) of Fe(II) complexes as determined from CV.[a]

	$Fe^{III/II}$			$Fe^{III/II}$			
Compounds	1_{ox}	1_{red}	$E_{1/2}$	2_{ox}	2_{red}	$E_{1/2}$	3_{ox}
[**1**]NEt_4: [Fe(L^1)(Et_4N)]	-1.31	-1.41	-1.36				
[**2**]PPh_4: [Fe(L^2)(PPh_4)]	-0.66	-0.87	-0.77				-0.39
[**6**]$(NEt_4)_2$: [$Fe_2(L^3)_2(NEt_4)_2$]	-1.33	-1.41	-1.37	-0.87	-0.96	-0.91	-0.34
[**7**]$(NEt_4)_2$: [$Fe_2(L^4)_2(NEt_4)_2$]	-1.35	-1.43	-1.39	-0.91	-0.97	-0.94	
[**5**]NEt_4: [Fe(L^5)(Et_4N)]	-1.14	-1.26	-1.20				-0.61

[a] CV on 2 mM solution of complexes in DMF under nitrogen gas. Electrolyte 100 mM $(NBu_4)PF_6$, Pt working electrode and Ag/AgCl reference electrode, $E_{1/2} = (E_{ox} + E_{red})/2$. See Figure 2.8.

In complexes [**6**]$(NEt_4)_2$ and [**7**]$(NEt_4)_2$, the two Fe(II) centers are bridged by two phenolate ligands, forming a central four-membered Fe_2O_2 ring. It appears that this geometry shifts the initial $Fe^{2+/3+}$ redox potential to slightly more negative values,[54] compared with the corresponding monoiron complexes. Given that oxidation of $[\mathbf{7}]^{2-}$ yielded the valence-localized mixed valent complex $[\mathbf{8}]^-$ (*vide supra*), two separate redox potentials are expected for the dinuclear complexes. Indeed, second redox couple (named "couple 2": 2_{ox} and 2_{red}) is evident at higher potential with an $E_{1/2}$-value of -0.937 V (ΔE= 0.45 V). However, complex $[\mathbf{6}]^{2-}$ displays only one clear reversible redox event at -1.37 V, while the peaks of couple 2 are much weaker (Figure 2.8).

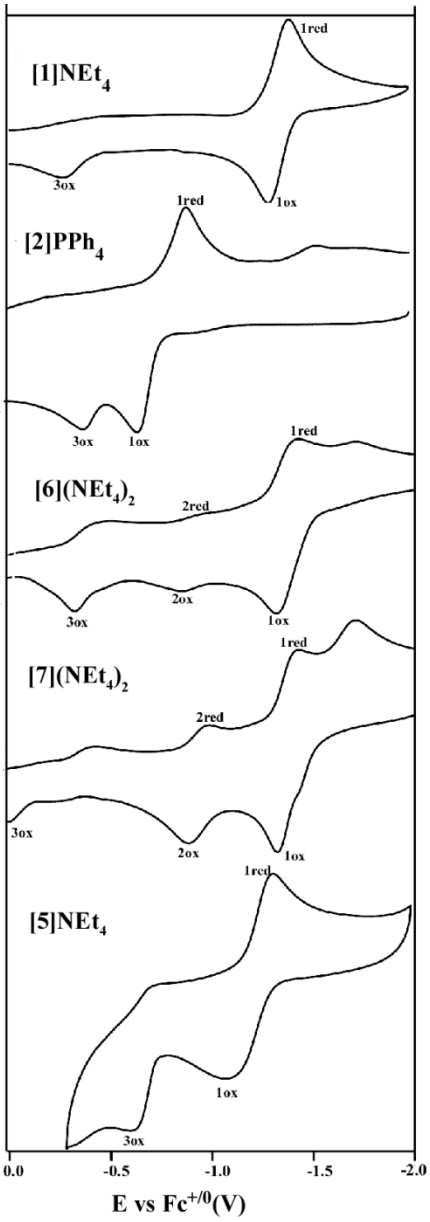

Figure 2.8 Cyclic Voltammograms of ferrous complexes with $\mathbf{H_3L^n}$(n=1-5) in DMF. Scan rate for each of the CV's was 100 mV/s.

In Table 2.5, we have summarized the redox potentials of the $[Fe_4S_4]$ clusters in radical SAM proteins, as well as those measured for relevant model complexes. The redox potential of $[\mathbf{1}]^-$ closely matches the value reported for the ferric complex with same ligand $H_3L^{\mathbf{1}}$ [Fe($\mathbf{L^1}$)(Meim)]. Our Fe(II) complexes are less reducing than Holm's

synthetic [Fe_4S_4] clusters, which feature redox potentials below -1.4 V. The redox potentials of the mononuclear Fe(II) complexes [**1**]NEt_4 and [**5**]NEt_4 are reasonably close (within ~ 150 mV) to potentials measured for the [Fe_4S_4] clusters in radical SAM enzymes. This suggests that these complexes are suitable electrochemical models for the unique Fe center. The reactivity of these complexes with synthetic sulfonium cations is the subject of the following Chapter III.

Table 2.5 Summary of redox potentials E (in V vs $Fc^{+/0}$) of compounds in DMF reported in the literature.

Compound	$E_{1/2}$
[Fe_4S_4] clusters in radical SAM enzymes	-1.10
[Fe(L^1)(1-methylimidazole)][40]	-1.25 in DMF
[Fe{N[CH_2-*o*-C_6H_4S]$_3$}]$^-$ [30]	-0.58 in DMF
[$Fe_4S_4(SPh)_4$]$^{2-/3-}$ from Holm's group[36]	-1.45 in MeCN
[$Fe_4S_4(Et)_4$]$^{2-/3-}$ from Holm's group	-1.75 in DMF

2.2.E Electronic Absorption Spectroscopy Data

Electronic absorption spectra of selected Fe complexes are shown in Figure 2.9. Most complexes display an intense absorption band in the UV region (λ_{max}~300 nm) caused by $\pi \rightarrow \pi^*$ transitions within the phenolate rings. The intense and sharp shoulder at approximately 330 nm in the spectrum of [**1**]NEt_4 is tentatively assigned to either an amine-to-iron charge transfer (CT) band,[51] or charge transfer (CT) from the out-of-plane p_π orbital of the phenolate oxygen to the high-spin Fe(II) center. Finally, the weak and broad bands observed near 400 nm for several complexes likely arise from oxygen→Fe

ligand-to-metal CT transitions. However, exposure of the putative Fe(II) complexes to air results in a dramatic increase in the intensity of ca. 400 nm feature. Thus, it is possible that this band actually arises from partial oxidation of the Fe centers, and should instead be assigned to a phenolate→Fe(III) CT band of the oxidized species. Given the high sensitivity of these complexes to minute amounts of oxygen, it is difficult to obtain accurate molar absorptivity (ε) values.

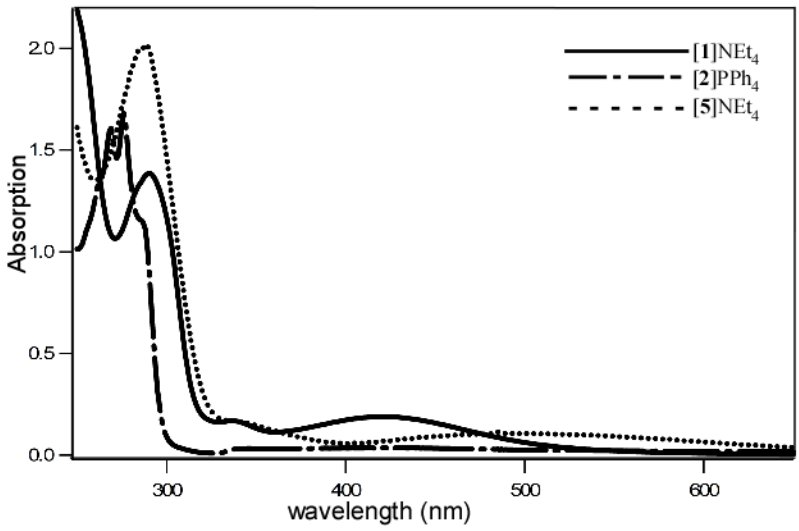

Figure 2.9 Electronic absorption spectra of mononuclear Fe(II) complexes [**1**]NEt_4, [**2**]PPh_4, [**5**]NEt_4 in DMF solutions at room temperature. ([Fe^{2+}] = 0.20 mM).

2.3 Conclusion

A novel series of Fe(II) complexes with three criteria has been prepared supported by amine trisphenolate ligands. These complexes have been structurally characterized by X-ray diffraction and exhibit various geometries, either a mildly distorted trigonal bipyramidal or square pyramidal geometry depending on the ligand employed. And for the asymmetric ligands H_3L^3 and H_3L^4, they display dinuclear feature with each iron

centre linked by a μ-coordinated oxygen from phenolate ring. Paramagnetic ^{1}H NMR spectroscopy confirms high spin d^6 electronic configurations. Electronic absorption spectra in the UV-visible range exhibits strong charge transfer bands from p_π orbital of the phenolate to the d orbitals of high spin Fe(II). Cyclic Voltammetry data confirmed these unsaturated high-spin complexes [**1**]NEt_4 and [**5**]NEt_4 are very promising to model the active site. Further reactivity studies of [**1**]NEt_4 with our synthetic sulfonium salts will be discussed in Chapter 3.

2.4 Experimental Section

2.4.A General

All reagents and solvents were purchased from commercial source and used as received unless otherwise noted. Acetonitrile (MeCN), dichloromethane (DCM), and tetrahydrofuran (THF) were purified and dried using a vacuum atmospheres solvent purification system. All syntheses and handling of air-sensitive materials were carried out under an inert atmosphere using a Vacuum Atmospheres Omni-Lab glovebox equipped with a freezer setting to -25 ^{0}C. NMR spectra were collected at room temperature with a Varian 300 or 400 MHz spectrometer. UV – vis spectra were collected with an Agilent 8453 diode array spectrometer. Electrochemical studies were conducted by using BASi MF - 9092 Potentiostat/Galvanostat in acetonitrile or dimethylformamide (DMF) solutions containing the supporting electrolyte of $(C_4H_9)_4N^{+}\cdot PF^{-}_6$ 100 mM under an inert atmosphere. The reference electrodes used were an Ag/AgCl RE - 5. A platinum wire was used as an auxiliary electrode and platinum

was used as a working electrode for the cyclic Voltammetry (CV). All redox potentials of iron complex are referred to the ferrocenium/ferrocene couple ($Fc^{+/0}$).

2.4.B Syntheses of Amine Trisphenolate Ligands

2-tert-butyl-4-methyl-6-(chloromethyl)phenol

To a solution of 2-tert-butyl-4-methylphenol (16.4 g, 0.1 mol) in methanol (60ml), NaOH (4.40 g, 0.11 mol) was added and stirred at room temperature for 30 min. 36% aqueous Formaldehyde (25 ml, 0.32 mmol) was added to the pink reaction mixture, and stirred for 26 hours. Then the reaction mixture was poured over 300 ml water, acidified with 6M HCl to PH=1-2, and extracted with DCM (3x100 ml). The organic layer was collected, dried over $MgSO_4$, and concentrated to yellow oil. Vacuum distillation of the oil residue gave clear oil as the right product of 2-tert-butyl-4-methyl-6-hydroxymethyphenol at 115 – 125 ^{0}C. Yield: 11.3 g, 58.3 %. ^{1}H NMR ($CDCl_3$, 400 MHz) δ 7.5 (s, 1H, ArH), 6.2 (s, H, ArH), 4.8 (s, 2H, CH_2), 2.2 (s, 3H, CH_3), 1.4 (s, 9H, t-Bu) ^{13}C NMR ($CDCl_3$, 75 MHz) δ 153.1, 137.0, 128.2, 127.6, 126.2, 124.5, 65.4, 34.6, 29.6, 20.6.

To a solution of 2-tert-butyl-4-methyl-6-hydroxymethyphenol (4.24 g, 21.9 mmol) in 40 ml DCM, thionyl chloride (1.84 ml, 25.4 mmol) was added dropwise. Then the reaction mixture was stirred at room temperature for 1 hour and kept under vacuum for several hours to remove solvent, residual thionyl chloride, and hydrogen chloride, to generate the product as pale yellow oil. Yield: 4.13 g, 89.7 %. ^{1}H NMR ($CDCl_3$, 300 MHz) δ 7.3 (s, 1H, ArH), 7.2 (s, H, ArH), 4.7 (s, 2H, CH_2), 2.3 (s, 3H, CH_3), 1.5 (s, 9H,

t-Bu) ^{13}C NMR ($CDCl_3$, 75 MHz) δ 151.8, 137.8, 129.7, 129.2, 128.4, 123.8, 44.7, 34.8, 30.0, 20.9.

2,4-dimethyl-6-(chloromethyl)phenol

Followed the procedure of 2-tert-butyl-4-methyl-6-(chloromethyl)phenol, 2,4-dimethylphenol (2.45g, 20.1mmol) in methanol (60ml), NaOH (0.894 g, 22.4mmol) and 36% aqueous Formaldehyde (6.00 ml, 76.8mmol) gave white solid as the right product at the vacuum distillation of 110 – 120 ^0C. Yield: 2.00g, 57.1%. ^1H NMR ($CDCl_3$, 400 MHz) δ 6.9 (s, 1H, ArH), 6.6 (s, H, ArH), 4.7 (s, 2H, CH_2), 2.2 (d, 6H, CH_3). ^{13}C NMR ($CDCl_3$, 75 MHz) δ 151.8, 131.5, 129.0, 126.2, 125.2, 124.2, 64.6, 20.5, 15.7.

And followed same procedure of 2-tert-butyl-4-methyl-6-(chloromethyl)phenol, 2,4-dimethyl-6-(chloromethyl)phenol was made as white powder. Yield: 4.13 g, 89.7 %. ^1H NMR ($CDCl_3$, 400 MHz) δ 6.9 (s, 1H, ArH), 6.9 (s, H, ArH), 4.6 (s, 2H, CH_2), 2.2 (s, 3H, CH_3), 2.1 (s, 3H, CH_3) ^{13}C NMR ($CDCl_3$, 100 MHz) δ 150.4, 132.4, 129.8, 128.4, 124.5, 123.0, 43.1, 20.3, 15.7.

o-amino-4,6-di-tert-butylphenol

To a solution of 3,5-di-tert-butyl-o-benzoquinone (1.59 g, 7.26 mmol) in 45ml methanol, 20ml NH_4OH was added and stirred at room temperature for 15 min. And then adding sodium borohydride (0.374 g, 9.87 mmol) and stirring another 15 min and filtering, green powder was collected and washed with MeOH:NH_4OH (3:1) to give the right product as nice green powder. Yield: 0.734 g, 45.7 %. ^1H NMR ($CDCl_3$, 400 MHz) δ 6.9 (s, 1H, ArH), 6.8 (s, 1H, ArH), 3.2 (s, 2H, NH_2), 1.4 (s, 9H, t-Bu), 1.3 (s, 9H, t-Bu).

^{13}C NMR ($CDCl_3$, 100 MHz) δ 144.2, 142.7, 135.9, 132.6, 132.6, 117.25, 115.9, 34.9, 31.8, 30.0。

H_3L^1:

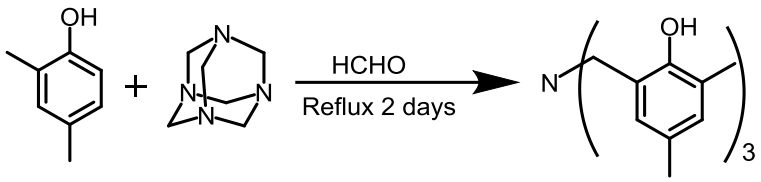

H_3L^1

2,4-dimethylphenol (5.10g, 41.7 mmol), hexamethylenetetramine (0.470 g, 3.35 mmol), and 35 % aqueous formaldehyde solution (1.21 g, 14.2 mmol) was refluxed at 125 ^{0}C for 2 days, after which the yellow mixture was quenched with chloroform, washed with water (3x100 ml). The organic layer was collected, dried over $MgSO_4$ and concentrated to slightly yellow oil. Recrystallization of the oil residue from methanol: Ether (1:1) 15ml overnight in freezer of -20 ^{0}C gave white solid as product, washed with cold methanol 4 times and dried under vacuum. Yield: 2.54 g, 43.2 %. ^{1}H NMR ($CDCl_3$, 400 MHz) δ 6.84 (s, 3H, ArH), 6.7 (s, 3H, ArH), 3.6 (s, 6H, CH_2), 2.2 (s, 18H, CH_3), ^{13}C NMR ($CDCl_3$, 75 MHz) δ 151.1, 131.2, 129.1, 128.8, 124.5, 121.8, 56.4, 20.4, 15.9.

H_3L^2:

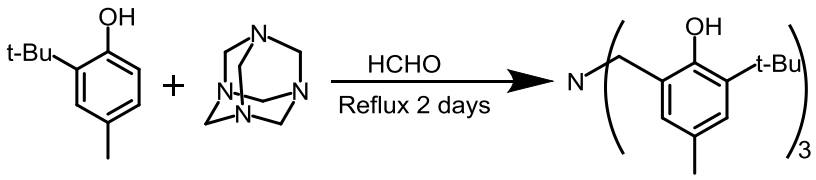

H_3L^2

2-tert-butyl-4-methylphenol (6.56 g, 40.0 mmol), hexamethyltetramine (0.47 g, 3.30 mmol), and 35 % aqueous formaldehyde solution (1.21 g, 14.2 mmol) was refluxed at 125 ^{0}C for 3 days, after which the yellow mixture was worked up by generally following the procedure 4.2.1 and gave white powder as the product. Yield: 2.5g, 45 %. ^{1}H NMR ($CDCl_3$, 400 MHz) δ 7.0 (s, 3H, ArH), 6.6 (s, 3H, ArH), 4.0 (s, 6H, CH_2), 2.2 (s, 9H, CH_3), 1.3 (s, 27H, t-Bu). ^{13}C NMR ($CDCl_3$, 75 MHz) δ 154.4, 136.8, 129.8, 127.4, 126.1, 121.3, 55.3, 34.9, 29.8, 21.1.

H_3L^3:

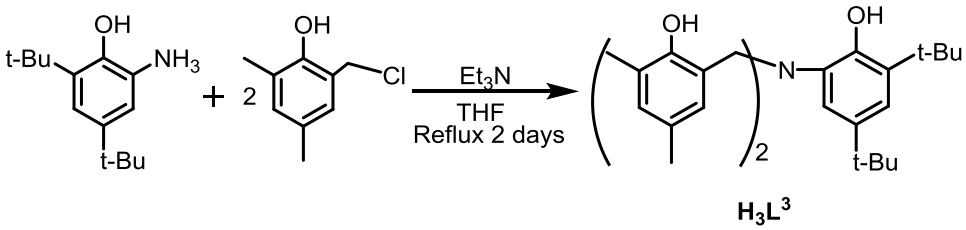

H_3L^3

To a solution of 2-amino-4,6-di-tert-butylphenol (0.394 g, 1.78 mmol) and 2,4-dimethyl-6-(chloromethyl)phenol (1.79 g, 3.56 mmol) in THF (40 ml), triethylamine (0.50 ml, 3.6 mmol) was added slowly. The mixture was refluxed at 80 ^{0}C for 2 days, after which the solvent was removed by rotator evaporation to give dark yellow solid. The yellow residue was redissolved in 30ml DCM, washed 3 times with water, dried over $MgSO_4$ and concentrated to light yellow powder as product. Yield: 0.703 g, 80.7 %. ^{1}H NMR ($CDCl_3$, 400 MHz) δ 7.1 (s, 1H, ArH), 7.0 (s, 1H, ArH), 6.8 (s, 2H, ArH), 6.8 (s, 2H, ArH), 4.2 (s, 4H, 2*CH_2), 2.2 (s, 6H, 2*CH_3), 2.1 (s, 6H, 2* CH_3), 1.4 (s, 9H, t-Bu), 1.3 (s, 9H, t-Bu) ^{13}C NMR ($CDCl_3$, 100 MHz) δ 151.0, 148.5, 140.1, 135.3, 134.4, 131.1, 129.5, 128.9, 123.8, 121.9, 119.9, 116.2, 55.5, 35.0, 34.4, 31.5, 29.5, 20.3, 15.6.

H_3L^4:

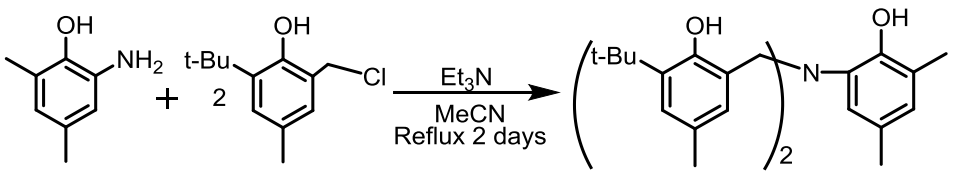

H_3L^4

To a solution of 6-amino-2,4-dimethylphenol (1.38 g, 10.0 mmol) and 2-tert-butyl-4-methyl-6-(chloromethy)phenol (4.23 g, 20.1 mmol) in MeCN (30 ml), triethylamine (3.0 ml, 21.5 mmol) was added slowly. The mixture was refluxed at 90 ^{0}C for 2 day and was concentrated to orange powder. Purification was achieved by column chromatography using 3% ethyl acetate: 97 % Hexane. The first component was collected and concentrated to light yellow powder as the right product. Yield: 1.3 g, 25 %. ^{1}H NMR ($CDCl_3$, 300 MHz) δ 6.9 (s, 2H, ArH), 6.9 (s, 1H, ArH), 6.7 (s, 2H, ArH), 6.6 (s, 1H, ArH), 4.0 (s, 4H, 2*CH_2), 2.2 (s, 9H, CH_3), 2.1 (s, 3H, CH_3), 1.3 (s, 18H, t-Bu). ^{13}C NMR ($CDCl_3$, 75 MHz) δ 152.5, 147.6, 136.3, 135.2, 129.7, 129.2, 128.5, 127.5, 124.4, 122.8, 120.1, 116.1, 56.4, 34.5, 29.9, 21.1, 20.9, 16.1.

H_3L^5:

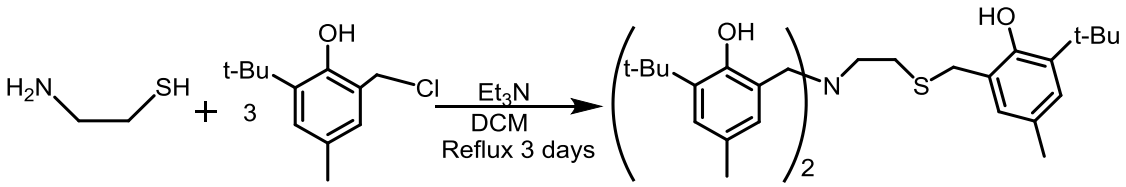

H_3L^5

To a solution of 2 (2.12 g, 10.0 mmol) and 2-mercaptoethylamine·HCl (0.374 g, 3.29 mmol) in DCM (40 ml), triethylamine (2.07 ml, 14.8 mmol) was added slowly. The mixture was refluxed at 55 ^{0}C for 3 days. The reaction solution was quenched by DCM,

washed 3 times with water, dried over $MgSO_4$ and concentrated to yellow powder. Recrystallization of the residue in MeCN at -20 ^{0}C overnight gave white crystalline precipitate as the product. Yield: 1.08 g, 54.3 %. ^{1}H NMR ($CDCl_3$, 400 MHz) δ 7.0 (s, 2H, ArH), 7.0 (s, 1H, ArH), 6.7 (s, 2H, ArH), 6.6 (s, 1H, ArH), 3.5 (s, 6H, 3*CH_2), 2.5 (dd, 4H, 2*CH_2), 2.2 (s, 6H, CH_3), 2.1 (s, 3H, CH_3), 1.4 (s, 18H, t-Bu), 1.3 (s, 3H, t-Bu). ^{13}C NMR ($CDCl_3$, 75 MHz) δ 154.3, 147.2, 139.8, 137.6, 132.2, 130.5, 129.4, 128.9, 128.5, 127.4, 124.8, 122.6, 56.8, 55.8, 34.7, 32.4, 30.4, 29.7, 21.1.

2.4.C Synthesis of Metal Complexes: Ferrous Complexes: Mononuclear and dinuclear Fe complexes

The preparation of the complexes follows this general procedure: **H_3L^n** (1.0 mmol) was dissolved in 20.0 ml anhydrous methanol and t with sodium methoxide (3.0 mmol) in glovebox of nitrogen pressure. To the resulting solution were added $FeCl_3$/$FeCl_2$ (1.0 mmol) (For the Fe(II) complexes, one equivalent NEt_4Cl or PPh_4Br was added to provide a suitable countercation for crystallographic studies. After stirring the mixture at room temperature overnight and removal of the solvent under vacuum, the yellow-colored solid was redissolved in MeCN, filtered through celite and dried under vacuum. X-ray quality crystals were obtained using different solvents.

[1]NEt_4: [Fe(L^1)(Et_4N)]:

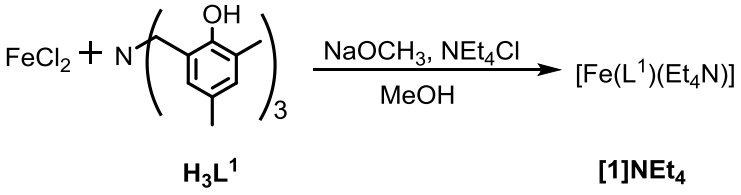

According to the general procedure, $FeCl_2$ (126 mg, 1.00 mmol) was treated with H_3L^1 (419 mg, 1.0 mmol), $NaOCH_3$ (162 mg, 3.00 mmol) and $Et_4NCl{\cdot}H_2O$ (183 mg, 1.00 mmol) to give [**1**]NEt_4 as orange powder. X-ray quality crystals were afforded by layering Hexane into a high concentrate isopropyl alcohol solution as yellow crystal. Yield: 203 mg, 33.8%. (Elemental Analysis: %C: 68.33, %H: 7.89; %N: 4.04.)

[2]PPh_4: [Fe(L^2)(PPh_4)]:

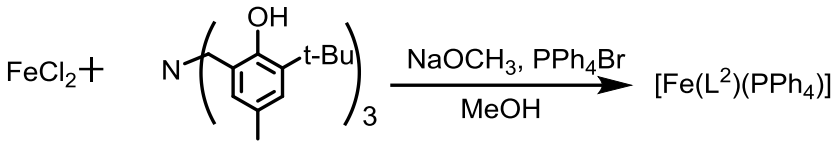

H_3L^2 **[2]PPh_4**

According to the general procedure, $FeCl_2$ (126 mg, 1.00mmol) was treated with H_3L^2 (545 mg, 1.00 mmol), $NaOCH_3$ (162 mg, 3.00 mmol) and tetraphenylphosphonium bromide (0.419 mg, 1.00 mmol) to give [Fe(L^2)(Ph_4P)] as yellow powder. The layering of Hexane into a high concentrated DCM solution gave X-ray quality crystals as dark yellow. Yield: 549 mg, 75.4 %.

[4]: [Fe(L^2)]*:*

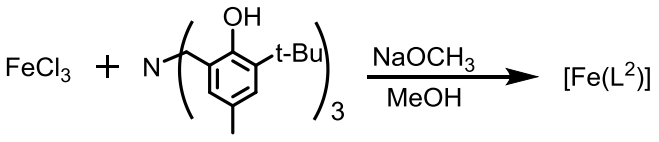

H_3L^2 **[4]**

According to the general procedure, $FeCl_3$ (162 mg, 1.00 mmol) was treated with H_3L^2 (545 mg, 1.00 mmol) and $NaOCH_3$ (162 mg, 3.00 mmol) to give **4** as black powder. X-ray quality crystals were grown in pure DMF under -30 ^{0}C. Yield: 170 mg, 28.4%.

[5]NEt$_4$: [Fe(L^5)(Et$_4$N)]:

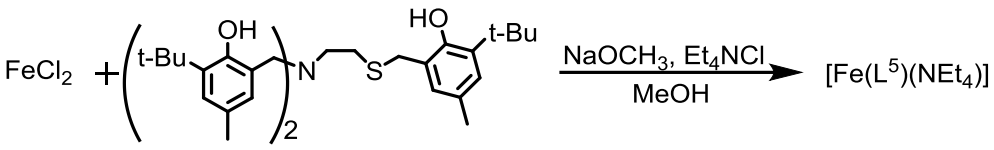

H_3L^5 **[5]NEt_4**

According to the general procedure, $FeCl_2$ (126 mg, 1.00 mmol) was treated with H_3L^5 (605 mg, 1.00 mmol), $NaOCH_3$ (162 mg, 3.00 mmol) and $Et_4NCl{\cdot}H_2O$ (183 mg, 1.00 mmol) to give [**5**]NEt_4 as dark brown powder. X-ray quality crystals were grown by vapor diffusion of Hexane into DMF. Yield: 486 mg, 61.6 %.

[6](NEt$_4$)$_2$: [Fe$_2$(L^3)$_2$(NEt$_4$)$_2$]:

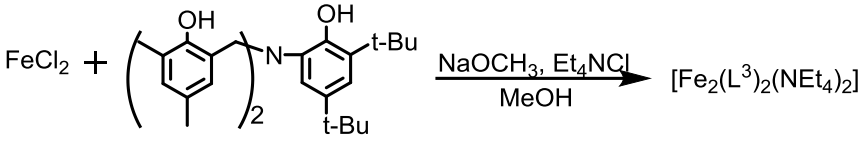

H_3L^3 **[6]$(NEt_4)_2$**

According to the general procedure, $FeCl_2$ (126 mg, 1.00 mmol) was treated with H_3L^3(490 mg, 1.00 mmol), $NaOCH_3$ (162 mg, 3.00 mmol) and $Et_4NCl{\cdot}H_2O$ (183 mg, 1.00 mmol) to give [**6**]$(NEt_4)_2$ as dark brown powder. X-ray quality crystals were grown by vapor diffusion of Hexane into isopropyl alcohol. Yield: 277 mg, 82.3 %.

[7](NEt$_4$)$_2$: [Fe$_2$(L^4)$_2$(NEt$_4$)$_2$]:

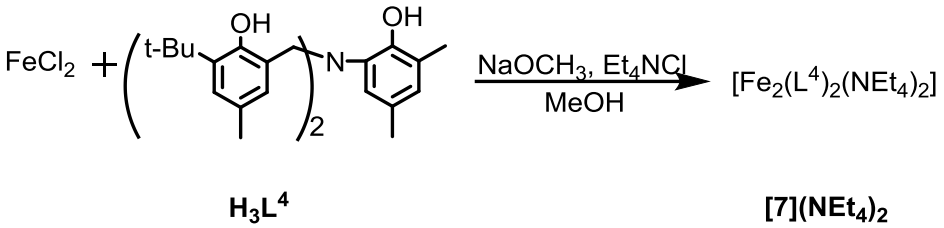

H_3L^4 **[7](NEt$_4$)$_2$**

According to the general procedure, $FeCl_2$ (126 mg, 1.00 mmol) was treated with H_3L^4 (489 mg, 1.00 mmol), $NaOCH_3$ (162 mg, 3.00 mmol) and $Et_4NCl{\cdot}H_2O$ (183 mg, 1.00 mmol) to give dimeric [**7**](NEt$_4$)$_2$ as greenish brown powder. X-ray quality crystals were grown by vapor diffusion of Hexane into isopropyl alcohol. Yield: 286 mg, 85.1 %.

[8]NEt$_4$: [Fe$_2$(L^4)$_2$(NEt$_4$)]:

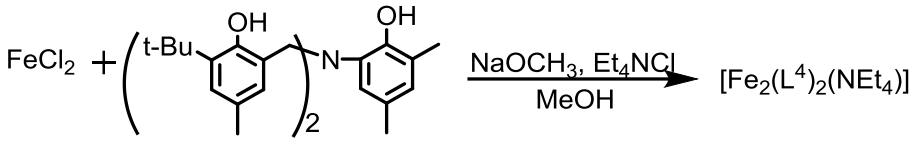

H_3L^4 **[8]NEt$_4$**

Complex [**8**]NEt$_4$ was synthesized and crystallized following the procedure similar to [**7**](NEt$_4$)$_2$, a vapor diffusion of Et_2O into MeCN yielded dark brown crystal. X-ray analysis confirmed mix-valent product [**8**]NEt$_4$.

9: [Fe$_2$(L^1)$_2$]:

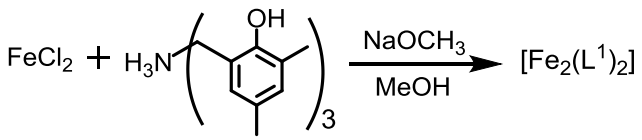

H_3L^1 **9**

According to the general procedure, $FeCl_3$ (162 mg, 1.00 mmol) was treated with $H_3L^{\mathbf{1}}$ (419 mg, 1.00 mmol) and $NaOCH_3$ (162 mg, 3.00 mmol) to give **9** as black powder. X-ray quality crystals were grown by layering pentane on a concentrated DCM solution as brown crystal. Yield: 330 mg, 69.8%.

Table 2.6 Summary of X-ray crystallographic data collection and structure refinement.

	[**1**]NEt_4	[**2**]PPh_4	[**3**]PPh_4	**4**
Empirical formula	$C_{41}H_{64.5}FeN_2O_5$	$C_{60.6365}H_{69.9095}Cl_{0.68175}FeNO_{3.31825}P$	$C_{60}H_{68}NO_3PClFe$	$C_{39}H_{55}FeN_2O_4$
Formula weight	721.30	976.80	973.42	671.70
Temperature/K	100.00(10)	99.95(10)	100.00(10)	100.00(10)
Crystal system	monoclinic	orthorhombic	orthorhombic	monoclinic
Space group	$P2_1/c$	$Pna2_1$	$Pna2_1$	$P2_1/m$
a/Å	29.9190(10)	18.2993(9)	17.9643(7)	9.8922(5)
b/Å	11.8500(3)	13.2235(4)	13.2670(5)	17.5425(9)
c/Å	22.9755(11)	21.9243(12)	21.9885(7)	10.7770(6)
α/°	90.00	90.00	90.00	90.00
β/°	93.047(3)	90.00	90.00	98.829(5)
γ/°	90.00	90.00	90.00	90.00
Volume/$Å^3$	8134.2(5)	5305.3(4)	5240.6(3)	1848.01(17)
Z	8	4	4	2
$\rho_{calc}mg/mm^3$	1.178	1.223	1.234	1.207
m/mm^{-1}	3.304	3.228	0.414	3.583
2Θ range for data collection	7.7 to 149.56°	7.8 to 148.1°	6.74 to 59.08°	8.3 to 147.88°
Reflections collected	43013	29661	27353	10917
Independent reflections	16058[R(int) = 0.0575]	8762[R(int) = 0.0631]	12036[R(int) = 0.0369]	3784[R(int) = 0.0385]
Data/restraints/parameters	16058/270/895	8762/1/628	12036/1/616	3784/176/288
Goodness-of-fit on F^2	1.055	1.045	1.035	1.055
Final R indexes [I>=2σ (I)][a]	R_1 = 0.0803, wR_2 = 0.2163	R_1 = 0.0700, wR_2 = 0.1695	R_1 = 0.0407, wR_2 = 0.0897	R_1 = 0.0469, wR_2 = 0.1103
Final R indexes [all data] [a]	R_1 = 0.1030, wR_2 = 0.2405	R_1 = 0.0825, wR_2 = 0.1820	R_1 = 0.0509, wR_2 = 0.0972	R_1 = 0.0570, wR_2 = 0.1169

$R1 = \sum ||F_o| - |F_c|| / \sum |F_o|$; $wR2 = [\sum w(F_o^2 - F_c^2)^2 / \sum w(F_o^2)^2]^{1/2}$

Table 2.7 Summary of X-ray crystallographic data collection and structure refinement.

	[**5**]NEt_4	[**6**]$(NEt_4)_2$	[**7**]$(NEt_4)_2$	[**8**]NEt_4
Empirical formula	$C_{48}H_{80}FeN_2O_5S$	$C_{84}H_{128}Fe_2N_6O_7$	$C_{86}H_{133}Fe_2N_5O_7$	$C_{80.4171}H_{112.62565}Fe_2N_{7.20855}O_6$
Formula weight	853.05	1445.62	1460.67	1388.03
Temperature/K	373.10(10)	100.00(10)	99.95(10)	100.00(10)
Crystal system	monoclinic	triclinic	monoclinic	monoclinic
Space group	$P2_1/c$	P-1	Cc	C2/c
a/Å	13.5433(6)	18.9455(3)	14.4633(2)	24.4814(2)
b/Å	13.3718(5)	20.8384(4)	25.0194(3)	14.70453(15)
c/Å	27.2260(10)	23.5345(5)	24.2285(4)	43.8725(4)
α/°	90.00	71.3257(17)	90.00	90.00
β/°	93.019(4)	70.7061(16)	105.4906(16)	94.0231(8)
γ/°	90.00	74.7610(15)	90.00	90.00
Volume/$Å^3$	4923.7(3)	8178.6(3)	8448.9(2)	15754.7(3)
Z	4	4	4	8
$\rho_{calc}mg/mm^3$	1.151	1.174	1.148	1.170
m/mm^{-1}	3.185	0.409	3.163	3.370
2Θ range for data collection	7.36 to 147.44°	6.68 to 59.12°	7.06 to 147.62°	7.02 to 145.7°
Reflections collected	26116	146419	71503	65591
Independent reflections	9691[R(int) = 0.0512]	40890[R(int) = 0.0415]	15325[R(int) = 0.0906]	15493[R(int) = 0.0375]
Data/restraints/parameters	9691/0/534	40890/24/1898	15325/2/932	15493/102/993
Goodness-of-fit on F^2	3.225	1.062	1.014	1.019
Final R indexes [I>=2σ (I)][a]	R_1 = 0.1753, wR_2 = 0.4648	R_1 = 0.0426, wR_2 = 0.0948	R_1 = 0.0381, wR_2 = 0.0951	R_1 = 0.0424, wR_2 = 0.1113
Final R indexes [all data] [a]	R_1 = 0.1848, wR_2 = 0.4679	R_1 = 0.0669, wR_2 = 0.1075	R_1 = 0.0425, wR_2 = 0.0982	R_1 = 0.0477, wR_2 = 0.1163

$R1 = \sum ||F_o| - |F_c|| / \sum |F_o|$; $wR2 = [\sum w(F_o^2 - F_c^2)^2 / \sum w(F_o^2)^2]^{1/2}$

Table 2.8 Summary of X-ray crystallographic data collection and structure refinement.

	9
Empirical formula	$C_{56}H_{64}Cl_4Fe_2N_2O_6$
Formula weight	1114.59
Temperature/K	100.00(10)
Crystal system	monoclinic
Space group	C2/c
a/Å	31.1185(18)
b/Å	10.7719(5)
c/Å	17.0611(10)
α/°	90.00
β/°	114.153(7)
γ/°	90.00
Volume/Å^3	5218.3(5)
Z	4
ρ_{calc}mg/mm^3	1.419
m/mm^{-1}	6.761
2Θ range for data collection	8.78 to 147.64°
Reflections collected	10470
Independent reflections	10474[R(int) = 0.0000]
Data/restraints/parameters	10474/0/351
Goodness-of-fit on F^2	1.110
Final R indexes [I>=2σ (I)] [a]	R_1 = 0.0565, wR_2 = 0.1392
Final R indexes [all data] [a]	R_1 = 0.0770, wR_2 = 0.1553

$R1 = \sum ||F_o| - |F_c|| / \sum |F_o|$; $wR2 = [\sum w(F_o^2 - F_c^2)^2 / \sum w(F_o^2)^2]^{1/2}$

Chapter III

Reactivity Studies of Iron (II) Complex with Sulfonium Salts

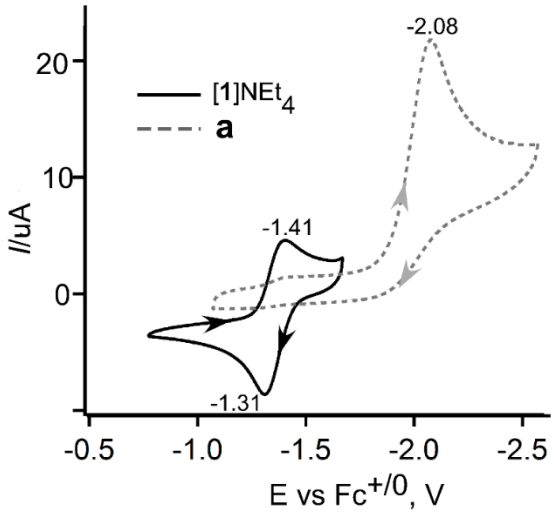

Figure 3.1 Cyclic voltammograms of [**1**]NEt_4 (Solid) and sulfonium salt **a** (Dashed) in DMF with 100 mM $(NBu_4)PF_6$ as the supporting electrolyte and a scan rate of 100 mV/s.

Abstract: To determine whether the synthetic models in described in the previous chapter are capable of reductively cleaving S-C bonds to generate radical species, we prepared sulfonium salts that contain metal-binding moieties, such as a pyridyl group, that position the reactive sulfonium group close to the Fe(II) center. By monitoring changes in UV-visible absorption features as a function of time, we have measured reaction rates for the sulfonium cations: *S*-(phenyl) tetramethylenesulfonium and *S*-(2-pyridylmethyl) tetramethylenesulfonium, to evaluate the effects of Fe···S distances on the rate of electron transfer. GC-MS and ^{1}H NMR spectroscopy were used to characterize and quantify the resulting products. Finally, density functional theory (DFT) calculations have been performed to further elucidate the significant interactions within this synthetic modeling system.

3.1 Introduction

The radical SAM superfamily of enzymes plays an important role in many processes, such as the metabolism of amino acids, biosynthesis of vitamins and gene expression. As discussed in chapter 1, the $[Fe_4S_4]$ cluster in radical SAM-dependent enzymes has only three conserved cysteine ligands with one unique Fe center, which is able to bind the carboxyl and amino groups of SAM.[4] Inner-sphere electron transfer from the reduced $[Fe_4S_4]^+$ cluster to the sulfonium group of SAM occurs in accordance with cleavage of the S-C5' bond of *S*-adenosyl-methionine to give the Ado· radical, which further participates in the initiation of various biological reactions.[55] After the reductive cleavage of the S-C bond, the unique Fe center may coordinate to the S-atom of the methionine product. Although the mechanism by which SAM is reductively cleaved in its reversible reaction with the $[Fe_4S_4]$ cluster has been the subject of various spectroscopic and computational studies, very few studies with synthetic models have been conducted.

As discussed in chapter 1, due to the difficulties in the preparation of adequate synthetic $[Fe_4S_4]$ clusters, modeling studies of radical SAM enzymes have been hindered. However, in this project, we seek to generate high-spin mononuclear Fe(II) complexes with low reduction potentials that can react with SAM-like substrates, thus generating carbon-based radicals. We already presented the syntheses and characterizations of Fe(II) complexes in chapter 2 that fulfill three criteria: i) high spin Fe centers, ii) low redox potentials (for complex [**1**]NEt_4, $E_{1/2}$ = -910 mV vs SCE), and iii) unsaturated coordination environments. By analyzing the reactivity of these complexes with various sulfonium salts (Figure 3.1), we intend to formulate structure-reactivity correlations that are transferrable to the SAM-dependent enzymes themselves.

In spite of difficulties in collecting accurate kinetic data and reaction yields due to the highly air-sensitive nature of these complexes, we were able to perform product analyses and quantifications, and obtain kinetics data with different sulfonium salts at various temperatures. However further conclusions will require more extensive kinetics data.

3.2 Discussion and Results

To determine whether our synthetic models are capable of reductively cleaving S-C bonds to generate radical species, we have generated the sulfonium salts shown in Figure 3.2.

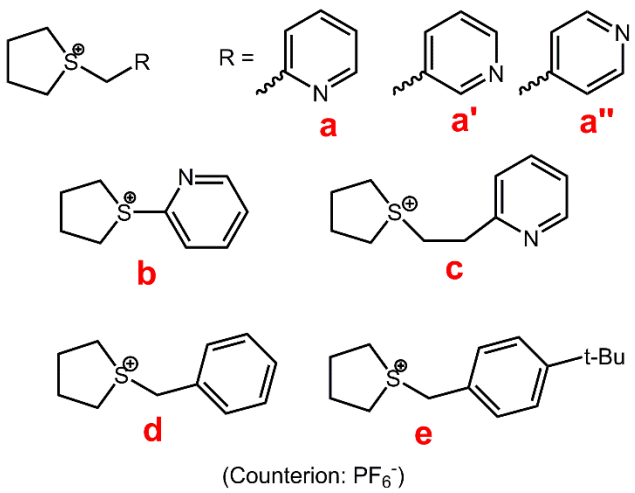

Figure 3.2 Structure of sulfonium cations (**a-e**), and the counterion of all salts are PF_6^-.

Each sulfonium salt consists of a tetrahydrothiophene unit and a special fragment consisting of a benzyl or metal-binding pyridyl group. The benzyl compound was

prepared as a control to assess the impact of metal coordination on reactivity. The PF_6^- anion was typically used as the counteranion. The **a-a''** series and **d** salt were easily prepared by S_N2 reaction of tetrahydrothiophene with the appropriate organobromine compound, followed by addition of NH_4PF_6. Sulfonium salt **b** was synthesized by reaction of 2-mercaptopyridine and 1,4-dibromobutane in Et_2O with NEt_3 serving as the base, followed by counterion exchange with NH_4PF_6 in acetone.[56] Compound **c** was synthesized in two steps by using excess thionyl chloride and $AgPF_6$. Firstly, the precursor 2-(2-chloroethyl)pyridine was synthesized by a reaction of 2-(2-hydroxylethyl) pyridine and $SOCl_2$. Then 2-(2-chloroethyl)pyridine, tetrahydrothiophene and $AgPF_6$ were used to synthesize salt **c**. The sulfonium salts **a-c** feature a pyridyl donor that can position the sulfonium group closer to the Fe(II) center after binding of the pyridyl moiety, yet the expected distance between the Fe and atom S would be relatively different. For **d** and **e**, there is no strong electron donor that can directly bind to metal center.

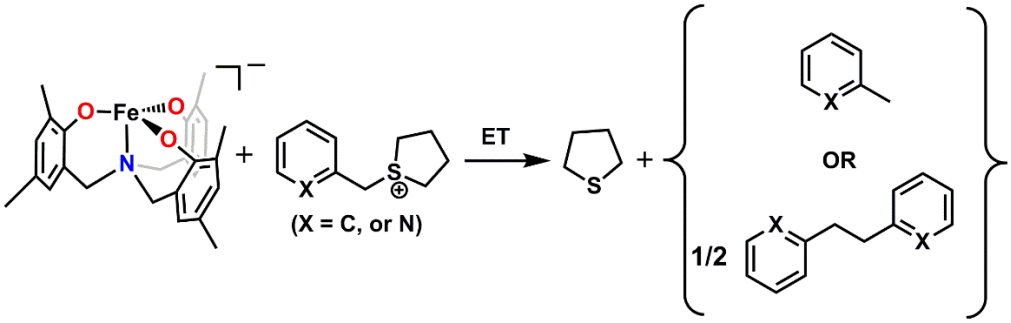

Scheme 3.1 Proposed products from the reaction of [**1**]NEt_4 and different sulfonium salts (**a** or **d**) via electron transfer and bond-cleavage.

In order to investigate the reactivity of Fe(II) complexes, we selected [**1**]NEt_4 (see Chapter II) and sulfonium **a** (pyridyl version) and **d** (benzyl version) for detailed product analysis and kinetic studies. Previous studies indicated the reaction can go through one or two electron reductions via different pathways to generate the three possible products shown in Scheme 3.1.[38,31] In the following sections, product analyses will provide more detailed information about the electron transfer and the S-C bond cleavage processes. And by collecting the kinetic data for the reaction of [**1**]NEt_4 with different sulfonium salts, we can evaluate the effect of the metal-binding group, the strength of the S-C bonds, and the distance of the S-atom from Fe(II) ion on the rate of electron transfer.

3.2.A Products Analysis and Quantification

3.2.A.1 Reaction of [1]NEt_4 with S-benzyl Tetramethylenesulfonium Salt (d) in THF

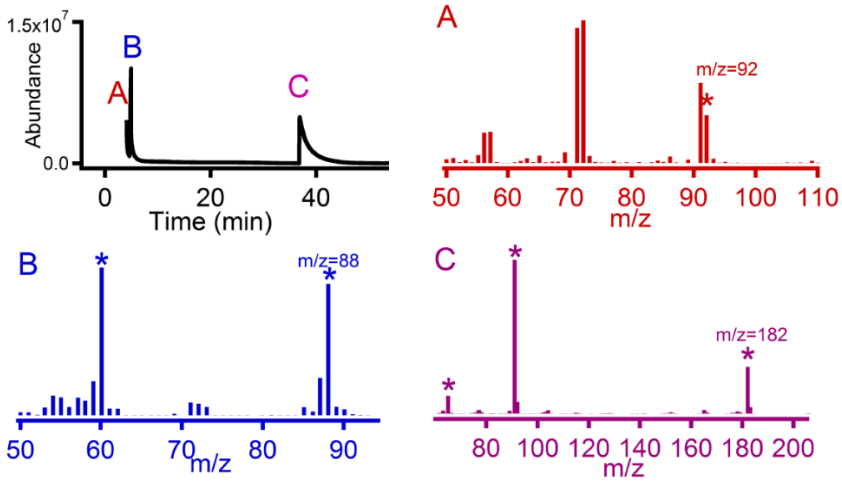

Figure 3.3 GC spectra derived from [**1**]NEt_4 reacting with **d**. And MS spectra corresponding to each peak on GC shows as following: (**A**) Mixture of toluene and THF solvent, (**B**) tetrahydrothiophene and (**C**) bibenzyl. Peaks marked with an asterisk (*) arise from fragmentation of the dominant product.

In the products analyses experiments, [**1**]NEt_4 (26.2 mg, 0.044 mmol) was dissolved in THF 2ml, and *S*-benzyl tetramethylenesulfonium PF_6^- (**d**) **(**14.1 mg, 0.044 mmol) was added. The reaction suspension was allowed to stir at room temperature for 18 hours. The reaction solution was passed through column packed with aluminum oxide as the stationary phase and hexane as mobile phase to remove Fe-containing salts. The organic components were collected and analyzed by GC-MS. After removal of solvent, the white crystalline residue was quantified by using GC-MS and GC-FID, using naphthalene as an internal calibration standard. In order to quantify the bibenzyl product, a response factor (R) relative to naphthalene was measured and a value of 0.8711 was obtained.

As shown in Figure 3.3, GC data derived from the reaction of [**1**]NEt_4 with **d** shows three peaks (marked by **A**, **B**, and **C**). The corresponding MS spectra are also displayed individually in Figure 3.3. According to the MS data, the first peak (**A**) is a mixture of toluene (derived from) and THF solvent. The GC peak B exhibits a clear peak at m/z = 88 in the MS attributable to tetrahydrothiophene (Figure 3.3.**B**), indicating the apparent cleavage of S-C bond in **d**. The last peak C at m/z = 182corresponds to bibenzyl (Figure 3.3.**C**). The peaks in the ^1H NMR spectrum also confirm the presence of these three products (See Experimental Section 3.4.**C**).

In terms of yield in the reaction of [**1**]NEt_4 reacting with **d**, if all of **d** transformed to bibenzyl via an electron-transfer pathway, then 1 equivalent of [**1**]NEt_4 should generate 1 equivalent of tetrahydrothiophene and ½ equiv. of bibenzyl. We ran three trials with [**1**]NEt_4 and **d** in molar ratios of approximately 1:1, 1:5 and 4:1. Once all of three trials reacted completely, GC-FID was used to quantify the products with

naphthalene as the internal standard. The moles information of starting materials and the bibenzyl product are summarized in Table 3.1. The highest yield of bibenzyl we obtained is 63% from trial 3 in which **d** is the limiting reagent.

Table 3.1 Bibenzyl product quantifications. Each trial represents a different molar ratio. And in each different molar ratio, we did several times and took the average.

Trial	Mole Ratio of [**1**]NEt_4 and **d**	Moles of [**1**]NEt_4 (mmol)	Moles of **d** (mmol)	Moles of bibenzyl (mmol)	Theoretical moles of bibenzyl (mmol)	Yield of bibenzyl (%)	**Average**
1	1:1	0.0440	0.0440	0.0102	0.0220	46.36	**40.56 +/- 5.8**
		0.0468	0.0466	0.0092	0.0233	39.48	
		0.0742	0.0741	0.0133	0.0371	35.85	
2	1:5	0.0440	0.0880	0.0103	0.0220	46.82	**46.17 +/- 0.980**
		0.0566	0.2831	0.0126	0.0283	44.54	
		0.0385	0.1935	0.0091	0.0193	47.15	
3	4:1	0.1369	0.0342	0.0107	0.0171	62.57	**62.57**

Owing to the air-sensitivity of the [**1**]NEt_4 complex, it is reasonable that the yield for trial 3 is larger than the other two in which [**1**]NEt_4 is the limiting reagent. Since all reactions were carried out overnight in the glovebox, the amount of oxygen present in the glovebox may be competent to oxidize [**1**]NEt_4 at room temperature. In addition, if there is any impurity in [**1**]NEt_4, the yield will be decreased. The last possible reason for the low yield may be sublimation of the bibenzyl product during work-up of the reaction. ^1H NMR spectroscopy could be another potential technique to quantify products.

The product analysis and quantification above strongly support our prediction that [**1**]NEt_4 is capable of electron-transfer to the sulfonium substrate, and facilitating cleavage of the S-C bond. Based on the mechanisms proposed for SAM-dependent enzymes and Holm's synthetic systems[4,36], the products derived from the reaction could

arise from two possible mechanistic pathways, as shown Scheme 3.2. Both pathways share the same initial step: one electron transfer from [**1**]NEt_4 to **d**, prompting the generation of tetrahydrothiophene and the carbon-based benzyl radical (Step 1). In the first pathway, the two benzyl radicals couple to give the product bibenzyl instantly (Step 2). Another possibility involves transferring of a H-atom to the radical to generate toluene (Step 3).

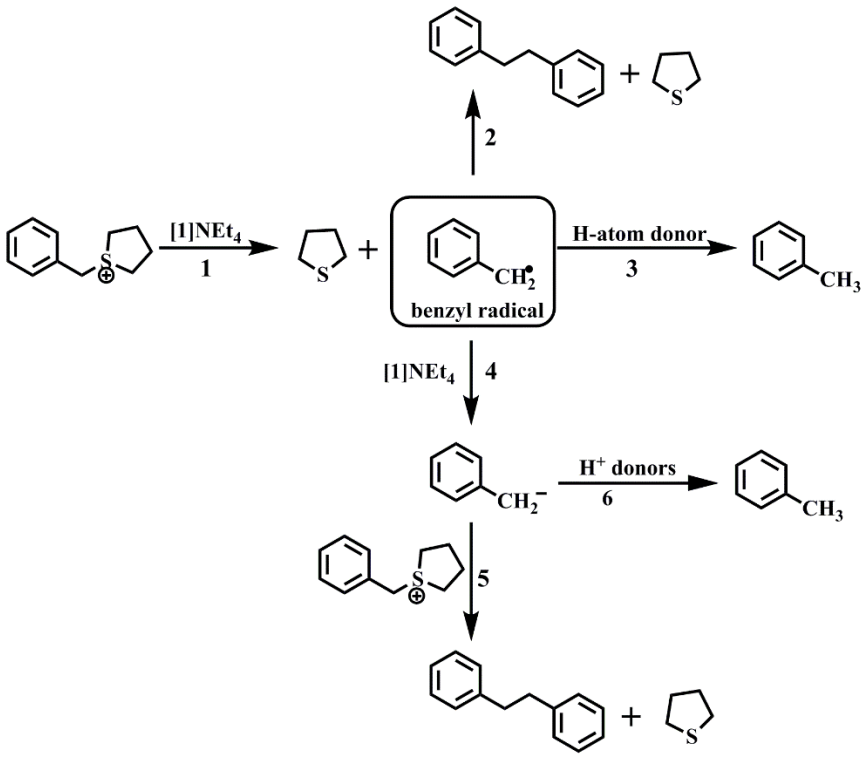

Scheme 3.2 Proposed pathways for the products upon electron transfer and S-C bond cleavage in the reaction of [**1**]NEt_4 with *S*-benzyl tetramethylenesulfonium salt **d**.

The second possible mechanism requires two-electron reduction of each sulfonium cation by two equivalents of [**1**]$^-$. After the first electron transfer and S-C bond cleavage, the transient carbon-based radical would very likely to be reduced to a

carbanion by a second electron originating from [**1**]NEt_4.(Step 4). Subsequently this carbanion substrate can participate in an S_N2-type reaction with a second equivalent of **d** to yield bibenzyl (Step 5). Alternatively, it could abstract a proton from solvent or **d**, thus accounting for the toluene peak (Step 6).

To further understand the reaction mechanism, we investigated the reaction in the presence of 2,4,6-tri-tert-butylphenol, which can serve as a "radical trap". In this manner, we can determine whether cleavage of S-C bond generates a radical with a significant lifetime. We assumed that if the reaction proceed via one-electron transfer, the carbon-based radical could abstract a hydrogen from 2,4,6-trimethylpehnol to produce phenoxyl radical, which has a distinctive peak at 626 nm in the UV-vis absorption spectrum. In our experiment, we mixed 1 equiv. of [**1**]NEt_4 with 5 equivalents of 2,4,6-tri-tert-butylphenol in the same DMF solution, followed by the injection of 1 equiv. of **d** in solution. At the completion of the reaction, however, no peak at 626 nm was evident, and the absorption spectrum was identical to the one obtained in the absence of 2,4,6-trimethylphenol. However, we still cannot draw firm mechanistic conclusions on the basis of this result, as the phenoxyl radical might have too short of a lifetime to be observed by UV-visible spectroscopy.

Since there is no convincing experimental evidence, we cannot distinguish between the mechanistic possibilities shown in Scheme 3.2.

3.2.A.2 Reaction of [1]NEt_4 with Salt (e) in THF

In the previous section, the GC-MS data indicated a weak peak at m/z = 92 that was attributed to toluene, but its intensity was too low to assign definitively. In order to confirm the formation of toluene, we synthesized athe *S*-4-tert-butylbenzyl tetramethylenesulfonium salt (**e**), which has a higher boiling point due to a bulky *tert*-butyl group at the *para* site.

After following the same procedure to workup the reaction and analyze products, GC and MS data were obtained in Figure 3.4. As before, three products were present (marked as A, B, C on the GC trace in Figure 3.4). The MS peak at m/z = 148 definitively corresponds to 4-tert-butyltoluene (Figure 3.3.B), despite its weak intensity compared with peaks of tetrahydrothiophene (A) and 4,4'-di-tert-butylbibenzyl (C) in the GC trace.

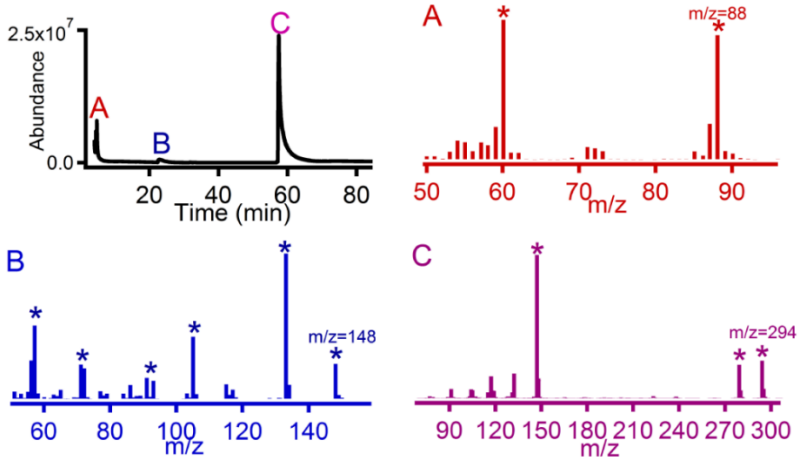

Figure 3.4 GC spectra derived from [**1**]NEt_4 reacting with **e**. And MS spectra corresponding to each peak on GC shows as following: tetrahydrothiophene (A), 4-tert-butyltoluene (B) and 4, 4'-di-tert-butylbibenzyl (C). Peaks marked with an asterisk (*) arise from fragmentation of the dominant product.

Further quantification of 4-tert-butyltoluene and di-tert-butylbibenzyl was done by following the same procedure and naphthalene was used as internal standard. The results showed that the reaction of [**1**]NEt_4 (0.0355 g, 0.0589 mmol) with **e** (0.0224 g, 0.0589 mmol) yielded 4-tert-butyltoluene (0.3075 mg, 0.0021mmol) and di-tert-butylbibenzyl (4.718 mg, 0.016mmol). Assuming that each was the only products, the theoretical yields values for 4-tert-butyltoluene and di-tert-butylbibenzyl would be 0.0054 mg (0.0589 mmol) and 8.6583 mg (0.0295 mmol). The yield of di-tert-butylbibenzyl is 54.49%, which is very comparable to the reaction of [**1**]NEt_4 with **d** discussed in Section 3.2.A.1.

Likewise, the reaction of [**1**]NEt_4 with **e** in the absence and presence of 2,4,6-tri-tert-butylphenol was performed, but GC-MS was used to detect the products. We hypothesized that if the percentage of 4-tert-butyltoluene is increased in the presence of TTBP, then the benzyl radical has a significant lifetime. Our GC-MS data shows that the reaction undergoes no change in the amount of 4-tert-butyltoluene and 4, 4'-di-tert-butylbibenzyl generated and there is no significant increase in the amount of 4-tert-butyltoluene, which means that the addition of TTBP does not influence the reaction pathway.

Although we still can't distinguish between the mechanistic possibilities shown in Scheme 3.2, the existence of both toluene and bibenzyl in in the reaction system of [**1**]NEt_4 reacting with **d** and **e** can be confirmed, the major product in both cases is bibenzyl.

3.2.A.3 Reaction of [1]NEt_4 with Sulfonium Salt (a) in THF

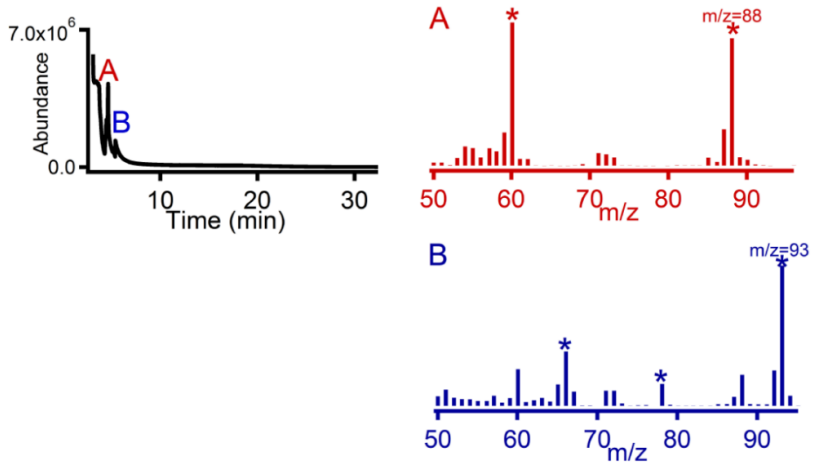

Figure 3.5 GC trace derived from reaction of [**1**]NEt_4 reacting with **a**. The MS data corresponding to each peak on the GC shows the following: tetrahydrothiophene in A and 2-picoline in B. Peaks marked with an asterisk (*) arise from the fragmentation of the dominant product. In B, 2-picoline is overlapping with partial tetrahydrothiophene.

The reaction of sulfonium salt *S*-(2-pyridylmethyl) tetramethylenesulfonium salt (**a**) with $[1]^-$ was also examined. Comparing the structure with the benzyl ring in **d**, the nitrogen atom in the pyridyl ring has a stronger ligating ability to the metal center, which can shorten the distance between the sulfonium group and Fe ion. For the product analysis, the same procedure was followed and three products were expected as tetrahydrothiophene, 2-picoline and 1,2-bis(2-pyridyl)ethane. The 1,2-bis(2-pyridyl)ethane product is supposed to be the major product if sulfonium salt **a** undergoes exactly the same mechanistic pathways as its analogue **d**.

Surprisingly, only the tetrahydrothiophene and 2-picoline products were observed in the resulting GC trace (Figure 3.5). The 1,2-bis(2-pyridyl)ethane product, which is

generated either by radical coupling or S_N2-type displacement, is not apparent. The other difference concerns the reaction speed; the reaction of [**1**]NEt_4 with **a** proceeds much faster than **d** according to our observations.

Given our previous assumption that the pyridyl ring of **a** can bind to Fe center while **d** cannot, the product distribution is quite reasonable. After the binding of nitrogen to Fe center, salt **a** goes through a faster inner-sphere electron transfer; for **d**, the reaction likely involves outer-sphere electron transfer. After electron reduction and S-C bond cleavage, pyridyl radical remains bound to the Fe center, inhibiting radical coupling or SN2-displacement to form 1,2-bis(2-pyridyl)ethane. The DFT calculations in the next section also supports this result.

A proposed mechanistic scheme is provided in Scheme 3.3. I will not describe this scheme in detail here, since it shares steps with the reactivity of **d** described above. Whereas, after reductive cleavage, the generated pyridyl radical or carbanion tends to abstract a hydrogen atom or proton, respectively to form 2-picoline (Step 2 or 4), instead of 1,2-bis(2-pyridyl)ethane.

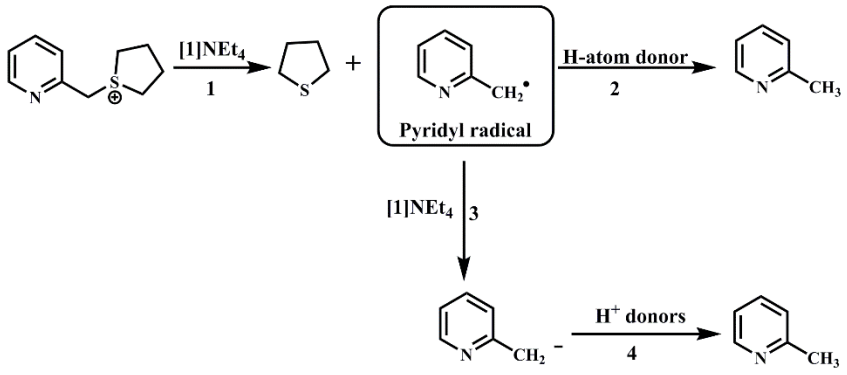

Scheme 3.3 Possible pathway for the products upon electron transfer and S-C bond cleavage in the reaction of [**1**]NEt_4 with **a**.

3.2.A.4 Reaction of [1]NEt_4 with Sulfonium Salt (e) in Acetone

In order to trace the source of the hydrogen atom in the various products (toluene, 4-tert-butyltoluene or 2-picoline), the reactions of [**1**]NEt_4 with **e** were performed in normal acetone (NA) and acetone-d_6 (DA), which can be H-donor. If H comes from the solvent, then the peak for 4-tert-butyltoluene is expected to appear at m/z = 149 in the MS data for the reaction in DA.

Following the general procedure, GC data was obtained (Figure 3.6). The black (solid) spectra were in normal acetone (NA), while the red (dashed) spectra was in acetone-d6 (DA). For these two trials, there is no substantial difference in the product distribution. Each trial has five peaks, corresponding to five products (Scheme 3.4).

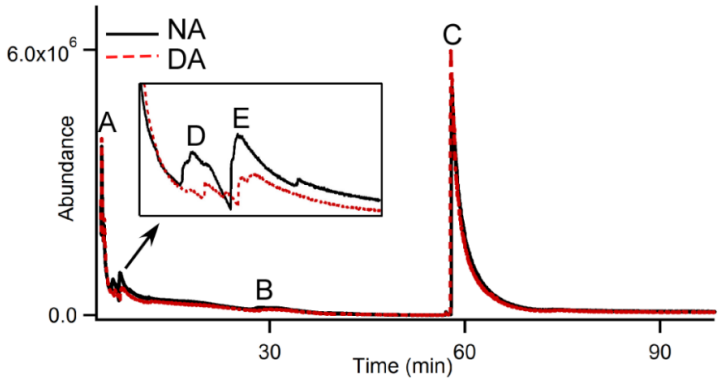

Figure 3.6 GC spectra derived from [**1**]NEt_4 reacting with **e**. The black (solid) spectra were in normal acetone (NA), while the red (dashed) spectra was in acetone-d_6 (DA). Five peaks (A to E) correspond to different products (Small window shows the detail peak information for D and E). The major components in each peak are assigned as A: tetrahydrothiophene; B: 4-tert-butyltoluene; C: 4, 4'-di-tert-butylbibenzyl; D: mesityl oxide; E: unknown compound.

Since solvent variation does not influence MS data for tetrahydrothiophene (A) and 4, 4'-di-tert-butylbibenzyl (C), Figure 3.7 here only summarizes the results for

products B, D and E. According to our assumption that H-atom comes from acetone, 4-tert-butyltoluene (B) should have m/z = 149 in acetone-d_6. However, in Figure 3.7 (Right), the weakness of peak at m/z =149 makes it hard to determine if there is a change due to use of acetone-d_6. Considering the large proportion of peak at m/z = 148 in both trials, other possible hydrogen sources must exist in the system and further study is required.

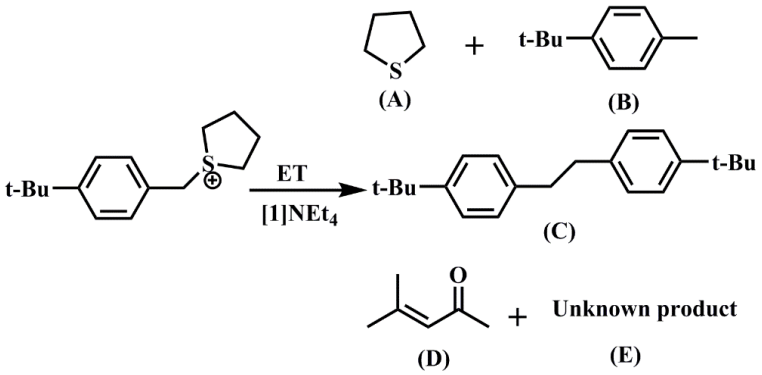

Scheme 3.4 Proposed products from the reaction of [**1**]NEt_4 with **e** in acetone. **A**: tetrahydrothiophene; **B**: 4-tert-butyltoluene; **C**: 4, 4'-di-tert-butylbibenzyl; D: mesityl oxide; E: unknown compound.

Comparing the GC trace with the one shown in Figure 3.4, two additional peaks (D and E) are present with m/z values of 98 and 101 in the acetone trial. Following the experimental data, product D appears to be mesityl oxide with a value of m/z = 98 in acetone; m/z increases to 108 in acetone-d6, as expected (Figure 3.7.D left and right). The presence of mesityl oxide supports the assumption that an active carbanion is generated by $2e^-$-reduction of the sulfonium cation. This carbanion is not only involved in proton transfer and S_N2 displacement to generate the main products (B and E), but it also initiates other side reactions, such as intramolecular aldol condensation of acetone to

form mesityl oxide (D) as a byproduct (Scheme 3.5). The intensity of mesityl oxide in Figure 3.6 indicates that this side reaction is quite favorable. Quantification of mesityl oxide from the products was attempted, however no accurate data was obtained due to the overlapping peaks of A, D and E in the GC trace.

For product E, although its structure is yet to be determined, the m/z shifts in acetone and acetone-d6 suggest that it must derive from side reactions initiated by reaction of the carbanion with acetone. One possibility is methyl isobutyl ketone, generated by the hydrogenation of mesityl oxide.

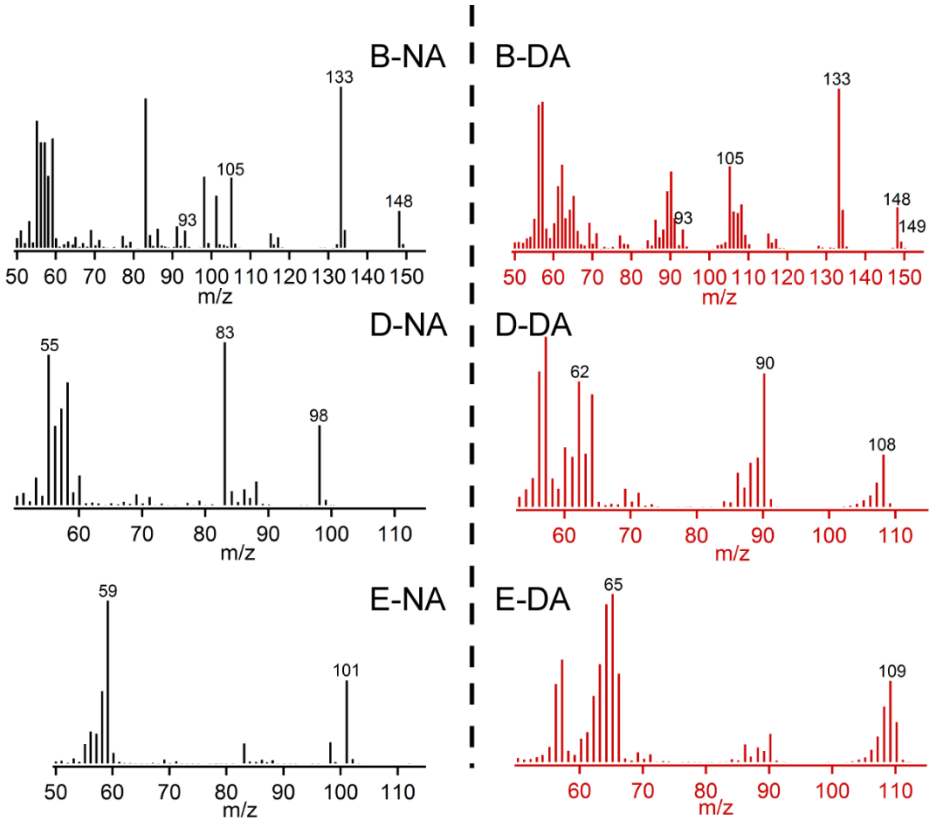

Figure 3.7 MS data corresponding to peaks B, D and E in GC trace (Figure 3.5) in normal acetone (NA, left) and acetone-d6 (DA, right). The major components in each peak are assigned as B: 4-tert-butyltoluene; D: mesityl oxide; and E: unknown compound.

In summary, even though the mechanism of toluene, 2-picoline and 4-tert-butyltoluene formation is not fully understood, product analyses indicate that the sulfonium salts can undergo reductive cleavage to generate carbon-based radicals. However, the initial radical products, likely participate in the fast second reduction to generate carbanions – a different process than the one used by the biological enzyme systems.[4] For example, in biotin synthase, the 5'-deoxyadenosyl radical generated by one-electron transfer and reductive cleavage is sufficiently stabilized as to allow it to abstract a hydrogen from the dethiobiotin substrate. Furthermore, the discrepancy in products between **a** and **d** (or **e**) suggests that the radical (or carbanion) from **a** is more reactive and is involved in the initiation of other chain reactions.

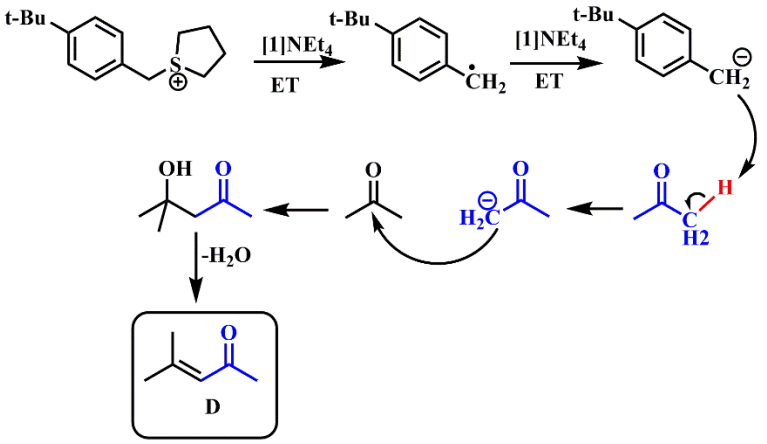

Scheme 3.5 Formation of Mesityl oxide (D) from the intramolecular aldol condensation of acetone, as initiated by the 4-tert-butylbenzyl carbanion.

3.2.B Electrochemical Properties of Sulfonium Salts

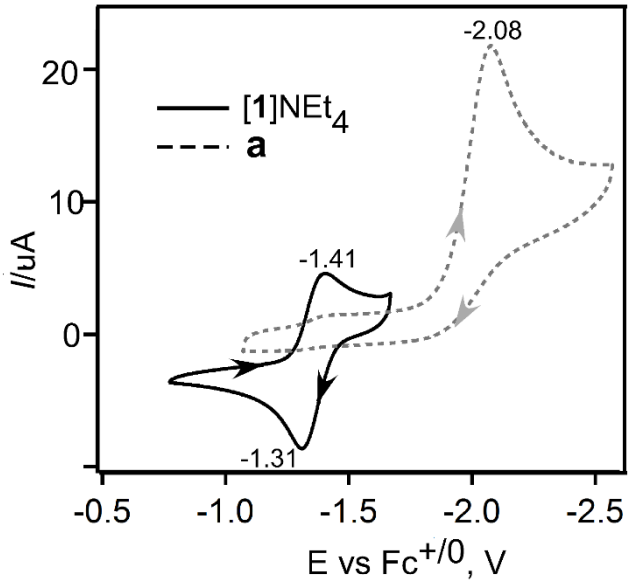

Figure 3.8 Cyclic voltammograms of [**1**]NEt_4 (Solid) and sulfonium salt **a** (Dashed) in DMF with 100 mM $(NBu_4)PF_6$ as the supporting electrolyte and a scan rate of 100 mV/s.

The redox properties of the sulfonium salts were examined with cyclic voltammetry in DMF solution with 0.1 M $(NBu_4)PF_6$ as the supporting electrolyte. Figure 3.8 represents a typical cyclic voltammogram for these sulfonium salts and electrochemical data are summarized in Table 3.2 (potential are reported vs $Fc^{+/0}$). As expected, each sulfonium salt exhibits an irreversible reduction event. Compared to the sulfonium salts in Holm's system,[36] the potentials are closer to the theoretical redox potential of the SAM cofactor.[33] Though observations and product analyses show clearly that [**1**]NEt_4 is capable of reductively cleaving the S-C bond of the sulfonium cations, there is a large energy barrier due to mismatch of ca. 600 mV in redox potential (Table 3.2), as is the case in the radical SAM enzymes.[33]

Table 3.2 Peak potentials *E* (in V vs $Fc^{+/0}$) of sulfonium salts as determined from CV.

	[1]NEt_4	**a**	**a'**	**a''**	**b**	**d**	**e**
Redox potential (V vs $Fc^{+/0}$)	-1.36	-2.08	-2.05	-1.96	-1.90	-2.11	2.13

In SAM enzymes studies, a great deal of research has been focused on elucidating how Nature surmounts a huge energy barrier of 1.32 V in the difference in midpoint potentials for free SAM and the [Fe_4S_4] cluster, and how this unfavorable process happens. Several explanations were discussed in Chapter 1. Upon binding SAM and substrate, the potential of the unique iron cluster is lowered; simultaneously ligation to the [Fe_4S_4] active site elevates the reduction potential of SAM, thus decreasing the barrier to its reductive cleavage.[33] A further consideration is attributable to the transformation of the unique iron site from penta-coordination to the more favorable pseudo-octahedral after the electron transfer. Not least important is orbital overlapping that is necessary to facilitate inner-sphere electron transfer.[57] Spectroscopic studies have provided evidence for direct orbital overlap between the sulfonium cation and [Fe_4S_4] cluster.[57]

The crystal structure of [**1**]NEt_4 reported in Chapter II shows a trigonal bipyramidal geometry (Figure 3.9). An isopropanol molecule that resides in the axial position can be easily replaced by substrates. The Fe-O4 bond length is 2.190 Å. The big cavity on the top provides space for sulfonium salts to access to the Fe(II) center. Compared to isopropanol, the pyridyl ring on **a** is expected to have a larger affinity for the Fe(II), resulting in a shorter bond length after binding. This bond length might be comparable to O/N_{SAM}-Fe distance in the SAM enzymes,[57] thus decreasing the energy barrier in the same manner as the enzymes. Meanwhile the affinity of **a** to Fe(II) is

greater than **d**, which might account for our observation that the reaction of [**1**]NEt_4 with **a** is much faster than **d**.

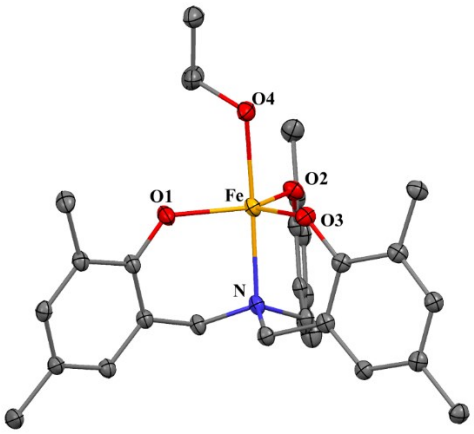

Figure 3.9 Thermal ellipsoid plots (50% probability) derived from the X-ray crystal structure of complex [**1**]$^{-}$. Non-coordinating solvent molecules, counterions, and most hydrogen atoms have been omitted for clarity. Bond length (Å) Fe–O4 = 2.190(3), Fe–O1 = 1.963(3), Fe–O2 = 1.981(3), Fe–O3 = 2.042(3), Fe–N1= 2.212 (3). In SAM enzymes families, approximately bond lengths: Fe-N_{AdoMet} = 1.9~2.4, Fe-O_{AdoMet} = 1.98 ~ 2.51.[57]

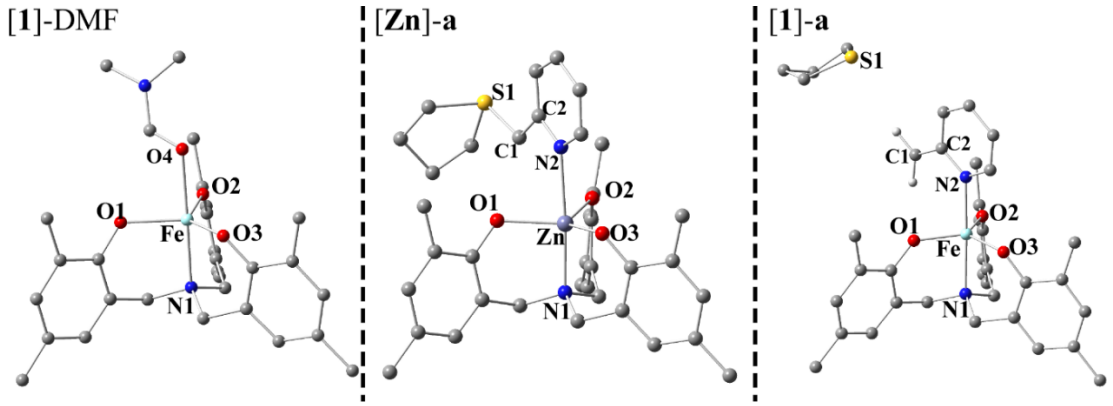

Figure 3.10 Idealized structures of three models from DFT calculation: ([**1**]-DMF (Left): DMF displaces isopropanol on the top site. Non-coordinating solvent molecules, counterions, and most hydrogen atoms have been omitted for clarity. [**Zn**]-**a** (Middle): the Fe (II) center was replaced by redox-inactive Zn(II), and $[Zn]^{-}$ was bound to **a** in the axial site with nitrogen binding to central Zn(II). [**1**]NEt_4-**a** (Right): $[\mathbf{1}]^{-}$ was bound to **a** in the axial site.

Three DFT models were calculated via geometry optimizations. The first one involves [**1**]$^-$ with DMF in the axial site (**[1]-DMF**), assuming a penta-coordination geometry, $S = 2$ high spin state, and overall charge of -1. In the second model (**[Zn]-a**), the Fe(II) center was replaced by redox-inactive Zn(II) and **a** was bound in the axial site (S=0 and overall charge of -1). In the third model (**[1]-a**), [**1**]$^-$ was bound to **a** in the axial site ($S = 2$ high spin state , and overall charge of 0).

The resulting models are displayed separately in Figure 3.10 and metric parameters are summarized in Table 3.3. For both **[Zn]-a** and **[1]-a**, the distances between metal center and N2 are comparable to the distance between the unique Fe and –NH_2 donor of SAM in the enzymes.[57] In model **[Zn]-a**, the bond distance of 2.4 Å between Zn and N2 suggests the formation of the bond, which mimics the interaction between the metal complex and **a** before the electron transfer.

Table 3.3 Metric parameters for the resulting models, selected bond distance for [**1**]-DMF, **[Zn]-a** and **[1]-a**.

Distance (Å)	[**1**]-DMF	[**Zn**]-**a**	[**1**]-**a**
Fe-O4/N2	2.27	2.41	2.21
C1-S1 in **a**	---	1.82	4.41
C1-C2	---	1.50	1.40
Fe-O1	2.04	2.04	1.90
Fe-O2	1.99	2.03	1.90
Fe-O3	1.96	1.96	1.91
Fe-N1	2.24	2.16	2.31

The starting geometry of model **[1]-a** was similar to the one obtained for the **[Zn]-a** (Figure 3.10 (Right)). However, during the course of the optimization, the S-C bond of

a spontaneously cleaves. The resulting structure resembles the species generated after electron transfer. The distance of 4.413 Å between S1 and C1 is evidence of bond-cleavage. The spin population of C1 of methylene is -0.54, indicating the formation of a bound radical. This computation result highlights the favorability of the reductive cleavage and the formation of carbon-based radical.

In the previous quantification and analyses section, the UV-visible and GC-MS studies in the presence of 2,4,6-tri-tert-butylphenol suggestes that the pyridyl radical may have a very short lifetime. Further connection between these results and DFT calculations needs to be established.

3.2.C Reactivity Studies of [1]NEt_4 Reacting with a and d Salts

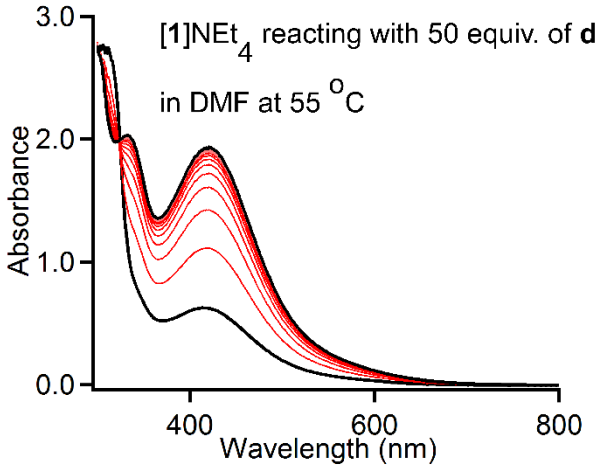

Figure 3.11 Time-resolved absorption spectra for the reaction of [**1**]NEt_4 with 50 equivalents of sulfonium salt **d** in DMF at 55ºC. ([Fe^{2+}] = 0.28 mM); spectra were collected at an interval of 10 s. The path length of the cuvette was 1.0 cm.

We investigated the reactivity of [**1**]NEt_4 with sulfonium salts by monitoring the intensity of the band at 418nm as a function of time under different sulfonium concentrations and various temperatures. All UV-visible kinetic experiments were carried out in a similar manner: solutions of [**1**]**NEt_4** and sulfonium salts in DMF were prepared separately in glovebox, and 4.00 mL of [**1**]**NEt_4** were transferred to a glass cuvette. Different amounts of the sulfonium salt solutions were drawn by a syringe and injected into the [**1**]NEt_4 solution while stirring. The UV-visible spectra were measured at a range of temperatures.

All of these reactions showed a dramatic increase in absorption intensity at 418 nm, which corresponds to the oxidation of [**1**]NEt_4 to the corresponding ferric complex. After the injection of **d** or **a**, the solution containing [**1**]NEt_4 turned to brown at different speeds, supporting the hypothesis that the sulfonium salts are capable of oxidizing the Fe(II) complex.

Figure 3.11 displays time-resolved absorption spectra of the reaction of [**1**]NEt_4 with **d** at 55^{o}C. In addition to the dominant peak at 418 nm, a feature at 330 nm is also apparent in the oxidized spectrum. As discussed in Chapter 2, these absorption bands likely arise from phenolate→Fe(III) charge transfer transitions. In the following sections, we will discuss kinetics data obtained for the reaction of [**1**]NEt_4 with **d** and **a** from two different aspects: i) dependence of rate on sulfonium concentration at a given temperature and, ii) the temperature dependence of the reaction rate.

3.2.C.1 Dependence on S-benzyl Tetramethylenesulfonium Salt (d) Concentration

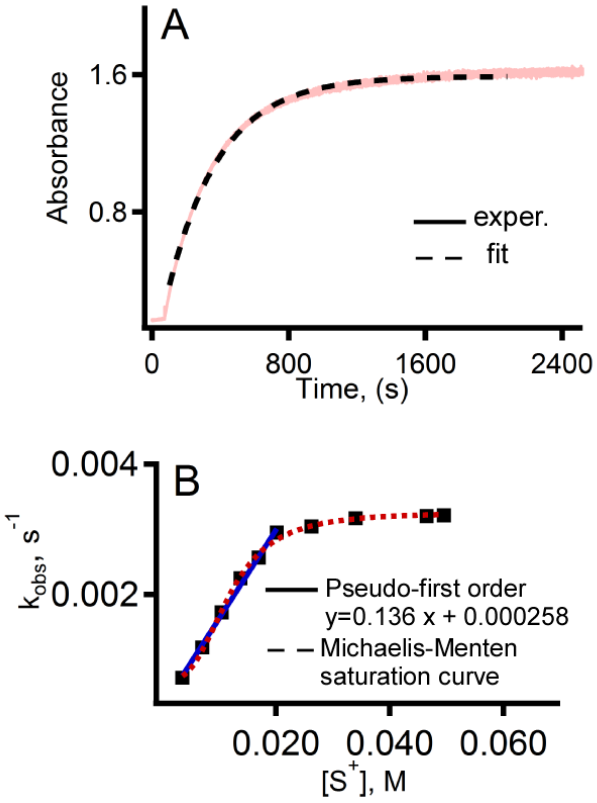

Figure 3.12 A: Experimental kinetic trace recorded for [**1**]NEt_4 at λ = 418 nm as a function of time always fits nicely a single exponential for the reaction of [**1**]NEt_4 with 60 equiv. of **d** at 20 ◦C; B: Observed pseudo-first-order rate constant, k_{obs}, as a function of [S^+] for reaction of [**1**]NEt_4 with 5, 10, 20, 30, 40, 50, 60, 80, 100, 120, 140, 150 equivalents of **d** in DMF solvent, T = 20 ◦C. Whole trends presents typical Michaelis-Menten enzyme kinetics saturation curve, initial points from 5 to 60 equivalents of excess **d** fit pseudo-first order and second-order rate constant is obtained from the equation (y = 0.1361 x + 0.000268).

Specifically, the kinetics studies for the reaction of [**1**]NEt_4 with the benzyl sulfonium cation (**d**) were performed under pseudo-first-order conditions in which the concentration of **d** was in excess and the concentration of [**1**]NEt_4 was kept constant ([Fe] = 0.36 mM in DMF). The kinetic trace for the increase of absorbance at 418 nm is nicely

fit by a single exponential curve (Figure 3.12.A). By using different ratios of metal complex and sulfonium cation, values for the pseudo-first-order rate constant (k_{obs}) were obtained (Table 3.3) and the plot of k_{obs} as a function of $[S^+]$ is shown in Figure 3.12.B.

Two important pieces of information are derived from Figure 3.12.B. Firstly, the increase of sulfonium concentration tends to increase rate of reaction. When $[S^+]$ is low (from 5 to 60 equivalents of excess **d**), k_{obs} and $[S^+]$ have a linear relationship, in which the second-order rate constant is derived from its slope ($k_2 = 0.136\ M^{-1}s^{-1}$). The second one is based on all points shown in Figure 3.12.B (from 5 to 150 equivalents). Once the excess of sulfonium salt reaches the saturation point, the rate constant no longer increases and the whole trend is reproduced by a typical Michaelis-Menten kinetic saturation curve in the dash line, which is very common in enzyme kinetics studies.

3.2.C.2 Dependence on S-benzyl Tetramethylenesulfonium Salt (a) Concentration

In the case of the reaction of 2-methylpyridyl sulfonium salt **a** with [**1**]NEt_4, our products analysis suggested that the reaction may proceed via a different mechanism after the shared initial step (i.e., one electron reduction of sulfonium salt to generate carbon-based radical). It would, therefore, be interesting to perform kinetic studies to further investigate this reaction. In order to compare results for **d** and **a**, we initially planned to monitor kinetic studies at room temperature as well. However this reaction is more than 200 times faster than **d** and finishes in less than 10 seconds, making it virtually impossible to measure an accurate second-order rate constant.

At this point, we lowered the temperature to 0 ˚C and –30 ˚C. In this thesis, we will only show kinetic traces and analyses for data collected at 0 ˚C. By fitting the kinetics traces to single exponentials and plotting pseudo-first order rate constants verse various [S^+], the kinetic plot in Figure 3.13 was obtained. The second-order rate constant (k_2) measured for **a** is 4.3 $M^{-1}s^{-1}$ at 0 ˚C, about 32 times faster than **d** at 20 ˚C. This confirms the direct observation that the color of metal complex changed faster in the presence of **a** than **d**.

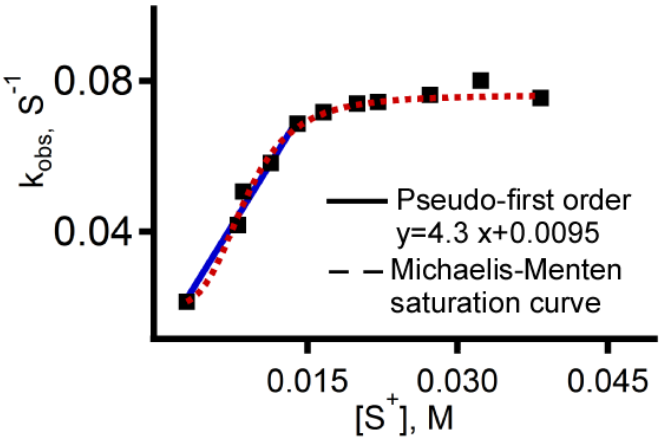

Figure 3.13 Observed pseudo-first-order rate constant, k_{obs}, as a function of [S^+] for reaction of [**1**]NEt_4 with 10, 20, 30, 40, 50, 60, 70, 80, 100, 120, 140 equivalents of **a** in DMF solvent, T = 0 ◦C. Whole trends presents typical Michaelis-Menten enzyme kinetics saturation curve, initial points from 10 to 50 equivalents of **a** fit pseudo-first order and second-order rate constant is obtained from the equation (y = 4.3002 x + 0.0095).

It is not really suitable to compare second-order rate constants measured at different temperatures. However, given the striking difference in second-order rate constants of **a** and **d**, we can conclude that the nature of the sulfonium salts does have a dramatic effect on reaction rates. The primary difference is the presence of a pyridyl

donor in **a**, which can orient the S close to Fe(II). In Chapter 2, we mentioned that the crystal structure of [**1**]NEt_4 features a trigonal-bipyramidal Fe(II) center donor, with three phenolate donors in equatorial plan and one axial nitrogen, leaving one open spot for substrate coordination. This molecular geometry enhance the electron-transfer process if there is a metal-binding ligand on the substrate's structure.

Considering the differentiation of the product analyses and second-order rate constants for salt **a** and **d** together, the ability of sulfonium salts to coordinate to Fe(II) affects the rate of electron transfer. And we suggest that **a** experiences inner-sphere electron transfer, while outer-sphere electron transfer occurs for salt **d**.

If this hypothesis is valid, then it can explain that why 2-picoline is the primary product of the reaction of **a** with [**1**]NEt_4, rather than the 2,2'-bipyridyl that would arise from coupling of two equivalents (as happens in the case of **d**). Salt **a** has a stronger affinity for [**1**]NEt_4, thus the resulting radical may remain bound to the Fe center even after the electron transfer and the generation of tetrahydrothiophene. Steric effects prohibit this radical or carbanion from approaching other molecules to generate the coupled product.

However, due to the lack of a donor group in **d**, the benzyl carbon-based radical or carbanion would be free in solution, thus increasing the possibility of coupling with another radical or attacking a second equivalent of **d** (as the carbanion). Meanwhile, this prediction could also explain why the reaction of **a** with [**1**]NEt_4 is faster than **d**. For inner-sphere electron transfer, **a** undergoes one electron transfer via a chemical bridge. In contrast, the outer-sphere electron transfer to **d** would be much slower. More

experiments need to be done to confirm these hypothesis about either inner-sphere or outer-sphere electron transfer in our synthetic system.

3.2.C.3 Dependence on Temperature

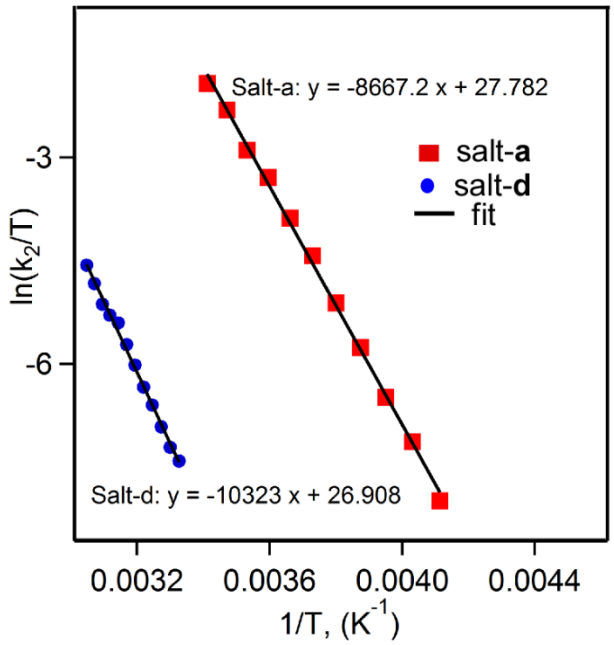

Figure 3.14 Eyring plot for the reaction of [**1**]NEt_4 with salts **a** (■) and **d** (●). Second-order rate constant (k_2) were obtained by dividing the pseudo-first constant by [S^+]. Each data point represents one reaction. Salt-a): 20 equivalents of excess **a** in DMF at an interval of 5 ˚C over a temperature range of -30 to 20 ˚C. Salt-d): 50 equivalents of excess **d** in DMF at an interval of 2.5 ˚C over a temperature range of 27.5 to 55 ˚C.

The direct observation of color change after injection of the sulfonium salts indicates that the reaction of [**1**]NEt_4 with sulfonium salts is highly favorable in our synthetic system. We carried out temperature-dependent experiments to calculate thermal activation parameters for the ET reaction. In these experiments, we measured the

second-order rate constant (k_2) over the temperature range of 27.5 to 55 ˚C for **d** and of -30 to 20 ˚C for **a**, respectively, and constructed Eyring plots for each sulfonium salt (Figure 3.14). The enthalpies and entropies of activation can be calculated from the slope and intercept of the plots, and the resulting values are summarized in Table 3.4.

As we know, activation enthalpy, $\Delta H^{\neq}$, represents the difference in energy between the ground state and the transition state in a chemical reaction. The higher the activation enthalpy, the more energy is required for the reaction to proceed. In general, a reaction will take place faster if the $\Delta H^{\neq}$ value is low. In our system, the midpoint potential for [**1**]NEt_4 is -1.36 V and the reduction potentials measured for **a** and **d** -2.08 V and -2.12 V, this electrochemical result indicates that the reactions of salts **a** and **d** with [**1**]NEt_4 are not favorable. So positive $\Delta H^{\neq}$, in both cases, are reasonable. Because $\Delta H^{\neq}$ for **a** is slightly smaller than **d**, the reaction of **a** with [**1**]NEt_4 can undergo faster than **d**, which corresponds to the reaction observation and the second-order rate constants. However, further exploration is required to connect the small difference in activation energies and the apparent difference in rate constants between **a** and **d**.

Table 3.4 Summarization of $\Delta H^{\neq}$ and $\Delta S^{\neq}$ calculated from plots in **Figure 3.13** for **a** and **d**.

Sulfonium salts reacting with [**1**]NEt_4	Plots in **Figure 3.10**	$\Delta H^{\neq}$, kcal/mol	$\Delta S^{\neq}$, cal/(K*mol)
a	Salt-a	17.2	7.98
d	Salt-d	20.5	6.25

Equation used for the calculation: $\ln(k_2/T) = (-\Delta H/R)x(1/T) + \ln(k_B/h)+(\Delta S/R)$

thus: Slope = $-\Delta H/R$; Intercept = $\ln(k_B/h)+(\Delta S/R)$

constants: R = 8.314 J/(K, mol), $k_B = 1.38x10^{-23}$ J/K,

$h = 6.63x10^{-34}$ J/S

For $\Delta S^{\neq}$, positive changes in entropy of activation indicate that the system becomes more disordered in the transition state, characteristic of S-C bond cleavage as the rate-determining step, for both **a** and **d**. The reason why $\Delta S^{\neq}$ for **a** is slightly larger than **d**, though, can't be clarified, the binding of $\Delta H^{\neq}$ and $\Delta S^{\neq}$ indicates that the reaction for **a** is easier to happen, compared with **d**.

3.3 Conclusions

This work has provided an example of a simplified biomimetic model for the SAM-dependent enzymes that attempts to replicate important properties of the unique Fe center. The reactivity studies have demonstrated that this system has the intrinsic ability to reductively cleave the S-C bond of sulfonium cations, resulting in the formation of tetrahydrothiophene and an unstable radical. The reaction appears to proceed via either the one-electron pathway (as occurs in the enzymes) or two-electron pathway, similar to the one observed in Holm's system. And because our conclusion of probable reaction mechanisms are predicated on product analysis and not on observations of reactive intermediates, we cannot insist upon such pathways. Further studies have to be done to provide more detailed information about electron transfer and bond interactions between [**1**]NEt_4 and sulfonium salts.

3.4 Experimental Section

3.4.A General

All reagents and solvents were purchased from commercial source and used as received unless otherwise noted. All syntheses and handling of air-sensitive materials were carried out under an inert atmosphere using a Vacuum Atmospheres Omni-Lab glovebox equipped with a freezer setting to -25 ^{0}C. NMR spectra were collected at room temperature with a Varian 300 or 400 MHz spectrometer. UV – visible spectra were collected with an Agilent 8453 diode array spectrometer. Electrochemical studies were conducted by BASi MF-9092 Potentiostat/Galvanostat in dimethylformamide (DMF) solutions containing the supporting electrolyte of $(C_4H_9)_4N^+ \cdot PF^-_6$ 100 mM under an inert atmosphere. The reference electrodes used were an Ag/AgCl RE - 5. A platinum wire was used as an auxiliary electrode and platinum was used as a working electrode for the cyclic Voltammetry (CV). All redox potentials of iron complex are referred to the ferrocenium/ferrocene couple ($Fc^{+/0}$).

3.4.B Synthesis of Sulfonium Salts

Sulfonium salt a: S-(2-pyridylmethyl) Tetramethylenesulfonium PF_6. [58]

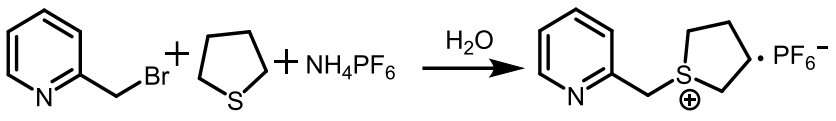

2-(Bromomethyl) pyridine·HBr (2.54 g, 10.0 mmol) in water (20.0 ml) was treated with tetrahydrothiophene and ammonium hexafluorophosphate (3.50g, 21.5 mmol). After stirring at room temperature for 10 hours, white solid which gradually precipitated was filtered and dried under vacuum then dissolved in acetone, titrated with saturated aqueous $NaHCO_3$ to PH= ~7. The mixture was dried under reduced vacuum and the resulting solid was washed with water (2x10 ml) and the remaining solid was dried under vacuum and recrystallized from acetone-Et_2O to give *S*-(2-pyridylmethyl) tetramethylenesulfonium PF_6^- as white powder. Yield: 2.23 g, 68.2%. ^1H NMR (CD_2Cl_2, 400 MHz) δ 8.54 (s, 1H), 7.80 (m, 1H), 7.49 (m, 1H), 7.37 (m, 1H), 4.78 (s, 2H), 3.35-3.54 (m, 4H), 2.05-2.19 (m, 4H). ^{13}C NMR (CD_2Cl_2, 100 MHz) δ 150.1, 149.1, 148.2, 138.8, 124.62, 47.79, 43.85, 28.96.

Sulfonium salt a': S-(3-pyridylmethyl) Tetramethylenesulfonium PF_6^-

By the same procedure, 3-(Bromomethyl) pyridine·HBr (2.34 g, 9.24 mmol), tetrahydrothiophene (1.84 g, 20.9 mmol) and ammonium hexafluorophosphate (3.22 g, 19.8 mmol) in water gave white powder as the right product. Yield: 1.52 g, 50.5%. ^1H NMR ($(CD_3)_2SO$), 400 MHz) δ 8.75 (s, 1H), 8.65 (d, 1H), 7.99 (d, 1H), 7.51 (t, 1H), 4.56 (s, 2H), 3.43-3.48 (m, 4H), 2.16-2.25 (m, 4H). ^{13}C NMR ($(CD_3)_2SO$), 100 MHz) δ 151.3, 142.5, 138.58, 124.62, 124.5, 43.52, 42.89, 28.62.

Sulfonium salt a'': S-(4-pyridylmethyl) Tetramethylenesulfonium PF_6^-

By the same procedure, 4-(Bromomethyl) pyridine·HBr (1.27 g, 5.02 mmol), tetrahydrothiophene (1.00 g, 11.3 mmol) and ammonium hexafluorophosphate (1.75 g, 10.7 mmol) in water gave light pink powder as the right product. Yield: 0.759 g, 46.5%. ^{1}H NMR ($(CD_3)_2SO$, 400 MHz) δ 8.67 (d, 1H), 7.56 (d, 1H), 4.53 (s, 2H), 3.43-3.49 (m, 4H), 2.18-2.28 (m, 4H). ^{13}C NMR ($(CD_3)_2SO$, 100 MHz) δ 150.6, 139.04, 125.06, 43.63, 43.34, 28.26.

Sulfonium salt b: S-(3-pyridyl) Tetramethylenesulfonium PF_6^-

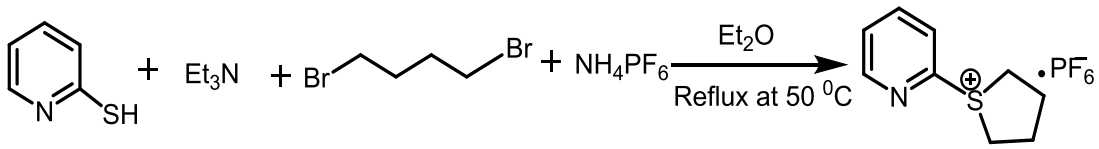

To the mixture of 2-mecaptopyridine (1.01 g, 9.08 mmol) and 1, 4-dibromobutane (5.88g, 27.2 mmol) in Et_2O (10.0 ml), triethylamine (1.39g, 13.6mmol) was added and a white solid immediately began to precipitate. After refluxing at 50 ^{0}C for 3 hours, the mixture was treated with another 10 ml Et_2O and washed with 5% NaOH(2 x 20 ml) and brine (2 x 20 ml). The organic layer was collected, dried with $MgSO_4$ and concentrated to give crude material.

The crude material was dissolved in acetone (30.0 ml), and then ammonium hexafluorophosphate (2.22 g, 13.6 mmol) was added. After stirring overnight at room temperature, white solid was precipitated. The solid was filtered and washed with acetone. Large amount of Et_2O was added to the filtrate to induce crystallization of white

powder. The white powder was washed with water (2 x 20 ml), ethanol (2 x 20 ml) and Et_2O (2 x 20 ml) and dried under vacuum to give the right product. Yield: 1.21 g, 42.8%. ^{1}H NMR ($(CD_3)_2SO$, 400 MHz) δ 8.79 (s, 1H), 8.17 (s, 2H), 7.76 (s, 1H), 3.91(m, 2H), 3.82 (m, 2H), 2.23 (app q, 4H). ^{13}C NMR ($(CD_3)_2SO$, 100 MHz) δ 151.0, 147.6, 139.79, 127.58, 127.41, 46.26, 28.69.

Sulfonium salt d: S-(phenyl) Tetramethylenesulfonium PF_6^-

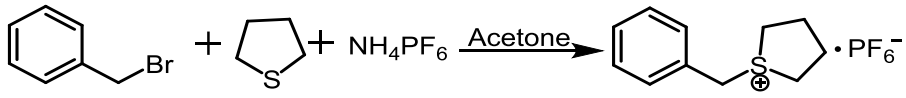

Benzyl bromide (1.88 g, 10.9 mmol) was dissolved in acetone (20.0 ml) then tetrahydrothiophene (1.10 g, 12.4 mmol) and ammonium hexafluorophosphate (1.97 g, 12.1 mmol) were added. White solid formed immediately. After stirring at 40 ^{0}C for 16 hours, the solid was filtered and washed with acetone. Large amount of Et_2O was added to the filtrate to induce the crystallization of crude product. The resulting white powder was washed with water (20 ml * 2), ethanol (2 x 20 ml) and Et_2O (2 x 20 ml) and dried under vacuum to give white powder as right product. Yield: 2.35 g, 65.4%. ^{1}H NMR ($(CD_3)_2SO$), 400 MHz) δ 7.46-7.55 (m, 5H), 4.53 (s, 2H), 3.35-3.54 (m, 4H), 2.15-2.22 (m, 4H). ^{13}C NMR ($(CD_3)_2SO$), 100 MHz) δ 130.35, 129.80, 129.51, 129.39, 44.92, 42.55, 39.43, 28.09.

Sulfonium salt c: S-(2-pyridylethyl) Tetramethylenesulfonium PF_6^-

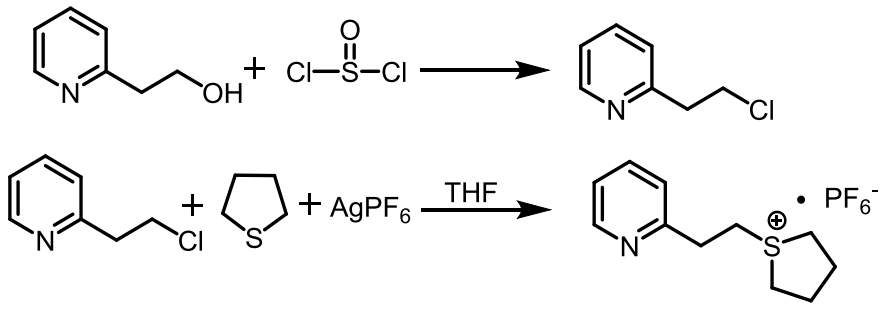

2-(2-chloroethyl)pyridine 2-(2-hydroxylethyl) pyridine (3.00 g, 24.4 mmol) was dropwised into $SOCl_2$ (11.6 g, 97.4 mmol) slowly at 0 ^{0}C. The mixture was refluxing at 80 ^{0}C for 1 hour to give a clear dark yellow solution. And the reaction was concentrated into yellow powder. The resulting powder was further dissolved in ca. 10.0 ml water, and solution's PH value was adjusted to ca. 12 by KOH solution. The aqueous solution was exacted with DCM and the combined organic phases were dried over $MgSO_4$ and DCM was vacuum off to give dark orange oil as the right product. Yield: 2.69 g, 78.1%. ^{1}H NMR ($CDCl_3$, 400 MHz) δ 8.5310, 7.5982, 7.1195~7.2600, 3.8983, 3.1974. ^{13}C NMR ($CDCl_3$, 100 MHz) δ 157.77, 149.49, 123.66, 123.36, 121.83, 43.54, 40.96.

S-(2-pyridylethyl) Tetramethylenesulfonium PF_6^- 2-(2-chloroethyl)pyridine (0.342 g, 2.41 mmol), tetrahydrothiophene (0.240g, 2.73 mmol) and $AgPF_6$ (0.669 g, 2.65 mmol) were dissolved in 10 ml THF and stirring for 1 day to give dark brown suspension. The mixture solution was concentrated into black powder. Black powder was dissolved in acetone and filtered. The filtrate was dried to give pale brown powder as the right product. Yield: 0.514, 63.5%. ^{1}H NMR ($(CD_3)_2SO$, 400 MHz) δ 8.5802 (d, 1H), 7.9340 (t, 1H), 7.5482 (d, 1H), 7.4418 (t, 1H), 4.0186 (t, 1H), 3.2962 (t, 2H), 2.9953 (t,

4H), 1.9542 (t, 4H). ^{13}C NMR ($(CD_3)_2SO$, 100 MHz) δ 157.39, 149.82, 138.59, 124.73, 122.96, 43.78, 41.18, 34.41, 30.52.

3.4.C Analyses and Quantifications of Organic Products

All of GC-MS experiment followed the general procedure. [**1**]NEt_4 (26.2 mg, 0.044 mmol) was dissolved in 2 ml THF, and *S*-benzyl tetramethylenesulfonium PF_6^- (**d**) **(**14.1 mg, 0.044 mmol) was added. And the reaction suspension was allowed to stir at room temperature for 18 hours. Then the reaction residue was gone through column packed with aluminum oxide as stationary phase and hexane as mobile phase, about 10 ml organic components were collected and analyzed by GC-MS. After removal of the solvents, white crystalline residue was quantified by using GC-FID and naphthalene was used as an internal calibration standard. In order to quantify bibenzyl product, a relative response factor (R) of bibenzyl to naphthalene was tested and a value of 0.8711 was obtained.

Both of products were also characterized by ^{1}H NMR spectroscopy**.**

Tetrahydrothiophene: ^{1}H NMR (400 MHz, CD2Cl2) δ 2.76 (m, 4H), 1.89 (m, 4H).

Bibenzyl: ^{1}H NMR (400 MHz, CD2Cl2) δ 7.18 (m, 10H), 2.9167 (s, 4H).

REFERENCE

1. Booker, S. J.; Cicchillo, R. M.; Grove, T. L., *Curr. Opin. Chem. Biol.* **2007,** *11* (5), 543-552.

2. Fontecave, M.; Atta, M.; Mulliez, E., *Trends Biochem. Sci.* **2004,** *29* (5), 243-249.

3. Frey, P. A.; Ballinger, M. D.; Reed, G. H., *Biochem. Soc. Trans.* **1998,** *26*, 304-310.

4. Frey, P. A.; Hegeman, a. D.; Ruzicka, F. J., *Critical Reviews in Biochemistry and Molecular Biology* **2008,** *43*, 63-88.

5. Markham, G. D.; Hafner, E. W.; Tabor, C. W.; Tabor, H., *J. Biol. Chem.* **1980,** *255* (19), 9082-9092.

6. Van Lanen, S. G.; Iwata-Reuyl, D., *Biochemistry* **2003,** *42* (18), 5312-5320.

7. Stoner, G. L.; Eisenberg, M. A., *J. Biol. Chem.* **1975,** *250* (11), 4037-43.

8. Björk, G. R.; Durand, J. M. B.; Hagervall, T. G.; Leipuvien≐, R.; Lundgren, H. K.; Nilsson, K.; Chen, P.; Qian, Q.; Urbonavičius, J., *FEBS Lett.* **1999,** *452* (1–2), 47-51.

9. Taylor, F. R.; Cronan, J. E., *Biochemistry* **1979,** *18* (15), 3292-3300.

10. Chiang, P. K.; Gordon, R. K.; Tal, J.; Zeng, G. C.; Doctor, B. P.; Pardhasaradhi, K.; McCann, P. P., *FASEB J.* **1996,** *10* (4), 471-80.

11. Chirpich, T. P.; Zappia, V.; Costilow, R. N.; Barker, H. A., *J. Biol. Chem.* **1970,** *245*, 1778-1789.

12. Knappe, J.; Schmitt, T., *Biochem. Biophys. Res. Commun.* **1976,** *71*。

13. Grove, T. L.; Benner, J. S.; Radle, M. I.; Ahlum, J. H.; Landgraf, B. J.; Krebs, C.; Booker, S. J., *Science* **2011,** *332* (6029), 604-607.

14. Duin, E. C.; Lafferty, M. E.; Crouse, B. R.; Allen, R. M.; Sanyal, I.; Flint, D. H.; Johnson, M. K., *Biochemistry* **1997,** *36* (39), 11811-11820.

15. Lepore, B. W.; Ruzicka, F. J.; Frey, P. A.; Ringe, D., *Proc. Natl. Acad. Sci. U.S.A.* **2005,** *102* (39), 13819-13824.

16. Cosper, N. J.; Booker, S. J.; Ruzicka, F.; Frey, P. A.; Scott, R. A., *Biochemistry* **2000,** *39* (51), 15668-15673.
17. Boal, A. K.; Grove, T. L.; McLaughlin, M. I.; Yennawar, N. H.; Booker, S. J.; Rosenzweig, A. C., *Science* **2011,** *332* (6033), 1089-1092.

18. Moss, M.; Frey, P. A., *J. Biol. Chem.* **1987,** *262* (31), 14859-62.

19. Frey, P. A.; Hegeman, A. D., *Enzymatic Reaction Mechanism* **2007**.

20. Jarrett, J. T., *Archives of Biochemistry and Biophysics* **2005,** *433* (1), 312-321

21. Taylor, A. M.; Farrar, C. E.; Jarrett, J. T., *Biochemistry* **2008,** *47* (35), 9309-9317.

22. Berkovitch, F.; Nicolet, Y.; Wan, J. T.; Jarrett, J. T.; Drennan, C. L., *Science* **2004,** *303* (5654), 76-79.

23. Hegazi, M. F.; Borchardt, R. T.; Schowen, R. L., *J. Am. Chem. Soc.* **1979,** *101* (15), 4359-4365.

24. Woodard, R. W.; Tsai, M. D.; Floss, H. G.; Crooks, P. A.; Coward, J. K., *J. Biol. Chem.* **1980,** *255* (19), 9124-9127.

25. Cannone, J.; Subramanian, S.; Schnare, M.; Collett, J.; D'Souza, L.; Du, Y.; Feng, B.; Lin, N.; Madabusi, L.; Muller, K.; Pande, N.; Shang, Z.; Yu, N.; Gutell, R., *BMC Bioinformatics* **2002,** *3* (1), 15.

26. Toh, S.-M.; Xiong, L.; Bae, T.; Mankin, A. S., *RNA* **2008,** *14* (1), 98-106.

27. Schlunzen, F.; Zarivach, R.; Harms, J.; Bashan, A.; Tocilj, A.; Albrecht, R.; Yonath, A.; Franceschi, F., *Nature* **2001,** *413* (6858), 814-821.

28. Kehrenberg, C.; Schwarz, S.; Jacobsen, L.; Hansen, L. H.; Vester, B., *Mol. Microbiol.* **2005,** *57* (4), 1064-1073.

29. Giessing, A. M. B.; Jensen, S. S.; Rasmussen, A.; Hansen, L. H.; Gondela, A.; Long, K.; Vester, B.; Kirpekar, F., *RNA* **2009,** *15* (2), 327-336.

30. Duschene, K. S.; Veneziano, S. E.; Silver, S. C.; Broderick, J. B., *Current Opinion in Chemical Biology* **2009,** *13* (1), 74-83.

31. Kamachi, T.; Kouno, T.; Doitomi, K.; Yoshizawa, K., *J. of Inorg. Biochem* **2011,** *105* (6), 850-857.

32. Hinckley, G. T.; Frey, P. A., *Biochemistry* **2006,** *45* (10), 3219-3225.

33. Wang, S. C.; Frey, P. A., *Biochemistry* **2007,** *46* (45), 12889-12895.

34. Walsby, C. J.; Ortillo, D.; Yang, J.; Nnyepi, M. R.; Broderick, W. E.; Hoffman, B. M.; Broderick, J. B., *Inorg. Chem.* **2005,** *44* (4), 727-741.

35. Layer, G.; Moser, J.; Heinz, D. W.; Jahn, D.; Schubert, W.-D., *EMBO J* **2003,** *22* (23), 6214-6224.

36. Daley, C. J. A.; Holm, R. H., *Inorg. Chem.* **2001,** *40* (12), 2785-2793.

37. Andrieux, C. P.; Robert, M.; Saeva, F. D.; Saveant, J. M., *J. Am. Chem. Soc.* **1994,** *116* (17), 7864-7871.

38. Daley, C. J. A.; Holm, R. H., *J. Inorg. Biochem.* **2003,** *97* (3), 287-298.

39. Daley, C. J. A.; Holm, R. H., *Inorg. Chem.* **2001,** *40* (12), 2785-2793

40. Hwang, J.; Govindaswamy, K.; Koch, S. A., *Chem. Commun.* **1998,** *0* (16), 1667-1668.

41. Licini, G.; Mba, M.; Zonta, C., *Dalton Trans.* **2009,** *0* (27), 5265-5277.

42. Bull, S. D.; Davidson, M. G.; Johnson, A. L.; Robinson, D. E. J. E.; Mahon, M. F., *Chem. Commun.* **2003,** *0* (14), 1750-1751.

43. Mba, M.; Prins, L. J.; Licini, G., *Org. Lett.* **2006,** *9* (1), 21-24.

44. Groysman, S.; Goldberg, I.; Goldschmidt, Z.; Kol, M., *Inorg. Chem.* **2005,** *44* (14), 5073-5080.

45. Keyes, W. E.; Loehr, T. M.; Taylor, M. L., *Biochem. Biophys. Res. Commun.* **1978,** *83* (3), 941-945.

46. Klabunde, T.; Sträter, N.; Fröhlich, R.; Witzel, H.; Krebs, B., *J. Mol. Biol.* **1996,** *259* (4), 737-748.

47. Kol, M.; Shamis, M.; Goldberg, I.; Goldschmidt, Z.; Alfi, S.; Hayut-Salant, E., *Inorg. Chem. Commun.* **2001,** *4* (4), 177-179.

48. Govindaswamy, N.; Quarless, D. A.; Koch, S. A., *J. Am. Chem. Soc.* **1995,** *117* (32), 8468-8469.

49. Tong, L. H.; Wong, Y.-L.; Lee, H. K.; Dilworth, J. R., *Inorg. Chim. Acta* **2012,** *383* (0), 91-97.

50. Tong, L. H.; Wong, Y.-L.; Pascu, S. I.; Dilworth, J. R., *Dalton Trans.* **2008,** *0* (35), 4784-4791.

51. Adam, B.; Bill, E.; Bothe, E.; Goerdt, B.; Haselhorst, G.; Hildenbrand, K.; Sokolowski, A.; Steenken, S.; Weyhermüller, T.; Wieghardt, K., *Chem. Eur. J.* **1997,** *3* (2), 308-319.

52. van Gorkum, R.; Berding, J.; Mills, A. M.; Kooijman, H.; Tooke, D. M.; Spek, A. L.; Mutikainen, I.; Turpeinen, U.; Reedijk, J.; Bouwman, E., *Eur. J. Inorg. Chem.* **2008,** *2008* (9), 1487-1496.

53. Reddig, N.; Pursche, D.; Krebs, B.; Rompel, A., *Inorg. Chim. Acta* **2004,** *357* (9), 2703-2712.

54. Pyrz, J. W.; Roe, A. L.; Stern, L. J.; Que, L., *J. Am. Chem. Soc.* **1985,** *107* (3), 614-620.

55. Frey, P. A.; Booker, S., 1999; Vol. 2, p 1.

56. Aggarwal, V. K.; Thompson, A.; Jones, R. V. H., *Tetrahedron Lett.* **1994,** *35* (46), 8659-8660.

57. Nicolet, Y.; Amara, P.; Mouesca, J.-M.; Fontecilla-Camps, J. C., *Proceedings of the National Academy of Sciences* **2009,** *106* (35), 14867-14871.

58. Srogl, J.; Allred, G. D.; Liebeskind, L. S., *J. Am. Chem. Soc.* **1997,** *119* (50), 12376-12377.